Distributed Generation Reformer and Fuel Cell System Modeling and Reformer Catalyst Layer Optimization

By

Kurtis Joseph Paul DePippo

A thesis submitted to the Graduate Program in Chemical
Engineering in conformity with the requirements for the
Degree of Master of Applied Science

Queen’s University

Kingston, Ontario, Canada

October, 2016

Abstract

This research presents a diesel-fed steam reformer and solid oxide fuel cell stack system Honeywell UniSim® Design Suites model and a two-dimensional diesel-fed steam reformer ANSYS Fluent model. The performance of the reformer and fuel cell system was compared to the performance of diesel generators in Canadian remote communities to illustrate the environmental and economic advantages that reformer and fuel cell systems have over typical diesel generation setups. The results show that, despite current solid oxide fuel cell technology being economically unfeasible, technology that is nearing commercialization could present substantial environmental and economic savings opportunities for diesel-based distributed generation projects.

The UniSim® model relied on several assumptions, one of which was the full conversion of the fuel feed within the steam reformer. A two-dimensional steam reformer model was therefore created in ANSYS Fluent to more accurately model the reforming process. Parameter studies on the reformer catalyst layer showed that reducing catalyst layer porosity along the length of the reformer results in improved reformer performance because of increased catalyst mass and higher reaction rates downstream that help push the reforming reaction towards equilibrium.

Acknowledgments

I would like to thank my supervisor, Dr. Brant Peppley, for his outstanding guidance and support throughout my graduate studies. Dr. Peppley has helped make my time at Queen’s University exciting and informative.

I would also like to thank Dr. Jon Pharoah, Dr. Warren Mabee, Dr. Scott Parent, Gillian Woodruff, FCRC members, as well as all other Chemical Engineering Department faculty and staff for providing me with invaluable learning experiences. In addition, I would like to acknowledge Dr. Christopher Thurgood and Dr. Alireza Naseri for their help with ANSYS Fluent.

I am grateful to NSERC’s Collaborative Research and Training Experience Program for providing me with additional learning opportunities beyond the scope of my research. I would also like to thank the Courtnage and Ballard families as well as all other funding sources that helped make my research possible.

Finally, I would like to thank my family and friends for being there to share in my successes and for their unwavering support.

Table of Contents

List of Tables

List of Figures

Abbreviations

RFC	Reformer and fuel cell system
WGS	Water-gas shift
SOFC	Solid oxide fuel cell
CHP	Combined heat and power
PRSV	Peng-Robinson-Soave-Vera
PR	Peng-Robinson
GEN1	1x200 kW diesel generator system
GEN2	2x100 kW diesel generator system
GEN3	5x40 kW diesel generator system
UDF	User-defined function
WSGGM	Weighted-sum-of-gray-gases model
ISAT	In situ adaptive tabulation

Chapter 1: Introduction

1.1: Background and Motivation

There are 292 communities in Canada that are not connected to the North-American electrical grid or to the piped natural gas network. These 292 communities are referred to as “remote communities” and are home to 194,281 people as of August 2011 [1]. Diesel generators are predominantly relied upon for electricity generation in 249 of the 292 Canadian remote communities, with a total annual diesel consumption of around 215 million litres. Diesel generation in remote communities is responsible for the emission of over 600 kilotons of carbon dioxide equivalents per year without including fuel transportation emissions, resulting in remote communities having 85% higher per capita greenhouse gas emissions than the Canadian average [2].

Diesel generation is not only environmentally unsustainable, but also economically unsustainable. The rising and uncertain cost of fossil fuels as well as the global shift away from carbon-based energy sources results in diesel-dependent remote communities having elevated, up to 20 times the average price of electricity paid by on-grid Canadians, and volatile electricity prices [2]. Therefore, diesel generation in remote communities discourages investment and also reduces electricity availability, resulting in remote communities having lower standards of living.

Reducing or eliminating diesel generation in remote communities would result in more stable electricity rates that would encourage economic growth within the communities. Current efforts are focused on improving energy efficiency, through conservation and/or generation efficiency improvements [3]. Tentative diesel displacement projects have also been implemented, with efforts being made to establish renewable energy pilot projects in remote communities to better understand the logistical and economic challenges associated with energy projects in remote communities. Larger scale diesel displacement renewable energy projects are planned to be the future of remote community electricity generation [2].

The feasibility of implementing renewable energy in remote communities is limited by the distance of the renewable energy source from the community and the availability of the renewable energy. Linking remote communities to nearby renewable resources, such as hydroelectric or geothermal energy sources, or to micro-grids comprised of multiple remote communities is subject to economic constraints that limit the distance transmission wires can be built, which is the primary reason why remote communities are considered to be “remote” and are not connected to the main electrical grid. Renewable resources that are available on-site to remote communities, such as wind, solar, and biomass, are generally not abundant enough to meet a community’s energy needs, with 1.8 MW being the average fossil fuel-reliant Canadian remote community generation capacity [1, 4]. However, wind power is seen as the most viable option for renewable power systems since the availability of the wind resource, unlike solar, is highest during the winter months, coinciding with the peak in remote community electricity demand [5, 6]. However, the installation of wind power in Canadian remote communities has not seen much progression. The start of 2011 saw 1.48 MW of installed wind capacity in Canadian remote communities, compared to 63.8 MW by the end of 2012 in Alaska [1, 7].

The stalled implementation of wind energy in Canadian remote communities is caused by the low rate of success experienced in earlier wind power pilot projects, with only 15% of the pilot projects remaining operational 8 years after installation [8]. Wind projects were primarily abandoned either because unforeseen installation costs exceeded a reasonable budget or because it was found that servicing small and scattered wind projects resulted in high operation and maintenance costs that did not meaningfully outweigh diesel savings [8]. Diesel generators do not suffer from the same maintenance issues that plague wind projects because replacement parts for generators are more readily available and the presence of locally trained technicians either within the community or nearby allows for more cost-effective labour [4]. However, the successful implementation of wind power in Alaska illustrates that wind technology can succeed in harsh climates and remote conditions.

The naturally limited and intermittent nature of wind resources means that remote community wind power projects must combine wind with existing diesel generation to meet a community's electricity demand. However, diesel generators achieve optimal generation efficiencies when operating at around 80% capacity [9]. Therefore, the benefit of diesel consumption reduction from increased renewable penetration in renewable-diesel systems would be partially mitigated by reduced diesel generator efficiencies.

A reformer and fuel cell system (RFC) could replace the diesel generators in a remote community. RFCs fed with low molecular weight hydrocarbons are currently being manufactured by companies such as Fraunhofer ICT-IMM for decentralized and mobile electricity generation [10]. A graphical representation of a RFC is shown in Figure 1-1. The reformer can convert fossil fuels to hydrogen rich syngas (synthesis gas primarily composed of carbon monoxide and hydrogen) which is then converted to electricity by the fuel cell. An RFC can utilize existing diesel infrastructure to produce electricity from diesel with more efficiency than diesel generators, aiding with current efforts of improving generation efficiency. Furthermore, a RFC would be capable of efficiently converting a variety of fuels (e.g. natural gas, gasoline, or hydrogen) to electricity. The fuel flexibility of an RFC would ensure that remote community electricity prices are not forced to be at the whim of diesel prices. Moreover, fuel flexibility could allow for the future use of more environmentally friendly fuels that could potentially be locally sourced with the added benefit of creating more local employment.

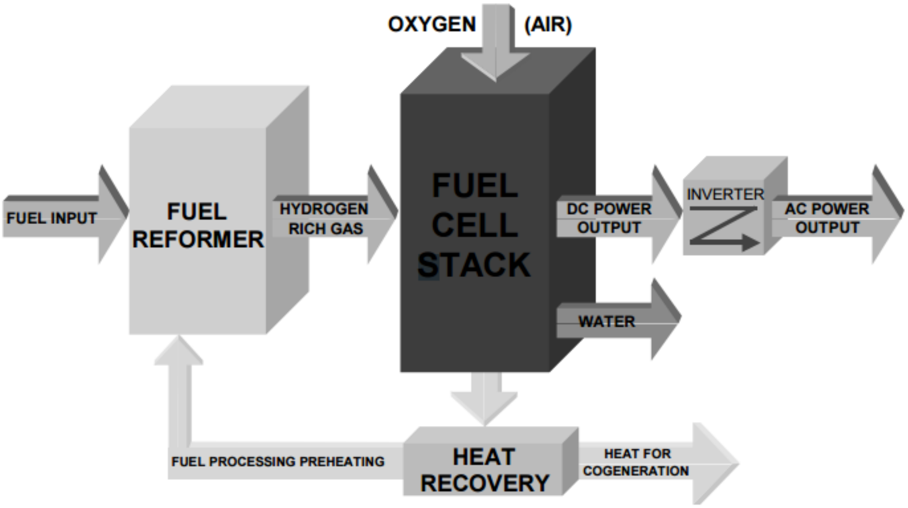

Figure 1-1: Reformer and fuel cell system representation [11].

A RFC would also complement renewable energy projects in remote communities. Contrary to diesel generators, RFCs have improved efficiencies at lower loads. Therefore, increased renewable penetration in a renewable-diesel system would have its impact on diesel consumption augmented by the RFC rather than mitigated by diesel generators. In addition, because of the increased fuel flexibility, the RFC could operate on stored hydrogen produced by converting excess renewable energy using an electrolyser. Hydrogen storage is advantageous to battery storage since hydrogen storage allows for longer term storage (months instead of days), it has much higher energy and power densities, and it makes it less expensive to increase storage capacity since new hydrogen storage tanks are cheaper than new lithium-ion batteries [12].

1.2: Thesis Objectives

The overall objective of this work was to model and optimize a diesel-fed RFC to be used for distributed electricity generation in Canadian remote communities. The first objective was to develop a steady state model of the RFC using Honeywell’s UniSim® Design Suite. The UniSim® model was then optimized to meet the electrical load of a small test case remote community. The second objective involved implementing previous work by Naseri et al. to create a more detailed steady state model of the RFC reformer using ANSYS Fluent [13]. The reformer catalyst layer porosity was varied along the length of the reformer to determine the effectiveness of this technique at reducing catalyst mass without sacrificing reformer performance. Furthermore, the impact of catalyst layer thickness on reformer performance was also studied.

The present work is designed to demonstrate the environmental and economic advantages of replacing diesel generators with RFCs in Canadian remote communities. The RFC UniSim® model presented can be used to determine the feasibility and benefits of replacing existing electricity generation systems with RFCs. Furthermore, the Fluent model presented in this work for microchannel reformer simulations implements previous work by Naseri *et al.* to improve catalyst layer simulation accuracy, thus allowing for the model to be used to determine the reformer performance impacts of various catalyst layer setups. Based on the Fluent model results, the present work demonstrates that catalyst savings and reformer length reductions can be achieved within a microchannel reformer by implementing a catalyst layer porosity distribution featuring an axially decreasing porosity profile.

1.3: References

[1] Aboriginal Affairs and Northern Development Canada, "Status of Remote/Off-Grid Communities in Canada," Government of Canada, 2011.

[2] M. Arriaga, C. A. Canizares and M. Kazerani, "Northern Lights," *IEEE Power & Energy Magazine,* pp. 50-59, 2014.

[3] Neegan Burnside Ltd., "Sharing the Story: Aboriginal and Northern Energy Experiences," Indian Affairs and Northern Development, Ottawa, 2004.

[4] T. M. Weis, A. Ilinca and J. Pinard, "Stakeholders' Perspective on Barriers to Remote Wind-Diesel Power Plants in Canada," *Energy Policy,* pp. 1611-1621, 2008.

[5] H. S. Wang, K. M. Spohn, L. Piccard and L. Yao, "Feasibility Study of Wind Power Generation System at Arctic Valley," *Engineering Management Journal,* vol. 22, no. 3, pp. 21-33, 2010.

[6] M. Devine and E. I. Baring-Gould, "The Alaska Village Electric Load Calculator," National Renewable Energy Laboratory, Oak Ridge, 2004.

[7] R. Stromberg, "Alaska Wind Energy Barriers," Alaska Energy Authority, 2012.

[8] T. M. Weis and A. Ilinca, "The Utility of Energy Storage to Improve the Economies of Wind-Diesel Power Plants in Canada," *Renewable Energy,* pp. 1544-1557, 2008.

[9] Arctic Energy Alliance, "Guide to Best Energy Practices for Remote Facilities," 2011.

[10] A. Schiegl, F. Reinhard, S. Butschek and G. Kolb, "Reformer Fuel Cell System with External Burner". United States Patent Patent 7,851,098, 14 Dec. 2010.

[11] J. M. Nail, G. Anderson, G. Ceasar and C. J. Hansen, "The Evolution of the PEM Stationary Fuel Cell in the U.S. Innovation System," The Organisation for Economic Co-operation and Development, 2000.

[12] H. Chen, T. N. Cong, W. Yang, C. Tan, Y. Li and Y. Ding, "Progress in Electrical Energy Storage System: A Critical Review," *Progress in Natural Science,* pp. 291-312, 2009.

[13] A. T. Naseri, B. A. Peppley, J. G. Pharoah, P. Mandal, S. Litster and N. Abatzoglou, "X-Ray Tomography-Based Analysis of Transport and Reaction in the Catalyst Coating of a Reformer," *Chemical Engineering Science,* vol. 138, pp. 499-509, 2015.

Chapter 2: Literature Review

2.1: Fuel Reforming

Hydrocarbon fuel reforming occurs at temperatures of 600°C to 1,000°C over a catalyst to produce syngas [1, 2]. Fuel reforming can also occur without a catalyst at higher temperatures, however non-catalytic reforming requires more costly construction materials for the reformer, is less efficient, and can result in the formation of unwanted nitrogen oxides, rendering non-catalytic reforming not overly useful for the proposed application [3]. Syngas is primarily composed of carbon monoxide, carbon dioxide, and hydrogen. The three primary reforming methods that use oxygen and/or steam are steam reforming, partial oxidation, and oxidative steam reforming (sometimes referred to as autothermal reforming).

2.1.1: Steam Reforming

Steam reforming is endothermic and results in the highest hydrogen yield by combining fuel with steam to produce syngas according to Equation 2-1 [3]. Steam reforming is favoured by high temperatures and low pressures. One disadvantage of steam reforming is that steam reformers require an external heat source and good heat transport to supply the reactants with the necessary thermal energy.

$$C_nH_m + nH_2O \rightarrow nCO + \left(n + \frac{m}{2}\right)H_2 \qquad \Delta H > 0 \qquad (2\text{-}1)$$

2.1.2: Partial Oxidation

Partial oxidation is exothermic and combines fuel with oxygen to produce syngas according to Equation 2-2 [3]. Partial oxidation is favoured by low temperatures and low pressures. Partial oxidation is much faster than steam reforming which allows for the use of smaller reforming reactors and allows for a rapid response to changes in power demand [4]. One disadvantage of partial oxidation is that it creates regions of high temperature within the reformer, resulting in the need for more robust building materials.

$$C_nH_m + \frac{n}{2}O_2 \rightarrow nCO + \frac{m}{2}H_2 \qquad \Delta H < 0 \qquad (2\text{-}2)$$

2.1.3: Oxidative Steam Reforming (Autothermal Reforming)

Oxidative steam reforming combines both steam reforming and partial oxidation reactions, with the fast kinetics of partial oxidation resulting in full consumption of oxygen near the entrance of the reactor and steam reforming being dominant for the rest of the reactor [5]. The separation of the partial oxidation and steam reforming reactions result in temperature spikes near the front of the reactor and temperature troughs downstream that require effective axial heat transfer to avoid damaging the catalyst [6, 7].

2.1.4: Additional Reforming Reactions

Fuel reforming includes other chemical reactions, such as the water-gas shift (WGS) reaction (Equation 2-3), the methanation reaction (Equation 2-4), and carbon dioxide reforming (Equation 2-5) [8, 9]. The WGS and methanation reactions are kinetically fast compared to reforming reactions and generally achieve or come close to achieving local and overall thermodynamic equilibrium within a reformer [7, 10]. The WGS reaction is effective at improving hydrogen selectivity for steam reforming as long as the operating temperature is not too high. A high operating temperature pushes the WGS equilibrium to the left, resulting in reduced hydrogen product selectivity. Moreover, the methanation reaction has improved hydrogen selectivity at higher temperatures, with negligible amounts of methane being produced from reformers with exit temperatures above 700°C [10]. The methanation reaction has reduced hydrogen selectivity at higher pressures. A pressure increase from 1 atm to 20 atm results in a higher temperature reformer (200°C hotter) being required to achieve full methane conversion [11]. Carbon dioxide reforming is slower than steam reforming and can be considered negligible when steam is present [4, 12]. It is important to note that the reforming of heavy hydrocarbons often results in the presence of lighter hydrocarbons at concentrations much greater than their thermodynamic equilibrium values, thus reducing hydrogen yield [10].

$$CO + H_2O \rightleftarrows CO_2 + H_2 \qquad \Delta H^0 = -41.2 \text{ kJ/mol} \qquad (2\text{-}3)$$

$$CO + 3H_2 \rightleftarrows CH_4 + H_2O \qquad \Delta H^0 = -206.2 \text{ kJ/mol} \qquad (2\text{-}4)$$

$$C_nH_m + nCO_2 \rightarrow 2nCO + \frac{m}{2}H_2 \qquad \Delta H < 0 \qquad (2\text{-}5)$$

2.2: Reformer Catalyst Deactivation

Reformer catalyst converts hydrocarbon feedstocks to syngas. Reformer catalysts can be deactivated through sintering or by being poisoned because of carbon or sulfur buildup on the catalyst. Catalyst deactivation reduces catalyst activity, leading to reduced hydrocarbon conversion rates and potential contaminant breakthrough that could lead to downstream catalyst deactivation.

2.2.1: Sintering

Catalyst thermal sintering results in a loss of active metal area in the catalyst or a decrease in the catalyst support area. There is a greater risk of sintering in reducing atmosphere, such as can be found with the high hydrogen and carbon monoxide concentrations present in syngas. The mechanism for sintering is not well understood for reforming catalysts, resulting in uncertainty regarding the temperature at which it may occur. It is hypothesized that sintering either occurs because of the diffusion of mass through the catalyst volume or because of the diffusion of mass over the catalyst surface. If sintering occurs because of diffusion through the catalyst particle volume then the Tamman temperature, the temperature above which the bulk mobility and reactivity of solid molecules are no longer negligible, becomes the temperature barrier above which sintering occurs [13]. The Tamman temperature is equal to half of the metal melting temperature and the Tamman temperature is most often identified as the sintering limit [14]. However, sintering has been shown to occur below the Tamman temperature [15]. If the sintering mechanism is linked to surface diffusion, then the Huttig temperature, the temperature above which metal surface species mobility is no longer negligible, would be the temperature barrier above which sintering may occur. The Huttig temperature is equivalent to one third of the metal melting temperature [13, 14].

2.2.2: Carbon Formation

Carbon formation results in an increased pressure drop through the reformer and causes catalyst deactivation as active sites are rendered inert through carbon encapsulation that make the active sites inaccessible to reactants. There are three kinds of carbon formed during steam reforming: whisker, pyrolytic, and gum [11, 16, 17].

Whisker carbon is produced through hydrocarbon decomposition on the catalyst surface. The carbon then diffuses into the catalyst crystals, blocking catalyst pores and resulting in a loss of active catalyst area and an increase in pressure drop. Pyrolytic carbon is obtained at temperatures exceeding 600^{o}C through the thermal cracking of higher hydrocarbons. Gum formation occurs at low temperatures through the slow polymerization of unsaturated hydrocarbons located on the catalyst surface when the kinetic rate of hydrocarbon cracking on the catalyst is surpassed by the rate of hydrocarbon adsorption on the catalyst [18].

2.2.2.1: Preventing Carbon Formation

The risk of carbon formation can be reduced by increasing the oxygen to carbon ratio and/or the steam to carbon ratio. Increasing these ratios also improves fuel conversion in the reformer. Increasing the oxygen to carbon ratio to unity, however, results in reduced reformer fuel conversion since it allows for complete oxidation to occur instead of partial oxidation [19]. Whisker carbon, pyrolytic carbon, and gum formation have different occurrence criteria. For whisker carbon, the risk of formation is drastically lowered when the steam to carbon ratio meets or exceeds the critical ratio, with the critical ratio being dependent on the hydrocarbon mixture feed [8, 20]. Whisker carbon is more likely to form at higher temperatures and pressures, and therefore the critical steam to carbon ratio increases with temperature and pressure [16, 21]. Contrary to whisker carbon, the risk of gum formation can be reduced most effectively by increasing operating temperatures. Furthermore, higher hydrogen partial pressures, higher steam to carbon ratios, the absence of aromatics, and the processing of smaller hydrocarbons all have the effect of reducing the risk of gum formation [16, 22]. As for pyrolytic coking, the risk of carbon formation increases with increasing temperatures [16].

Overall, the result is that carbon formation can be avoided by operating within a safe temperature range that is not high enough to risk whisker and pyrolytic carbon formation and not low enough to risk gum formation. Carbon formation is more likely to occur when the feed includes sulfur compounds and unsaturated hydrocarbons such as olefins and aromatics rather than just alkanes [20]. Unsaturated hydrocarbons are carbon precursors that may be formed through steam cracking of vapourized large hydrocarbons. Long residence times at elevated temperatures and in the absence of catalyst can lead to further thermal cracking that would result in carbon formation [23]. Catalyst deactivated by carbon deposition can be regenerated by passing a high temperature stream of hydrogen, steam, or oxygen through the reactor and then reducing any oxidized catalyst [24].

2.2.3: Sulfur Poisoning

Sulfur poisoning, much like carbon formation, results in catalyst deactivation and activity loss. Sulfur poisoning reduces catalyst activity as the active sites bond with sulfur compounds. Unlike carbon formation, catalyst sulfur coverage is independent of the steam to carbon ratio [20]. The presence of oxygen in the reformer feed, however, reduces the risk of sulfur poisoning since oxygen compounds oxidize the sulfur to form SO_2 which is not adsorbed on the catalyst [8]. Furthermore, catalyst selection and operating temperature impact the likelihood of sulfur poisoning, with cobalt and noble metal catalysts providing a distinct advantage over nickel catalysts and higher operating temperatures resulting in drastic decreases in catalyst deactivation [24, 25].

In case of sulfur poisoning, catalyst regeneration can be achieved by passing a hot hydrogen stream through the reactor, resulting in chemisorbed sulfur compounds reacting with the hydrogen to form H_2S [26]. Another method of catalyst regeneration is to oxidize the catalyst by passing hot steam or oxygen through the reactor, replacing sulfur compounds bound to the catalyst with oxygen, the oxidized catalyst would then have to be reduced [24]. The driving force for desorption, however, is low, making it not overly feasible to rely on catalyst regeneration to combat sulfur poisoning [20]. A low driving force for sulfur desorption means that the catalyst lifespan is dependent on the efficiency of upstream feedstock desulfurization. Upstream desulfurization of hydrogen sulfide and lower mercaptans can be accomplished using a zinc oxide catalyst bed, but heavier sulfur compounds, such as those found in diesel fuel, require much more aggressive desulfurization techniques [8]. Dibenzylthiophenes, which are present in diesel fuel, are the most difficult sulfur compounds to remove, with their concentration nearly unchanged even after deep desulfurization [27].

The risk of sulfur poisoning associated with diesel fuel is becoming less prominent as the U.S Environmental Protection Agency regulates diesel sulfur content towards 15 ppmw [28]. Desulfurization of diesel can be accomplished in either the vapour phase or the liquid phase. In the vapour phase, hydrodesulfurization is a viable sulfur removal option, although it suffers from high costs and low efficiency for removal of sterically hindered sulfur compounds. Bulk sulfur compound removal in the vapour phase can be more economically achieved using reactive sorbent-based gas-phase bulk desulphurization. The high boiling point of diesel makes sulfur compound removal in the vapour phase unfavourable since the sorbents have reduced sulfur equilibrium capacities at high temperatures, making liquid phase desulfurization preferable [28]. In the liquid phase, desulfurization can be accomplished with adsorption at as low as ambient temperatures [28]. Research is being conducted on liquid-phase adsorption using a combination of activated carbon and zeolite-13X sorbents. Activated carbon sorbents are useful for preliminary desulfurization thanks to their high capacities. However, activated carbon sorbents have low cleanup efficiencies. Zeolite-13X sorbents are useful for secondary deep desulfurization as they have low capacities, but high sulfur removal efficiencies [29, 30]. Salem *et al.* proposed an activated carbon bed at 80^{o}C followed by a zerolite-13X bed at room temperature to achieve deep desulfurization of petroleum derived fuels. An additional advantage of using the above setup for sulfur removal is that activated carbon is effective at removing dibenzothiophenes (the hard to remove sulfur compounds found in diesel) [31].

2.3: Considerations for Diesel Reforming

2.3.1: Impact of Aromatics

Diesel is comprised of an array of hydrocarbons that include paraffins, olefins, and aromatics, with the olefins and aromatics being more likely to form carbon precursors [19]. High aromatic concentrations in diesel (16.3 wt%) result in slower reforming kinetics because stronger C-C bond energies found in aromatics makes it difficult to achieve aromatic conversions over 90%, resulting in a reformate not approaching expected thermodynamic equilibrium concentrations [7, 32].

2.3.2: Gas-Phase Reactions

At temperatures above 600-650^{o}C, and under conditions of low catalyst activity, large paraffins often undergo gas-phase cracking to form lighter hydrocarbons through hydrogen abstraction (to create alkanes) and beta scission (to create alkenes) according to Equation 2-6 [16]. Beta scission takes over at low pressure and high temperature, the conditions used for reforming, resulting in carbon-precursor olefin production and little to no C_3+ alkanes being formed at these conditions [33]. Furthermore, larger hydrocarbons, such as those found in diesel, are more likely to undergo cracking because of their slower reforming reaction rates [34]. Parmar's work shows that oxidative steam reforming gas-phase reaction products consist primarily of carbon monoxide, ethylene, propylene, and carbon dioxide [33]. The presence of carbon monoxide and carbon dioxide is primarily due to the presence of oxygen in the oxidative steam reforming reactant flow, as evidenced by Parmar's work which showed a sharp reduction in carbon oxide production as the oxygen to carbon ratio in the feed was reduced. In addition, the propylene yield trended upwards as the oxygen to carbon ratio was reduced.

$$C_nH_m \rightleftarrows olefins + H_2 \qquad \Delta H > 0 \qquad (2\text{-}6)$$

2.3.3: Carbon Formation

Diesel must be fully evaporated before entering the reformer since contact of liquid aromatics with the reformer catalyst would result in coke formation. Furthermore, the vapourized diesel must be homogeneously mixed with steam to produce a constant steam to carbon ratio to yield consistent hydrogen production. Non-homogeneous mixing of the vapourized diesel with steam or oxygen could result in coke formation (regions of insufficient steam) and dangerous temperature spikes (regions of ample oxygen) respectively. Moreover, extra safety precautions must be taken when conducting the partial oxidation of fuels containing hydrocarbons larger than n-decane since these larger hydrocarbons have auto-ignition temperatures lower than their boiling points. Rapid mixing is required for partial oxidation so as to quickly bring the carbon to oxygen ratio above the auto-ignition limits [9]. In addition, catalyst selection for diesel reforming is vital for avoiding coke formation and sulfur poisoning. Base metals, such as nickel, should not be used as diesel reforming catalysts as they have poor coking resistances and are poisoned at sulfur levels above 100ppbv. Moreover, noble metal catalysts, such as rhodium-based catalysts, can achieve the best conversion, result in a reforming process with minimal coking, and can withstand sulfur concentrations up to 1-10 ppmv [9, 35].

High temperature reformer operation allows for the overcoming of the low reforming reactivity of aromatics, allowing for their complete conversion to syngas and the avoidance of coke formation. Coke formation can also be avoided by utilizing higher steam to carbon and oxygen to carbon ratios as it helps prevent coke precursor formation and allows for the oxidation of coke deposits. High temperature operation, however, requires that the reformer and catalyst be fabricated of materials with high thermal resistance to avoid reformer degradation and catalyst deactivation through sintering [9].

Work by Parmar *et al.* to determine the temperature boundary for coke formation in a hexadecane fed reformer resulted in the minimum carbon-free operating temperatures enclosed in Table 2-1 [36]. Parmar *et al.*'s work indicates that partial oxidation is not a valid approach for diesel reforming since it requires high temperatures and high oxygen to carbon ratios to avoid carbon formation.

Table 2-1: Carbon Formation Boundary Temperature (°C) by Parmar *et al.* for Hexadecane Reforming at Atmospheric Pressure [36]

H_2O/C	**0.00**	**0.75**	**1.00**	**1.25**	**1.50**	**1.75**	**2.00**
O_2/C							
0.00	>>1,276	>>1,023	974.9	711.1	649.4	583.4	238.3
0.125	>>1,276	1,023.4	717.3	657.0	600.4	315.4	231.9
0.25	>>1,276	727.7	663.2	611.1	528.8	282.8	219.9
0.50	1,276.0	624.7	570.1	443.8	292.8	229.4	187.9
0.75	678.8	514.1	371.9	273.8	217.4	178.6	149.4
1.00	584.9	300.4	230.3	178.9	150.6	125.0	104.7

2.3.4: Surrogate Fuel for Modeling

Diesel is a mixture of several different hydrocarbon species which complicates the modeling of diesel-fed systems. ANSYS Fluent in particular suffers from drastically reduced convergence speeds as species and reaction counts increase. Therefore, it is advantageous to represent diesel with a surrogate fuel. An effective surrogate for diesel is hexadecane. Hexadecane is the predominant hydrocarbon (38.7 wt%) in certified grade diesel fuel [7]. Hexadecane may be a widely accepted as a valid surrogate for diesel, but true diesel reforming has a lower hydrogen yield and a higher outlet methane concentration than hexadecane reforming due to the presence of unsaturated hydrocarbons in conventional diesel [7]. Gas-to-liquid diesel, which is predominantly composed of paraffins, does show good agreement with hexadecane in terms of reformate composition [7].

2.4: Reformer Designs

Fixed-bed reactors, monolithic reactors, and microchannel reactors are three different types of reactor used to reform fuel into syngas.

2.4.1: Fixed-Bed Reactors

Fixed-bed reactors constitute a channel or multiple tubes packed with catalyst. Fixed bed reactors suffer from high pressure drop as well as large temperature gradients caused by the large heats of reaction and the poor thermal conductivity through the catalyst bed. Temperature gradients can be reduced in fixed-bed reactors by having high reactant flow rates to induce turbulent mixing for better convective heat transport or by densely packing the reactor to minimize void fractions and thus reduce tortuosity for thermal conduction. However, using higher reactant flow rates and/or increasing catalyst packing density results in even higher pressure drops through the reactor and the former would also require a larger reactor to achieve the necessary residence time. An advantage of fixed-bed reactors is the ease with which the catalyst bed can be removed and replaced should widespread irreversible catalyst deactivation occur [9].

2.4.2: Monolithic Reactors

Monolithic reactors overcome fixed-bed reactor drawbacks of high-pressure drop and large temperature gradients by structuring the catalyst layers to allow for more direct mass and heat transport pathways. Monolithic reactors are composed of multiple small diameter channels whose walls act as supports for the catalyst. The proximity of the catalyst to the channel walls results in reactions occurring near channel walls. Reaction proximity to the wall, given the high thermal conductivity of the wall, results in reduced temperature gradients. Furthermore, the catalyst proximity to the channel walls results in an open flow path through the middle of the channel, lowering the reactor pressure drop.

Monolithic reactors operate in the laminar flow regime and are thus reliant on species diffusion to allow for the reactants to reach the catalyst. Although turbulent flow has a faster reaction rate because of better mixing which results in higher reactant concentrations at the catalyst surface, it requires a longer and more expensive reactor to achieve the same residence time and conversion seen with laminar flow [37]. The use of laminar, however, does result in the need for longer residence times than fixed-bed reactors since the reactants require time to diffuse into the catalyst layer. An additional design drawback of monolithic reactors is the manifold system required to ensure that the bulk flow is divided evenly across all reactor channels to ensure consistent reactor production. In addition, widespread irreversible catalyst deactivation in a monolithic reactor would require the replacement of the entire unit since the catalyst cannot be easily removed from the reactor walls [9].

2.4.3: Microchannel Reactors

Microchannel reactors are similar in design to monolithic reactors in that they both separate the bulk flow into multiple parallel channels whose walls act as the support for the catalyst layer. Monolithic reactor channel diameters, however, are in the millimetre to centimetre range whereas microchannel reactors are in the micrometre to millimetre range. These smaller channel sizes result in higher surface area to volume ratios which reduce heat and mass transfer limitations [38, 39]. Microchannel reactors share most of the same advantages and disadvantages of monolithic reactors with some important differences. Microchannels allow for better control over reactor residence times, leading to more control over syngas composition, but at the cost of higher pressure drops. Furthermore, microchannel reactors have high surface area to volume ratios which allows for effective coupling of microchannel reactors with heat exchange where certain channels within the reactor are used for hot fluid transport instead of acting as reacting channels [9]. The above concept of alternating reaction channels and heating channels is referred to as a catalytic plate reactor (Figure 2-1), a setup presented by Reay [40].

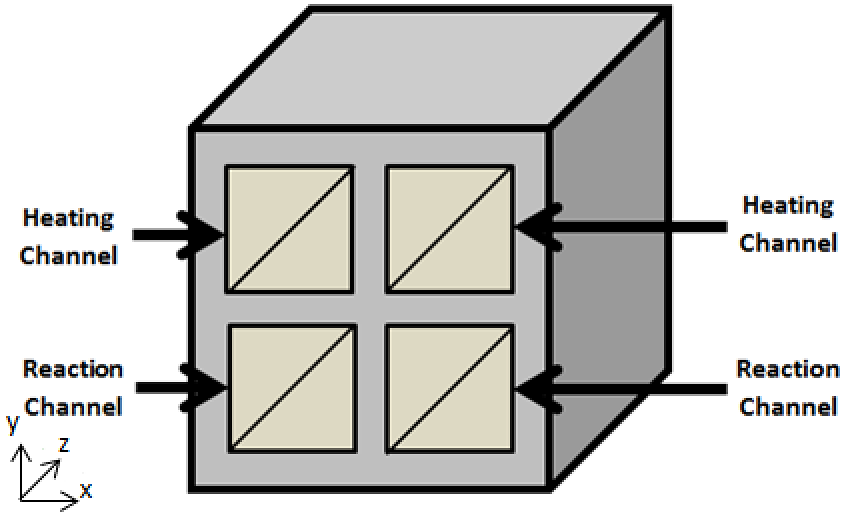

Figure 2-1: Catalytic plate reformer illustrating a potential reformer design that uses alternating reaction and heating channels to couple reforming with heat exchange.

2.4.3.1: Catalytic Plate Reactors

The performance of a catalytic plate reactor is dependent on the geometrical configuration of the channels, such as: channel height, wall thickness, catalyst layer thickness, and the thermal conductivity through the wall and catalyst layer [9]. For heat exchange coupling, counter-current operation was found to result in the formation of larger temperature gradients. Therefore, co-current operation is preferred [41, 42].

2.5: Previous Reformer Modeling Work

Previous reformer modeling work focused on modeling light hydrocarbon reforming using either one-dimensional or two-dimensional models, with the occasional researcher implementing a three-dimensional model. The following section will outline some of the previous work completed in reformer modeling. Reformer specifications for the previous work are summarized in Table 2-2.

Frauhammer *et al.*, 1999

In 1999, Frauhammer *et al.* published simulation results for the one dimensional modeling of a counter-current fixed-bed reactor that combined methane steam reforming with methane combustion [43]. Frauhammer *et al.* used a one-dimensional model because experimental work and two-dimensional simulations showed that gradients along the cross-section of the reactor channels were negligible. However, a one-dimensional approach does not allow the impacts of wall thickness or catalyst thickness to be studied.

Zanfir and Gavriilidis, 2003

In 2003, Zanfir and Gavriilidis modelled a two-dimensional co-current catalytic plate reformer with methane steam reforming on one side of the heat exchange wall and methane catalytic combustion on the other side [44]. Zanfir and Gavriilidis assumed some channel symmetry in order to simplify their model. The first symmetry assumption was that an infinite number of channels in the reactor y-direction would result in a repeating unit consisting of exothermic and endothermic channel pairings which would have a net y-direction heat flux of zero. The net y-direction heat flux of zero, therefore, allows for the establishment of planes of symmetry at the centreline of each channel, resulting in the modeling of a repeated unit consisting of a wall with an exothermic channel half-height on one side and an endothermic channel half height on the other. Further assumptions include the use of a one-dimensional approach to model the catalyst layers, justified by the small thickness of the catalyst layer compared to the reactor length. This one-dimensional approach to catalyst modeling, however, does not allow for the inclusion of species transport within the catalyst layer.

The effect of the channel height on reformer performance was studied by changing the channel height as well as the inlet velocity to maintain a constant flowrate through the reformer. Zanfir and Gavriilidis found that increasing channel height resulted in an upstream movement of the reaction rate peaks caused by the lower inlet velocities, and corresponding higher residence times, used as the channel height increased. The upstream movement of reaction rate peaks , however, were partially mitigated by longer mass transfer pathways from the channel centreline to the catalyst layer. In addition, an increase in channel height resulted in higher temperature gradients between the wall and the channel centreline, as would be expected as the channel centreline was placed further from the wall. A further study was conducted on the impact of increasing the catalyst layer thickness while maintaining a constant ratio of catalyst layer thickness to velocity. For this study the catalyst layer was modeled in two dimensions. Thicker catalyst layers resulted in lower conversions because of lower residence times stemming from higher velocities and because of higher mass transfer resistances through the catalyst layer. These higher mass transfer resistances resulted in a lower percentage of catalyst being utilized and essentially meant that the ratio of flowrate to utilized catalyst was increased.

Aubin *et al.*, 2009

Current manufacturing techniques limit microchannel reformer cross-sections to rectangles. Laminar flow within these rectangular ducts leads to a wide range of residence times, resulting in reduced selectivity of the desired product. Aubin *et al.* modified the aspect ratio (channel height over channel width) of rectangular duct microchannels to determine the effect that aspect ratio has on residence time distributions. They found that lower aspect ratios resulted in narrower residence time distributions that resembled those of ideal plug flow [45].

Hsueh *et al.*, 2009

Hsueh *et al.* used a three-dimensional model to study the effect of channel aspect ratios on methanol fuel conversion in a steam reformer [46]. Hsueh *et al.* studied aspect ratios ranging from 0.25 to 2 using a consistent hydraulic diameter of 0.286 mm and operated under the assumptions that thermal radiation and thermal conduction within the fluid were negligible compared to convection and that the wall temperature remained constant along the length of the reactor. The channel simulated, however, only had a catalyst layer along the top wall and did not have catalyst along the side walls or along the bottom. The catalyst layer was simulated with thickness, allowing for transport equations to be solved within the catalyst layer. Hsueh *et al.* found that reformers achieve better fuel conversion at lower aspect ratios. This finding was partially because of the presence of a greater volume of catalyst as the aspect ratio deviates from unity and the catalyst layer thickness is kept constant. Furthermore, considering the setup of Hsueh *et al.*'s model which only had catalyst along the width of the channel and not along the height, lower aspect ratios were expected to be more effective since they resulted in catalyst along a larger portion of the channel perimeter and a shorter mass transport path from the channel centreline to the catalyst.

Arzamendi *et al.*, 2009

Arzamendi *et al.* modeled a catalytic plate reformer consisting of four rectangular channels [47]. The catalytic plate reformer combined methanol steam reforming with methanol combustion. This work demonstrated how co-current flow results in the smallest axial temperature differential (4^{o}C in Arzamendi *et al.*'s case), while higher temperature differentials occur in setups with perpendicular cross-current flow (7^{o}C) and counter-current flow (19^{o}C).

Shi *et al.*, 2009

Shi *et al.* created a three-dimensional ANSYS Fluent model for the oxidative steam reforming of hexadecane in a monolith reactor with a circular cross-section [48]. Shi *et al.* aimed to model the entire monolith reactor. The modeling was simplified by using horizontal and vertical planes of symmetry that ran through the centre-point of the reactor so that only a quarter of the total circular cross-section had to be modeled. Shi *et al.* simplified the model by representing the entire monolith zone as a porous region instead of modeling the monolith as bulk flow, catalyst, and wall regions. Shi *et al.* also created surface reaction rate expressions for hexadecane partial oxidation, hexadecane steam reforming to carbon monoxide, hexadecane steam reforming to carbon dioxide, and WGS reaction. Shi *et al.* found that, although the carbon oxide content in the reformate was similar to their equilibrium values, the hydrogen content in the reformate was lower than the equilibrium value by 20%. Shi *et al.* state that the discrepancy in the reformate hydrogen concentration was caused by only 72% of the fuel being reformed. A sensitivity analysis of the model to the feed rate showed that as the feed rate was increased and residence times reduced the reformer became less efficient and the pressure drop increased from 150 Pa to 720 Pa.

Thormann *et al.*, 2009

Thormann *et al.* modeled hexadecane steam reforming in a microchannel reactor composed of 1,400 microchannels with square cross-sections [49]. Thormann *et al.* found that the reformate approached equilibrium composition at temperatures greater than 823 K. Reformate methane concentration was deemed to be negligible through experimental work conducted by Thormann *et al.* The model was created for one microchannel since the reactor was set-up so that all of the microchannels essentially behaved the same. Isothermal boundary conditions were assumed for the channel because the temperature difference along the catalytic wall was always below 5 K. The microchannel square cross-section was modeled as an axisymmetric circle with equivalent hydraulic diameter so as to model the microchannel as a cylinder in two-dimensions. The catalyst is treated as infinitely thin with reactions occurring on the surface being balanced by diffusion to and from the bulk flow.

Karakaya and Avci, 2011

Karakaya and Avci conducted a study on a catalytic plate reformer that coupled methane oxidation with iso-octane steam reforming [50]. Karakaya and Avci decided to use a two-dimensional model instead of a three-dimensional model since lateral heat flow in the x-direction (Figure 2-1 above) is nullified by equivalent heat flow from the neighbouring channel, resulting in the temperature gradients in the x-direction being negligible compared to the temperature gradients in the y-direction. In a similar manner to the previously discussed models, Karakaya and Avci used the planes of symmetry within the channels to reduce the modeling region to half the channel height with a wall in between. An advantage of switching from the three-dimensional model to the two-dimensional model was a reduction in cell count from 70,388 to 33,980 with CPU run times being reduced from 32 hours to three minutes. Karayaka and Avci found that thicker walls resulted in increased fuel conversion, and a reduction in the temperature difference between inlet and outlet. These findings were the result of the wall acting as a thoroughfare through which heat could be delivered to the catalyst to allow for fuel conversion, with a thicker wall allowing for the transport of more heat axially along the reactor length. The higher radial thermal resistance of thicker walls, however, had the undesirable effect of compounding the temperature drop over the first few millimetres of the channel, making for higher temperature gradients near the inlet.

Naseri *et al.*, 2014

Naseri *et al.* created a three-dimensional model of a methane steam reformer thermally coupled with a flue gas stream in a catalytic plate reactor [51]. The model consisted of a multi-stage approach that combined transport processes and reactions that occurred at the reactor level with the effective transport properties and reactions in the catalyst microstructure. The catalyst was assumed to be made up of spherical particles with an internal structure comprised of smaller spherical particles.

Caglar *et al.*, 2015

Caglar *et al.* suggest steam reforming glycerol into syngas so as to make use of the large amount of additional glycerol they forecast being produced as biodiesel becomes more widely used. [52]. Caglar *et al.* conducted their modeling work using a channel with a very small height to width ratio since this reduced axial dispersion and led to more uniform diffusion mixing according to Aubin *et al.* [45]. Therefore, because of this height to width ratio Caglar *et al.* deemed the effect of the vertical walls on each end of the channel to be negligible as they did not account for a significant portion of the channel perimeter, thus allowing for the reacting channel to be modeled in two dimensions, height and length, discounting width. Because of the plane of symmetry at the centreline of the channel only half of the channel height had to be modeled. Caglar *et al.* corroborated the findings of Karakaya and Avci that thicker walls result in improved reformer performance. It was also determined that reducing the inlet temperature reduced fuel conversion since there was less thermal energy available to drive the reforming reactions.

Table 2-2: Reformer Dimensions and Reforming Channel Fluid Inlet Properties used in Previous Catalytic Plate Steam Reformer Research

Researchers	Channel Length (mm)	Channel Height (mm)	Channel Width (mm)	Catalyst Layer Thickness (mm)	Wall Thickness (mm)	Inlet Velocity (m/s)	Model Dimension
Zanfir and Gavriilidis [44]	300	2	-	0.02	0.5	4	2-Dimensional
Hsueh *et al.* [46]	33	0.179-0.429	0.214-0.714	0.03	-	-	3-Dimensional
Thormann *et al.* [49]	80	0.2	0.2	-	-	-	2-Dimensional
Karakaya and Avci [50]	100	0.28-0.56	-	0.06	0.1-0.4	-	2-Dimensional
Naseri *et al.* [51]	20	0.8	1	0.1	0.8	0.8	3-Dimensional
Caglar *et al.* [52]	100	0.65	10	0.05	0.3-0.7	-	2-Dimensional

2.6: Catalyst Modeling Considerations

The reformer's catalyst layer can be modeled using either the surface reaction method or the volumetric reaction method. The surface reaction method assumes an infinitely thin catalyst layer with the reactions taking place at the boundary between the catalyst layer and the bulk flow. The surface reaction method ignores the effects of washcoat thickness, porosity, and diffusion within the catalyst. When using the surface reaction method the effect of diffusional resistance within the catalyst layer is often represented by effectiveness factors below unity, to represent that not all of the catalyst is used [53]. Using an effectiveness factor makes for a simpler model, but it discounts the thermal effects of the catalyst layer and does not account for the difference in diffusivities between various compounds [54]. Unlike the surface reaction method, the volumetric reaction method models the catalyst layer as a region with thickness, thus taking into account those parameters ignored by the surface reaction method [55]. One of the issues with the volumetric method is that it significantly increases computing times since it requires the calculation of mass balances within a layer that sees low velocity flow and as a result has a very small time scale. Mladenov *et al.* showed that diffusion within the porous layer used in the volumetric reaction approach has a larger mass transfer effect than radial diffusion from the bulk flow to the catalyst wall used in the surface reaction approach [56]. Furthermore, Massing *et al.* created a model that demonstrated that propylene conversion is diffusion limited, as shown by increases in catalyst layer thickness resulting in lower propylene conversion than would be expected given the volume of added catalyst [57]. Conclusively, the volumetric reaction method allows for the discrimination between intrinsic kinetics and mass transfer effects, allowing for the best agreement with experimental data [56].

2.7: One-Dimensional *vs.* Two-Dimensional *vs.* Three-Dimensional Computational Fluid Dynamics Models

Mladenov *et al.* studied the differences between one-dimensional, two-dimensional, and three-dimensional catalytic converter models [56]. The data presented in Mladenov *et al.*'s study is relevant to reformer modeling because of the similarities in channel catalytic reactions, albeit reforming reactions are significantly faster than reactions in catalytic converters and are also completed at higher temperatures. Both the one-dimensional and two-dimensional models are forced to only consider cylindrical channel geometries, whereas the three-dimensional model can consider geometries with square cross-sections [56, 58].

The one-dimensional plug flow model ignores the impact of diffusion on the reacting flow, resulting in significantly faster reactant conversion than expected, but benefits from faster convergence speeds. Improved model accuracy can be achieved by including diffusion impacts on the reacting flow in a two-dimensional or three-dimensional model. There is little differentiation between two-dimensional and three-dimensional models, since they have similar species profiles, thus suggesting that three-dimensional rectangular channels can be modeled by two-dimensional cylindrical channels with the same catalyst layer thickness, porosity and activity, and the same fluid velocity and mass flow rate [56]. In addition, channels with rectangular cross-sections and very small aspect ratios can be modeled with reasonable accuracy in two-dimensions [58]. The advantage of three-dimensional modeling is the ability to investigate the impact of channel aspect ratios. The major disadvantage of three-dimensional modeling, however, is the significantly slower computation speed compared to two-dimensional modeling. Properly modeling the reformer is important for conducting reformer parameter sensitivity analyses and for ensuring that the correct syngas composition is exiting the reformer and entering the fuel cell stack.

2.8: Fuel Cells

Fuel cells convert the chemical energy of a fuel into electrical energy. There are several different types of fuel cells differentiated by their electrolyte membranes and electrode catalysts which dictate their operating temperature range and their susceptibility to impurities. In general all fuel cell types follow Equation 2-7 to convert hydrogen and oxygen feeds into water or steam depending on their operating temperature.

$$H_2 + \frac{1}{2}O_2 \rightarrow H_2O \qquad \Delta H^0 = -242 \text{ kJ/mol} \qquad (2\text{-}7)$$

2.8.1: Low Temperature Fuel Cells

Low temperature fuel cells, such as polymer electrolyte membrane fuel cells (< 120°C), alkaline fuel cells (< 100°C), and phosphoric acid fuel cells (150°C – 200°C) suffer from sensitivities to fuel impurities (*e.g.* carbon monoxide, carbon dioxide, and/or sulfur compounds) [59]. Because reformer produced syngas includes carbon monoxide and carbon dioxide, directly feeding syngas into polymer electrolyte membrane fuel cells or alkaline fuel cells is not advisable and additional unit operations must be implemented to eliminate impurities within the syngas. Phosphoric acid fuel cells are less sensitive to carbon oxides thanks to their slightly higher operating temperature, but they suffer from high sulfur sensitivity which reduces their fuel flexibility since sulfur compounds can be found in or are added to fuels such as natural gas and diesel. Furthermore, phosphoric acid fuel cells have electrical efficiencies of around 40%, lower than other low temperature fuel cells which generally have electrical efficiencies around 60% [59].

2.8.2: High Temperature Fuel Cells

High temperature fuel cells, such as molten carbonate fuel cells (600°C – 700°C) and solid oxide fuel cells (SOFCs) (650°C – 1,000°C) have greater fuel flexibility than their low temperature counterparts since high operating temperatures result in a higher tolerance for impurities [59, 60]. Because of the higher impurity tolerance of high temperature fuel cells post-reformer syngas processing is not required, allowing for less complex and associatively cheaper systems. Furthermore, higher operating temperatures allow for internal reforming reactions to occur on the anode or on a separate catalyst integrated within the fuel cell stack, but upstream of the anode. Similar to the reformer, these internal reforming reactions convert thermal energy into chemical energy within the fuel which results in higher electrical efficiencies and lower thermal efficiencies for high temperature fuel cell systems compared to low temperature fuel cell systems [61]. Utilizing fuels made up of smaller hydrocarbons, such as natural gas, eliminates the need for any external reforming, allowing for the design of simpler, cheaper, and more efficient power units [62]. High operating temperatures also result in combined heat and power (CHP) opportunities since the heat generated by high temperature fuel cells is of a much higher quality (at a higher temperature) than that generated by low temperature fuel cells. However, high operating temperatures result in longer start-up times and make these fuel cells susceptible to high temperature corrosion, reducing their lifespan. Thanks to higher electrical efficiencies and a solid electrolyte which is easier to manage and results in longer fuel cell lifespans, SOFCs are more effective than molten carbonate fuel cells [59].

2.8.3: Fuel Cell Losses

The irreversible losses that reduce fuel cell potentials below the Nernst potential (open circuit voltage) are activation polarization, ohmic polarization, and concentration polarization [63]. These losses are illustrated in Figure 2-2. Activation polarization is the primary source of fuel cell potential losses when the fuel cell is operating at lower current densities. Activation polarization occurs because the reactants in the fuel cell must overcome a certain energy threshold before they can ionize to produce current and ionic flow. Activation losses are significantly pronounced in low temperature fuel cells and only occur at low current densities [64]. Moreover, ohmic polarization losses occur because of resistance in the electron pathway. Because cell resistances remain essentially constant ohmic losses are directly proportional to current density [63]. Finally, concentration polarization losses are prevalent at high current densities and are a result of fuel cell reactions occurring so rapidly that they become diffusion limited [63]. Minimizing polarization losses is vital for achieving efficient fuel cell stack operation and improved RFC performance.

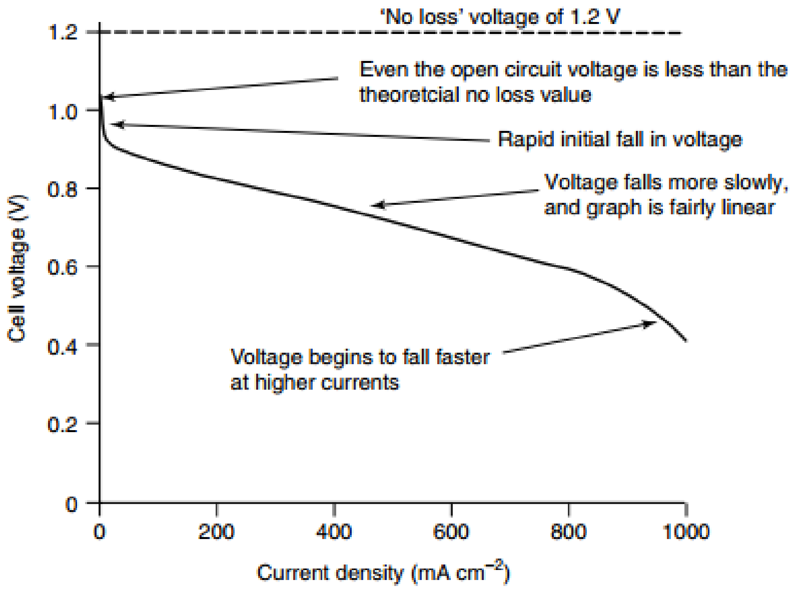

Figure 2-2: Polarization curve for a typical low temperature fuel cell [76].

2.9: References

[1] Y. Jamal and M. L. Wyszynski, "On-Board Generation of Hydrogen-Rich Gaseous Fuels - A Review," *International Journal of Hydrogen Energy,* vol. 19, no. 7, pp. 557-572, 1994.

[2] A. Naidja, C. R. Krishna, T. Butcher and D. Mahajan, "Cool Flame Partial Oxidation and its Role in Combustion and Reforming of Fuels for Fuel Cell Systems," *Progress in Energy and Combustion Science,* vol. 29, no. 2, pp. 155-191, 2003.

[3] D. Shekhawat, D. A. Berry and J. J. Spivey, "Introduciton to Fuel Processing," in *Fuel Cells: Technologies for Fuel Processing*, Elsevier, 2011, pp. 1-9.

[4] D. L. Trimm and Z. I. Onsan, "Onboard Fuel Conversion for Hydrogen-Fuel-Cell-Driven Vehicles," *Catalysis Reviews,* vol. 43, no. 1-2, pp. 31-84, 2001.

[5] D. J. Haynes and D. Shekhawat, "Oxidative Steam Reforming," in *Fuel Cells: Technologies for Fuel Processing*, Elsevier, 2011, pp. 129-190.

[6] I. Kang and J. Bae, "Autothermal Reforming Study of Diesel for Fuel Cell Application," *Journal of Power Sources,* vol. 159, pp. 1283-1290, 2006.

[7] I. Kang, J. Bae and G. Bae, "Performance Comparison of Autothermal Reforming for Liquid Hydrocarbons, Gasoline and Diesel for Fuel Cell Applications," *Journal of Power Sources,* vol. 163, pp. 538-546, 2006.

[8] J. R. Rostrup-Nielsen and J. Bogild Hansen, "Steam Reforming for Fuel Cells," in *Fuel Cells: Technologies for Fuel Processing*, Elsevier, 2011, pp. 49-71.

[9] Z. I. Onsan and A. K. Avci, "Reactor Design for Fuel Processing," in *Fuel Cells: Technologies for Fuel Processing*, Elsevier, 2011, pp. 451-516.

[10] D. J. Liu, T. D. Kaun, H. K. Liao and S. Ahmed, "Characterization of Kilowatt-Scale Autothermal Reformer for Production of Hydrogen from Heavy Hydrocarbons," *International Journal of Hydrogen Energy,* vol. 29, pp. 1035-1046, 2004.

[11] J. R. Rostrup-Nielsen, J. Sehested and J. K. Norskov, "Hydrogen and Synthesis Gas by Steam- and CO2 reforming," *Advances in Catalysis,* vol. 47, pp. 65-139, 2002.

[12] J. R. Rostrup-Nielsen and B. Hansen, "CO2-Reforming of Methane over Transition Metals," *Journal of Catalysis,* vol. 144, pp. 38-49, 1993.

[13] M. Baerns, Basic Principles in Applied Catalysis, Springer Science & Business Media, 2013.

[14] T. Popa, G. Xu, T. F. Barton and M. D. Argyle, "High Temperature Water Gas Shift Catalysts with Alumina," *Applied Catalysis A: General,* vol. 379, pp. 15-23, 2010.

[15] J. Sehested, "Four Challenges for Nickel Steam-Reforming Catalysts," *Catalysis Today,* vol. 111, pp. 103-110, 2006.

[16] J. R. Rostrup-Nielsen, T. S. Christensen and I. Dybkjaer, "Steam Reforming of Liquid Hydrocarbons," *Studies in Surface Science and Catalysis,* vol. 113, pp. 81-95, 1998.

[17] J. Rostrup-Nielsen and L. J. Christiansen, Concepts in Syngas Manufacture, London: Imperial College Press, 2011.

[18] Z. Chen, Y. Yan and S. S. Elnashaie, "Catalyst Deactivation and Engineering Control for Steam Reforming of Higher Hydrocarbons in a Novel Membrane Reformer," *Chemical Engineering Science,* vol. 59, pp. 1965-1978, 2004.

[19] S. Yoon, I. Kang and J. Bae, "Effects of Ethylene on Carbon Formation in Diesel Autothermal Reforming," *International Journal of Hydrogen Energy,* vol. 33, pp. 4780-4788, 2008.

[20] J. Rostrup-Nielsen, "Steam Reforming," in *Catalysis, Science and Technology*, Berlin, Springer-Verlag, 1984, pp. 1-117.

[21] Z. Chen, Y. Yan and S. S. Elnashaie, "Catalyst Deactivation and Engineering Control for Steam Reforming of Higher Hydrocarbons in a Novel Membrane Reformer," *Chemical Engineering Science,* vol. 59, pp. 1965-1978, 2004.

[22] T. S. Christensen, "Adiabatic Prereforming of Hydrocarbons - An Important Step in Syngas Production," *Applied Catalysis A: General,* vol. 138, pp. 285-309, 1996.

[23] S. B. Zdonik, E. J. Green and L. P. Haller, "How Cracking Proceeds in the Ethylene-Pyrolysis Reaction," *Oil & Gas Journal,* vol. 65, no. 26, pp. 96-101, 1967.

[24] J. J. Spivey, "Deactivation of Reforming Catalysts," in *Fuel Cells: Technologies for Fuel Processing*, Elsevier, 2011, pp. 285-315.

[25] M. Ashrafi, C. Pfeifer, T. Proll and H. Hofbauer, "Experimental Study of Model Biogas Catalytic Steam Reforming: 2. Impact of Sulfur on the Deactivation and Regeneration of Ni-Based Catalysts," *Energy & Fuels,* vol. 22, pp. 4190-4195, 2008.

[26] J. Hepola and P. Simell, "Sulphur Poisoning of Nickel-based Hot Gas Cleaning Catalysts in Synthetic Gasification Gas II. Chemisorption of Hydrogen Sulphide," *Applied Catalysis B: Environmental,* vol. 14, pp. 305-321, 1997.

[27] B. H. Cooper and K. G. Knudsen, "Ultra Deep Desulfurization of Diesel: How an Understanding of the Underlying Kinetics can Reduce Investment Costs," in *Practical Advances in Petroleum Processing - Volume 1*, New York, Springer Science, 2006, pp. 297-316.

[28] S. K. Gangwal, "Desulfurization for Fuel Cells," in *Fuel Cells: Technologies for Fuel Processing*, Elsevier, 2011, pp. 317-360.

[29] S. H. Salem and A. Bakr, "Naphtha Desulfurization by Adsorption," *Industrial & Engineering Chemistry Research,* vol. 33, pp. 336-340, 1994.

[30] A. Bakr, S. H. Salem and H. S. Hamid, "Removal of Sulfur Compounds from Naphtha Solutions Using Solid Adsorbents," *Chemical Engineering & Technology,* pp. 342-347, 1997.

[31] D. W. Savage, B. K. Kaul, G. D. Dupre, J. T. O'Bara, W. E. Wales and T. C. Ho, "Deep Desulfurization of Distiallate Fuels". United States of America Patent US5454933 A, 3 Oct. 1995.

[32] M. Flytzani-Stephanopoulos and G. E. Voecks, "Autothermal Reforming of Aliphatic and Aromatic Hydrocarbon Liquids," *International Journal of Hydrogen Energy,* vol. 8, no. 7, pp. 539-548, 1983.

[33] R. D. Parmar, "A Combined Gas-Phase and Surface Reaction Mechanistic Model of Diesel Surrogate Reforming for SOFC Application," Queen's University, Kingston, ON, 2013.

[34] J. R. Rostrup-Nielsen, "Catalytic Steam Reforming," in *Catalysis, Science and Technology*, vol. 5, Berlin, Springer, 1983.

[35] R. Peters, "Fuel Processors," in *Handbook of Heterogeneous Catalysis*, Weinheim, Wiley-VCH, 2008, pp. 3045-3080.

[36] R. D. Parmar, A. Kundu and K. Karan, "Thermodynamic Analysis of Diesel Reforming Process: Mapping of Carbon Formation Boundary and Representative Independent Reactions," *Journal of Power Sources,* vol. 194, pp. 1007-1020, 2009.

[37] J. E. Kent and A. G. Dixon, "Steam Reforming of Biodiesel By-Product Glycerol," Worcester Polytechnic Institute, 2013.

[38] W. Ehrfeld, V. Hessel and H. Lowe, "Microreactors: New Technology for Modern Chemistry," *Organic Process Research & Development,* vol. 5, no. 1, p. 89, 2001.

[39] L. Kiwi-Minsker and A. Renken, "Microstructured Reactors for Catalytic Reactions," *Catalysis Today,* vol. 110, pp. 2-14, 2005.

[40] D. A. Reay, "Catalytic Combustion: Current Status and Implications for Energy Efficiency in the Process Industries," *Heat Recovery Systems and CHP,* vol. 13, no. 5, pp. 383-390, 1993.

[41] G. Kolios, J. Frauhammer and G. Eigenberger, "A Simplified Procedure for the Optimal Design of Autothermal Reactors for Endothermic High-Temperature Reactions," *Chemical Engineering Science,* vol. 56, pp. 351-357, 2001.

[42] G. Kolios, J. Frauhammer and G. Eigenberger, "Efficient Reactor Concepts for Coupling of Endothermic and Exothermic Reactions," *Chemical Engineering Science,* vol. 57, pp. 1505-1510, 2002.

[43] J. Frauhammer, G. Eigenberger, L. V. Hippel and D. Arntz, "A New Reactor Concept for Endothermic High-Temperature Reactions," *Chemical Engineering Science,* vol. 54, pp. 3661-3670, 1999.

[44] M. Zanfir and A. Gavriilidis, "Catalytic Combustion Assisted Methane Steam Reforming in a Catalytic Plate Reactor," *Chemical Engineering Science,* vol. 58, pp. 3947-3960, 2003.

[45] J. Aubin, L. Prat, C. Xuereb and C. Gourdon, "Effect of Microchannel Aspect Ratio on Residence Time Distributions and the Axial Dispersion Coefficient," *Chemical Engineering and Processing,* vol. 48, pp. 554-559, 2009.

[46] C. Y. Hsueh, H. S. Chu and W. M. Yan, "Numerical Study on Micro-Reformer Performance and Local Transport Phenomena of the Plate Methanol Steam Micro-Reformer," *Journal of Power Sources,* vol. 187, pp. 535-543, 2009.

[47] G. Arzamendi, P. M. Dieguez, M. Montes, M. A. Centeno, J. A. Odriozola and L. M. Gandia, "Integration of Methanol Steam Reforming and Combustion in a Microchannel Reactor for H2 Production: A CFD Simulation Study," *Catalysis Today,* vol. 143, pp. 25-31, 2009.

[48] L. Shi, D. J. Bayless and M. E. Prudich, "A CFD Model of Autothermal Reforming," *Internation Journal of Hydrogen Energy,* vol. 34, pp. 7666-7675, 2009.

[49] J. Thormann, L. Maier, P. Pfeifer, U. Kunz, O. Deutschmann and K. Schubert, "Steam Reforming of Hexadecane over a Rh/CeO2 Catalyst in Microchannels: Experimental and Numerical Investigation," *International Journal of Hydrogen Energy,* vol. 34, pp. 5108-5120, 2009.

[50] M. Karakaya and A. K. Avci, "Microchannel Reactor Modeling for Combustion Driven Reforming of Iso-Octane," *Internation Journal of Hydrogen Energy,* vol. 36, pp. 6569-6577, 2011.

[51] A. T. Naseri, B. A. Peppley and J. G. Pharoah, "Computational Analysis of the Reacting Flow in a Microstructured Reformer Using a Multiscale Approach," *AIChE Journal,* vol. 60, no. 6, pp. 2263-2274, 2014.

[52] O. Y. Caglar, C. D. Demirhan and A. K. Avci, "Modeling and Design of a Microchannel Reformer for Efficient Conversion of Glycerol to Hydrogen," *International Journal of Hydrogen Energy,* vol. 40, pp. 7579-7585, 2015.

[53] R. E. Hayes and S. T. Kolaczkowski, Introduction to Catalytic Combustion, Amsterdam: Gordon and Breach Science Publishers, 1997.

[54] M. J. Stutz and D. Poulikakos, "Optimum Washcoat Thickness of a Monolith Reactor for Syngas Production by Partial Oxidation of Methane," *Chemical Engineering Science,* vol. 63, pp. 1761-1770, 2008.

[55] M. Irani, "Resolving a Challenge in the Modeling of Hydrogen Production Using Steam Reforming of Methane in Monolith Reactors Using CFD Models," *Advances in Materials Physics and Chemistry,* vol. 2, no. 4B, pp. 248-252, 2012.

[56] N. Mladenov, J. Koop, S. Tischer and O. Deutschmann, "Modeling of Transport and Chemistry in Channel Flow of Automotive Catalytic Converters," *Chemical Engineering Science,* vol. 65, pp. 812-826, 2010.

[57] E. Massing, J. F. Brilhac, A. Brillard, P. Gilot and G. Prado, "Modelling of the Behaviour of a Three Way Catalytic Converter at Steady State Influence of the Propene Diffusion Inside the Catalytic Layer," *Chemical Engineering Science,* vol. 55, pp. 1707-1716, 2000.

[58] S. T. Kolaczkowski, R. Chao, S. Awdry and A. Smith, "Application of a CFD Code (Fluent) to Formulate Models of Catalytic Gas Phase Reactions in Porous Catalyst Pellets," *Chemical Engineering Research and Design,* vol. 85, no. 11, pp. 1539-1552, 2007.

[59] Fuel Cell Technologies Office, "Comparison of Fuel Cell Technologies," U.S. Department of Energy, 2016.

[60] H. Dhingra and B. A. Peppley, "Sensitivity Analysis of a 1 kW Diesel-Fuelled SOFC Generator: A Single and Paired-Variable Study," *Journal of Power Sources,* vol. 239, pp. 527-537, 2013.

[61] J. Palsson, J. B. Hanseb, N. Christiansen, J. U. Nielsen and S. Kristensen, *Solid Oxide Fuel Cells - Assessment of the Technology from an Industrial Perspective,* 2003.

[62] R. M. Ormerod, "Fuels and Fuel Processing," in *High Temperature Solid Oxide Fuel Cells: Fundamentals, Design and Applications*, Elsevier, 2003, pp. 333-361.

[63] M. C. Williams, "Fuel Cells," in *Fuel Cells: Technologies for Fuel Processing*, Elsevier, 2011, pp. 11-27.

[64] C. Rayment and S. Sherwin, "Introduciton to Fuel Cell Technology," University of Notre Dame, Notre Dame, 2003.

Chapter 3: Reformer and Fuel Cell System UniSim® Model

3.1: Introduction

This work will focus on optimizing a steam reformer and SOFC stack system to meet a test case remote community's electricity load. The RFC generates electricity from diesel, utilizing the already established remote community diesel supply network, and offers a more efficient alternative to diesel generators currently used in the majority of Canadian remote communities. The improved efficiency of a RFC will be demonstrated by comparing the environmental and economic performance of the RFC with that of diesel generator units.

3.2: Process Design

The proposed RFC process design is outlined in Figure 3-1. The RFC uses a steam reformer to convert diesel to syngas. Steam reforming was chosen for its higher hydrogen yield which would allow for the optimal system efficiency to be achieved. In addition, a SOFC stack was chosen because of its higher impurity resistance compared to low temperature fuel cells and because of its greater efficiency than other high temperature fuel cells. A higher impurity resistance meant that post-reformer processing units were not necessary, resulting in a simpler and more robust system for remote community operation. Furthermore, the use of a high temperature fuel cell allowed for the fuel cell stack exhaust to be used as a heat source for steam reforming. If a low temperature fuel cell was used then a large amount of fuel would need to be burned to provide heat for the steam reforming reaction resulting in much lower efficiency and likely making the system unfeasible.

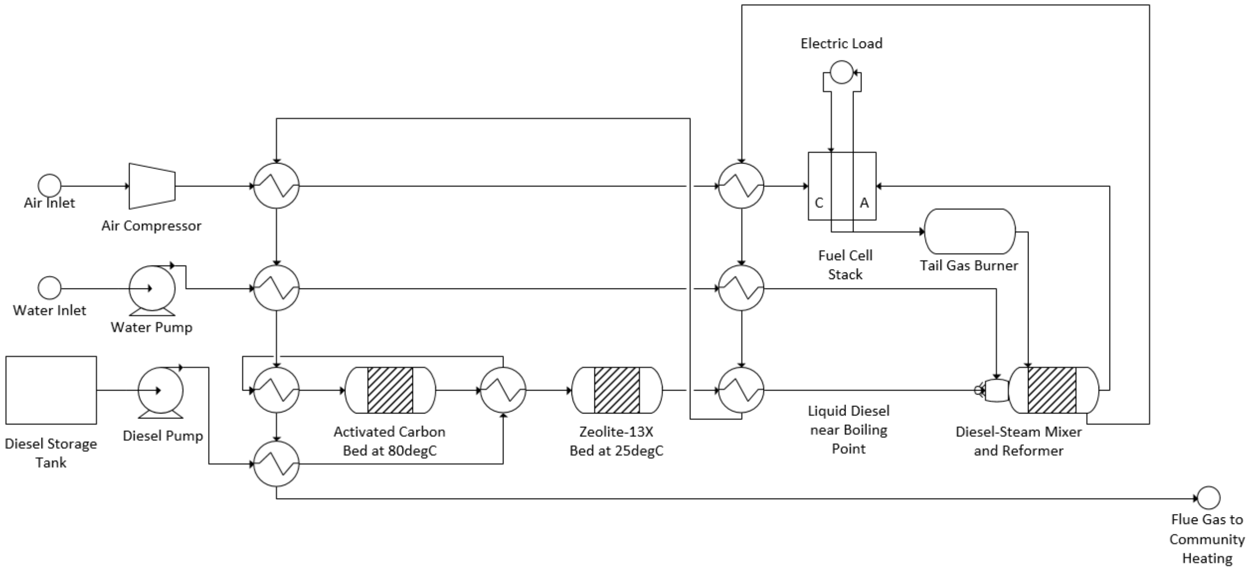

Figure 3-1: Diesel-fed steam reformer and SOFC stack system for remote community power generation.

The RFC includes the desulfurization of the diesel. Diesel desulfurization must still be performed despite greater sulfur resistance in high temperature fuel cells since the high sulfur content in diesel can still lead to catalyst deactivation in the reformer and fuel cell stack. For deep desulfurization Salem *et al.* proposed an activated carbon bed at 80°C for bulk sulfur compound removal, including some sterically hindered sulfur compounds. Salem *et al.* suggest following the activated carbon bed with a zeolite-13X bed at room temperature to achieve deep desulfurization [1, 2, 3].

After desulfurization the diesel is heated to just below boiling temperature before being vapourized by being mixed with high temperature steam immediately before entering the reformer. The steam can be formed either from water sourced locally or imported water stored on site. The diesel must be vapourized before entering the reformer because attempting to reform liquid aromatics on the reformer catalyst would result in catalyst deactivation through coke formation. However, the diesel must be vapourized immediately before the reformer since pyrolytic cracking can occur at high temperatures in the absence of catalyst activity [4]. Joensen and Rostrup-Nielsen have suggested using a pre-reformer operating at low temperatures (350-550°C) to convert larger hydrocarbons into C1 compounds without cracking so as to avoid coke precursors such as ethylene [5]. Low operating temperatures within the pre-reformer, however, increase the risk of gum formation, which is especially elevated in the presence of aromatics and their slow kinetics [6, 7]. Furthermore, using a pre-reformer would add another potential point of failure, further complicating a system that must be robust so as to achieve longevity in Canadian remote communities. Therefore, a pre-reformer was not implemented in the design.

The diesel-steam mixture enters the reformer, a catalytic plate reactor, with hot flue gas from the fuel cell stack exhaust providing the thermal energy needed for endothermic steam reforming. The syngas produced by the reformer enters the SOFC stack anode while hot air enters the cathode. The cathode half-cell reaction (Equation 3-1) produces a current as well as oxygen ions that diffuse through the fuel cell electrolyte towards the anode. The anode half-cell reaction is shown in Equation 3-2. The overall reaction is exothermic and is shown in Equation 3-3.

$$\frac{1}{2}O_2 + 2e^- \rightarrow O^{2-} \tag{3-1}$$

$$H_2 + O^{2-} \rightarrow H_2O + 2e^- \tag{3-2}$$

$$H_2 + \frac{1}{2}O_2 \rightarrow H_2O \qquad \Delta H^0 = -242\ \text{kJ/mol} \tag{3-3}$$

The exhaust from the fuel cell stack anode and cathode are fed into a tail gas burner where unused hydrogen and methane are combusted with leftover oxygen to increase the temperature of the flue gas. As mentioned above, the flue gas is utilized by the system to heat the reformer and preheat the reactants. A potential heat recovery system is presented above in Figure 3-1.

3.3: Model Design

The model presented in this work was created using Honeywell's UniSim® Design Suite. The Peng-Robinson-Soave-Vera (PRSV) property package was used with enthalpy specified using equations of state [8]. The PRSV property package was designed to be accurate for chemical systems. Honeywell generally recommends the use of the Peng-Robinson (PR) property package because of the extra work that Honeywell puts in to make the PR package accurate. The PRSV package is as accurate as the PR package, with the added advantage of more accurately modeling phase behaviours for hydrocarbon systems, at the cost of longer computation times.

3.3.1: System Feed

The air, water, and diesel feed were assumed to be at atmospheric pressure and 25^{o}C. Hexadecane was used as a diesel surrogate in order to more easily couple the results with future reformer modeling work completed in ANSYS Fluent. Hexadecane was chosen because it is the predominant hydrocarbon found in diesel [9]. It was assumed that there was no sulfur in the hydrocarbon feed.

3.3.2: Reformer Modeling

A zero dimensional model was used for the reformer. The reformer was modeled as a conversion reactor (a unit operation available in UniSim® that defines chemical reactions based on the extent of reactant conversion) where all of the hexadecane feed was consumed, along with the appropriate amount of steam, to produce carbon monoxide and hydrogen according to Equation 3-4. A Gibbs reactor (a unit operation available in UniSim® that finds the equilibrium composition of a mixture by minimizing its Gibbs free energy) was then used to calculate the equilibrium composition of the syngas, with the water-gas shift and methanation reactions assumed to be at equilibrium. The reformer was assumed to be isothermal, with the tail gas burner flue gas providing the necessary thermal energy.

The steam reformer operating temperature range was limited by the risk of carbon formation. Work by Parmar *et al.* shows that carbon formation within a steam reformer can be significantly reduced by staying above the carbon formation boundary temperature for a given steam to carbon ratio (Table 3-1) [10].

$$C_{16}H_{34} + 16H_2O \rightarrow 16CO + 33H_2 \qquad \Delta H = 2{,}475 \text{ kJ/mol} \qquad (3\text{-}4)$$

Table 3-1: Steam Reformer Minimum Operating Temperature to Avoid Carbon Formation [46]

H_2O/C	Temperature (°C)
1.00	974.9
1.25	711.1
1.50	649.4
1.75	583.4
2.00	238.3

3.3.3: Fuel Cell Modeling

The SOFC stack was modeled in zero dimensions using the validated study conducted by Costamagna *et al.* for a cathode-supported integrated-planar cell design [11]. The SOFC model equations are presented in Table 3-2 and Table 3-3, with the fuel cell parameters presented in Table 3-4.

The Nernst voltage is the cell open circuit voltage. Activation losses, which are minimal in high temperature fuel cells such as SOFCs, occur because reactants must overcome an energy threshold before reacting [12]. Ohmic losses occur because of resistance, proportional to current density along the electron and ionic pathways. Concentration losses occur at high current densities because of mass transport limitations that result in insufficient reactants reaching the electrocatalyst sites in the anode and cathode layers [13].

Table 3-2: SOFC Current and Voltage Equations [11]

Current	$I_{H_2} = \mu_{H_2} n_{e,a} \frac{\dot{n}_{H_2}}{cell} F$ $I_{O_2} = \mu_{O_2} n_{e,c} \frac{\dot{n}_{O_2}}{cell} F$ $I = \min(I_{H_2}, I_{O_2})$ $i = I/A$
Nernst Voltage [14, 15]	$V_{Nernst} = \frac{-\Delta G_T^0}{n_e F} + \frac{RT}{n_e F}\ln\left(\frac{P_{H_2}P_{O_2}^{0.5}}{P_{H_2O}}\right)$ $\Delta G_T^0 = T\left(\frac{\Delta G_{298}^0 - \Delta H_{298}^0}{T^0} + \frac{\Delta H_T^0}{T}\right)$ $\Delta H_T^0(\frac{kJ}{mol}) = C_1\left(\frac{T(K)}{1000}\right) + \frac{C_2}{2}\left(\frac{T(K)}{1000}\right)^2 + \frac{C_3}{3}\left(\frac{T(K)}{1000}\right)^3 - \frac{C_4}{4}\left(\frac{T(K)}{1000}\right)^4 - C_5\left(\frac{T(K)}{1000}\right)^{-1} - C_6$
Real Voltage	$V_{real} = V_{Nernst} - V_{act,c} - V_{act,a} - V_{ohm} - V_{conc,c} - V_{conc,a}$

Table 3-3: SOFC Voltage Loss Equations [11]

Activation Losses	$V_{act,x} = \frac{2RT}{n_e F} \sinh^{-1}\left(\frac{i}{2i_{0,x}}\right)$ $i_{0,c} = \gamma_c \left(\frac{P_{O_2}}{P_{ref}}\right)^{0.25} \exp\left(-\frac{E_c}{RT}\right)$ $i_{0,a} = \gamma_a \left(\frac{P_{H_2}}{P_{ref}}\right)\left(\frac{P_{H_2O}}{P_{ref}}\right) \exp\left(-\frac{E_a}{RT}\right)$
Ohmic Losses	$V_{ohm} = Ri$ $R = CJ\left(\coth(J) + B\left(J - 2\tanh\left(\frac{J}{2}\right)\right)\right)$ $C = \rho_c t_c + \rho_{ccc} t_{ccc} + \rho_{el} t_{el} + \rho_a t_a + \rho_{cca} t_{cca}$ $J = \frac{X}{L}$ $L = \sqrt{\frac{\rho_{el} t_{el}}{\left(\frac{t_{cca}}{\rho_{cca}} + \frac{t_a}{\rho_a}\right)^{-1} + \left(\frac{t_{ccc}}{\rho_{ccc}} + \frac{t_c}{\rho_c}\right)^{-1}}}$ $B = \frac{E}{(1+E)^2}$ $E = \left(\frac{t_{cca}}{\rho_{cca}} + \frac{t_a}{\rho_a}\right)^{-1} \left(\frac{t_{ccc}}{\rho_{ccc}} + \frac{t_c}{\rho_c}\right)$ $\rho_x = \left(\beta_{x,1} \exp\left(-\frac{\beta_{x,2}}{T}\right)\right)^{-1}$
Concentration Losses	$V_{conc,c} = -\frac{RT}{2n_e F} \ln\left(\frac{1}{x_{O_2}} - \left(\frac{1}{x_{O_2}} - 1\right) exp\left(\frac{iRTt_c}{2n_e F * D_{eff,c} P}\right)\right)$ $V_{conc,a} = -\frac{RT}{n_e F} \ln\left(\frac{1 - \left(\frac{iRTt_a}{n_e F * D_{eff,a} P_{H_2}}\right)}{1 + \left(\frac{iRTt_a}{n_e F * D_{eff,a} P_{H_2O}}\right)}\right)$

Table 3-4: SOFC Constants and Operating Parameters

			Reference
μ_{H_2}	Fuel utilization	0.8	-
μ_{O_2}	Oxygen utilization	0.4	-
T	Temperature	K	-
$n_{e,a}$	Electrons exchanged per mole of hydrogen	2	-
$n_{e,c}$	Electrons exchanged per mole of oxygen	4	-
$\dot{n}_{H_2}$	Molar flow rate of hydrogen	mol/s	-
$\dot{n}_{O_2}$	Molar flow rate of oxygen	mol/s	-
F	Faraday's Constant	96,485 C/mol	-
A	Bloom Box active surface area	100 cm^2	[16]
R	Universal Gas Constant	8.314 J/mol-K	-
n_e	Number of electrons exchanged	2	[11]
ΔG_{298}^{0}	Standard Gibbs free energy of steam	-228,590 J/mol	[14]
ΔH_{298}^{0}	Standard enthalpy of steam	-24,.830 J/mol	[14]
T^0	Standard temperature	298 K	[14]
C_1	Steam enthalpy constant	30.092	[15]
C_2	Steam enthalpy constant	6.832514	[15]
C_3	Steam enthalpy constant	6.793435	[15]
C_4	Steam enthalpy constant	2.53448	[15]
C_5	Steam enthalpy constant	0.082139	[15]
C_6	Steam enthalpy constant	250.881	[15]
γ_c	Cathode pre-exponential factor	$7*10^8$ A/m^2	[11]
γ_a	Anode pre-exponential factor	$5.5*10^8$ A/m^2	[11]
E_c	Cathode activation energy	120,000 J/mol	[11]
E_a	Anode activation energy	100,000 J/mol	[11]
P_{ref}	Reference pressure	101.3 kPa	[11]
t_c	Cathode thickness	30 µm	[11]
t_{ccc}	Cathode current collector thickness	300 µm	[11]
t_a	Anode thickness	20 µm	[11]
t_{cca}	Anode current collector thickness	200 µm	[11]
t_{el}	Electrolyte thickness	20 µm	[11]
ρ_{cca}	Anode current collector resistivity	$2*10^{-4}$ Ωm	[11]
ρ_c	Cathode resistivity	$7.8*10^{-5}$ Ωm	[11]
$\beta_{a,1}$	Anode resistivity coefficient 1	7,800 $\Omega^{-1}m^{-1}$	[11]
$\beta_{a,2}$	Anode resistivity coefficient 2	1,290 K	[11]
$\beta_{el,1}$	Electrolyte resistivity coefficient 1	20,500 $\Omega^{-1}m^{-1}$	[11]
$\beta_{el,2}$	Electrolyte resistivity coefficient 2	9,030 K	[11]
$\beta_{ccc,1}$	Cathode current collector resistivity coefficient 1	33,770 $\Omega^{-1}m^{-1}$	[11]
$\beta_{ccc,2}$	Cathode current collector resistivity coefficient 2	1,130 K	[11]
X	Cell pitch length	1 cm	[11]
x_i	Mole fraction of component i	-	[11]
$D_{eff,c}$	Effective diffusion coefficient at the cathode	$5.4*10^{-6}$ m^2/s at 1,000°C	[11]
$D_{eff,a}$	Effective diffusion coefficient at the anode	$2.1*10^{-5}$ m^2/s at 1,000°C	[11]

The fuel cell stack was modeled by separating the feed stream into anode and cathode streams. A spreadsheet was used to model the consumption of hydrogen and oxygen in each electrode stream as well as to calculate an initial estimation of current. The model operated with excess air in the cathode so that the anode current was the limiting factor and no hydrogen was needlessly wasted. A Gibbs reactor was then used to make an estimation of the reaction extent for the WGS and methanation reactions in anode stream. The average temperature of the fuel cell stack and the average partial pressures of the reactants were taken between the electrode inlets and outlets to be used to calculate voltage. The initial current estimation was then modified by adding the hydrogen generated in the WGS reaction to the total hydrogen feed, thus increasing the current. Finally, the estimated current, voltage, and average fuel cell stack temperature were changed so that they matched the UniSim® model outputs. The average fuel cell stack temperature was limited to between 650^{o}C to 1,000^{o}C in accordance with SOFC operating temperature ranges [17].

3.3.4: Tail Gas Burner Modeling

The tail gas burner was modeled by combining a conversion reactor with a Gibbs reactor. The conversion reactor used the leftover oxygen to combust all unused hydrogen and methane. The Gibbs reactor brought the gas mixture to equilibrium concentration.

3.4: Model Results

Different RFC model parameters were tested to achieve optimum electrical efficiency for a 100 kW system, including parasitic electricity losses from pump and compressor operation. Equation 3-5 was used to calculate the system electrical efficiency from the hexadecane lower heating value of 43.33 MJ/kg. Furthermore, the CHP efficiency for high quality heat (heat from a stream with a temperature of at least 100^{o}C) was calculated by adding a thermal work term to the numerator of Equation 3-5.

$$Electrical\ Efficiency = \frac{Electrical\ Work - Parasitic\ Losses}{\dot{m}_{fuel} * LHV_{fuel}} \qquad (3\text{-}5)$$

The model parameters that were tested were: steam to carbon ratio, steam and air temperature, and system pressure. During model testing it was assumed that pressure remained constant throughout the system and that the minimal acceptable system pressure was 120 kPa. To determine the optimal parameter value a rough cost analysis was conducted for a 100 kW system, with the parameter values chosen based on the best payback period. The rough cost analysis determined the project capital cost by equating it to the fuel cell stack capital cost. The number of cells per 100 kW stack was calculated from the parameters and the cost per cell was estimated to be $178.57. The cell cost was estimated from the Bloom Box which costs $750,000 for a 100 kW 4,200 cell stack [16, 18]. The payback period was based on the annual cost of diesel consumed. The cost of diesel was estimated to be $1.5/kg ($1.248/L), similar to the 2011 average cost of diesel fuel for Northern Ontario [19]. The parameters listed above were optimized from the base case presented in Table 3-5.

Table 3-5: RFC UniSim® Base Case Parameters

Molar Flow (mol/h-cell)	*Water*	0.50
	Diesel	0.16
	Air	3.10
Molar S/C Ratio		2.22
Temperature (^oC)	*Steam*	750.00
	Air	850.00
	Reformer	587.40
	SOFC Avg.	852.45
Pressure (kPa)		120
Cells per 100 kW		5,385
Electrical Efficiency (%)		42.27
CHP Efficiency (%)		64.52
Estimated Payback Period (yrs)		33.50

3.4.1: Steam to Carbon Ratio

Increasing the steam to carbon ratio resulted in an exponential rise in system electrical efficiency (Figure 3-2) and also acted to reduce the risk of carbon formation. More steam in the reformer and fuel cell stack resulted in increased hydrogen selectivity in the WGS reaction, increasing the amount of hydrogen available for electricity production. Excessively high steam to carbon ratios, however, had less of an impact on hydrogen selectivity and acted more to hinder fuel cell operation by reducing the Nernst potential and increasing fuel cell losses (Table 3-6). Moreover, CHP efficiency was found to be inversely proportional to the steam to carbon ratio since the extra thermal energy demand of a higher steam to carbon ratio was not adequately offset by the improved system electrical efficiency.

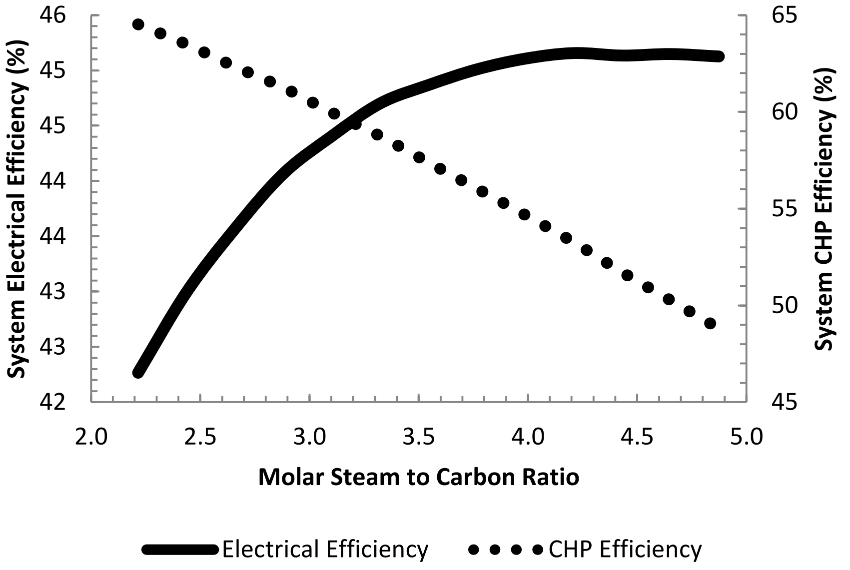

Figure 3-2: Effect of steam to carbon ratio on system electrical and CHP efficiencies.

Figure 3-2 shows the effects on RFC performance of increasing the steam to carbon ratio by increasing the steam flow rate. As shown in Figure 3-3, the system electrical efficiency can be improved once the crest of Figure 3-2 has been reached by increasing the steam to carbon ratio through the reduction of the fuel flow rate, which in turn reduces polarization losses while increasing the steam to carbon ratio. Reducing the fuel flow rate, however, resulted in reduced power output per cell. A higher cell count, and a greater capital investment, was required when the power output per cell was reduced. Therefore, repeatedly reducing the fuel flow rate during the UniSim® trials did not indefinitely result in a more cost effective system. Overall, a molar steam to carbon ratio of 4.67 was used with a total diesel flow rate of 17.51 kg/h and a SOFC count of 5,948.

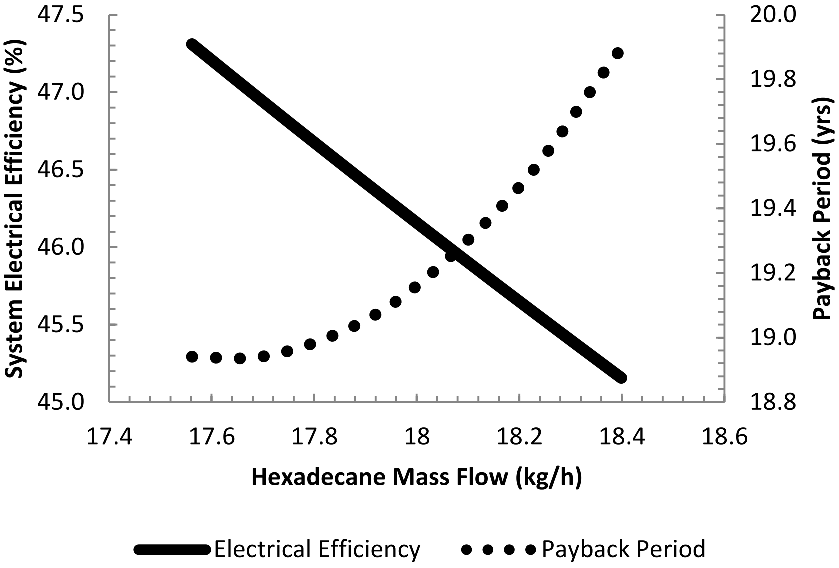

Figure 3-3: Impact of varying system hexadecane mass flow while keeping a constant steam flow rate.

3.4.2: Steam and Air Temperature

Steam temperature impacted reformer temperature and hydrogen selectivity. Higher temperatures resulted in lower hydrogen selectivity for the WGS reaction. Steam temperature also had an effect on the fuel cell temperature, with higher steam temperatures resulting in higher fuel cell temperatures. Higher fuel cell temperatures in turn resulted in lower Nernst voltages, lower activation and ohmic losses, and higher concentration losses (Table 3-6). The result was that increasing the steam temperature was beneficial as long as the reductions in activation and ohmic losses outweighed the higher concentration losses and lower Nernst voltage. The optimal steam temperature was found to be 800^{o}C given the RFC operating parameters and the reactant feed. A larger reactant flow rate, however, would be subject to higher concentration losses and would benefit from lower fuel cell stack operating temperatures. Moreover, air temperature only impacted fuel cell temperature, resulting in air temperature having a similar relationship with system efficiency as steam temperature, with temperature increases beyond 900°C proving detrimental.

3.4.3: System Pressure

Increasing the system pressure resulted in improved fuel cell performance (Table 3-6), but had a negative impact on system efficiency. Higher system pressure had a negative impact on system performance because of increased parasitic electricity losses attributable to the added power requirements for system pumps and compressors. A 17% increase in system pressure, from 120 kPa to 140 kPa, resulted in a 98% increase in parasitic electricity losses and a 0.56% decrease in electrical efficiency. A system pressure of 120 kPa was therefore used for the optimized model.

Table 3-6: SOFC Voltage Sensitivity to Parameter Change

Parameter	Parameter Change	Nernst Potential	Activation Losses	Ohmic Losses	Concentration Losses
Steam to Carbon Ratio	+	-	+	0	+
Reactant Flow Rate	+	0	+	+	+
Temperature	+	-	-	-	+
Pressure	+	+	-	0	-

3.5: Optimized System Case

The optimized parameters for the RFC are shown in Table 3-7. A more detailed stream table of the optimized case is provided in Appendix A. The optimized case provides the best payback period based on electrical efficiency at the expense of a significant decrease in CHP efficiency caused by the need to vapourize a significantly larger amount of water. CHP efficiency, however, was not accounted for in the rough cost analysis. When focusing only on the electrical efficiency it can be seen that a 5% improvement in electrical efficiency can nearly half the estimated payback period.

Table 3-7: RFC UniSim® Optimized Case Parameters for a 100 kW System

		Base Case	Optimized Case
Mass Flow (kg/h)	*Water*	48.51	91.08
	Diesel	19.66	17.51
	Air	483.52	482.48
Molar S/C Ratio		2.22	4.67
Temperature (°C)	*Steam*	750.00	800.00
	Air	850.00	900.00
	Reformer	587.40	692.90
	SOFC Avg.	852.45	946.40
Pressure (kPa)		120	120
Cells per 100 kW		5,385	5,948
Electrical Efficiency (%)		42.27	47.45
CHP Efficiency (%)		64.52	49.43
Estimated Payback Period (yrs)		33.50	18.66

3.6: System Analysis

3.6.1: Test Case Remote Community

A test case remote community located in Ontario with a peak demand of 150 kW was used to compare the performance of a diesel generator with that of the proposed RFC. For safety reasons a remote community cannot have a peak demand that exceeds 75% of their total generation capacity [20]. Therefore, a 200 kW diesel generator setup was compared to a 200 kW fuel cell stack for the purpose of supplying electricity to a community with a peak demand of 150 kW. The test case community's electricity demand curves for summer and winter (Figure 3-4) were created using the electricity demand curves composed by Arriaga *et al.* for a remote community in Ontario [21]. The test community's annual electricity demand is around 850 MWh (around 0.09% of the 964 GWh annual Canadian remote community electricity demand met using fossil fuel generation), equivalent to a remote community with a population of between 100 and 200 people [22]. The test community's average electricity load is 97.3 kW, close to the 100 kW load for which the RFC system was optimized.

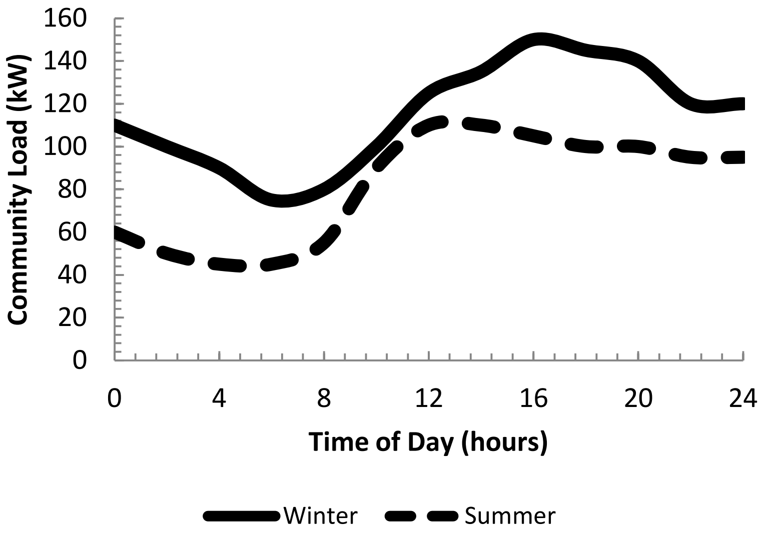

Figure 3-4: Test case remote community electricity demand curves.

The remote community's diesel price was based on the current and forecasted delivered diesel price in the Northwest Ontario First Nation Transmission Planning Committee report [23]. Emissions from diesel transportation to the test community were based on the Ontario remote community of Kasabonika Lake. Kasabonika Lake is only accessible by winter roads during February and March and by air during the rest of the year [24]. The nearest service centre to Kasabonika Lake is 400 km away, which is from where the diesel is assumed to originate for the purposes of calculating carbon dioxide emissions from diesel transportation [25].

The winter roads allow for 36 ton loads on semi-trailer trucks [21]. Diesel consumption by semi-trailer trucks is approximately 6.5 US gallons per thousand ton-mile, with carbon dioxide emissions of 10.15 kg/US gallon [26, 27]. The maximum payload for air access was determined using information from the Northern Ontario remote community air transport company Cargo North. Cargo North uses the Basler BT-67 airplane, allowing for a maximum fuel load of 6,200 L for a 200 nautical mile flight (duration of 1 hour), which is approximately the distance from Kasabonika Lake to the nearest service centre [28]. A standard cruise speed for the Basler BT-67 would result in fuel consumption of 145 US gallons/hour (an average between a fully loaded and an empty Basler BT-67) with 9.57 kilograms of carbon dioxide emitted per US gallon of fuel [26, 29].

3.6.2: Reformer and Fuel Cell System Performance *vs.* Diesel Generator Performance

The RFC efficiency curves were adjusted from the optimized case, maintaining a constant cell count and steam to carbon ratio while varying diesel, air, and steam flow rates to meet the community's changing electricity demand (see Appendix A for feed flow rates, operating temperatures, and efficiency values). Furthermore, the RFC efficiency was altered to take into account efficiency losses experienced during power conditioning. The conversion of the RFC direct current power to alternating current power was assumed to be conducted with a state-of-the art 95% efficient power conditioner [30, 31].

Diesel generator efficiency curves were acquired using Trnsys 17. Three 200 kW diesel generator setups were tested against the RFC. The first diesel generator setup (GEN1) consists of one 200 kW generator. The second diesel generator setup (GEN2) consists of two 100 kW generators. The last diesel generator setup (GEN3) consists of five 40 kW generators. For each diesel generator setup the community's load is evenly distributed across as few active generators as necessary (*e.g.* a 120 kW load would see the first generator setup operating with one generator at 120 kW, the second generator setup would see both generators operating at 60 kW, the third generator setup would see three generators operating at 40 kW and two idle generators). The above setup provided more efficient diesel generator operation than if the community's load was distributed evenly among all available generators. Furthermore, the above method was also used to minimize low load operation (loading factors below 40% of the generators maximum continuous rating) since persistent low load operation can lead to generator failure [32, 33].

Electrical efficiencies for the three diesel generator setups and the RFC are illustrated in Figure 3-5. The diesel generators setups generally achieve the best efficiencies when operating at higher loads, whereas the RFC tends to achieve optimal efficiencies when operating at lower loads. The improved performance of fuel cells at lower loads is a benefit for remote community electricity generation, where the average load is around 50% of the total generating capacity [21]. Furthermore, improved efficiency at lower loads allows the RFC to harmoniously mesh with intermittent renewable energy grid penetration.

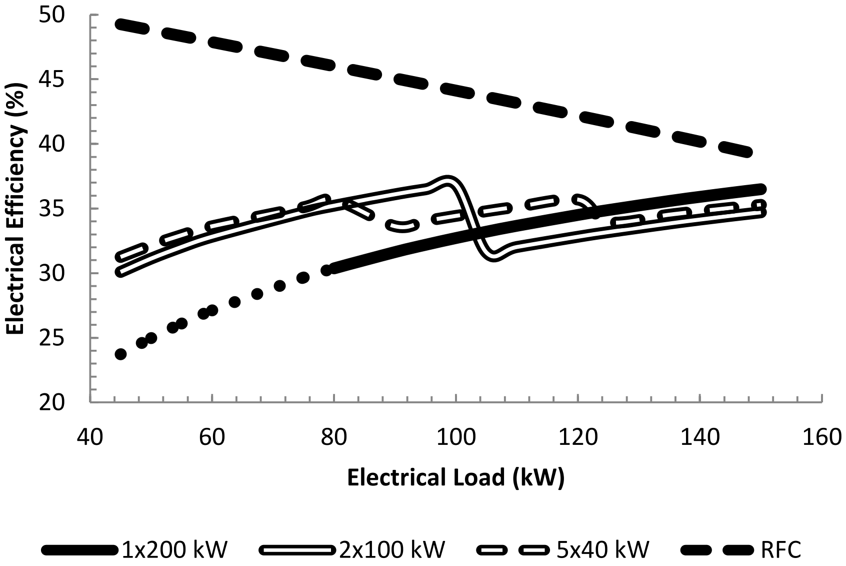

Figure 3-5: Electrical efficiencies for three different diesel generator setups and the RFC. The dotted line represents a region of low load operation for the 1x200 kW system.

GEN1 exhibits a smooth efficiency versus load curve, where electrical efficiency increases logarithmically with electrical load. GEN1, however, is the only generator setup that experiences low load operation for electrical loads under 80 kW (2 hours/day during the winter and 10 hours/day during the summer). GEN2 and GEN3 start with significantly higher electrical efficiencies than GEN1 thanks to higher generator loading factors. GEN2 and GEN 3, however, experience sharp efficiency drop-offs each time an additional generator is brought online (at 100 kW for GEN2 and at 80 kW and 120 kW for GEN3).

These sharp efficiency drop-offs are caused by a sudden reduction in individual generator loading factors caused by dividing the electrical load between the previously operating generators as well as the generator that was just brought online.

The electrical efficiencies of the RFC and GEN1 are compared in Figure 3-6 using the test case remote community's electricity demand curves. RFC versus GEN2 and RFC versus GEN3 plots can be found in Appendix B. All three RFC versus GEN plots are similar, with the diesel generator setup efficiencies never surpassing RFC efficiencies. The maximum RFC efficiency experienced by the test remote community is 50.3% and the minimum is 40.0%, resulting in a net annual efficiency of 45.30%. The maximum GEN efficiency experienced by the test remote community is 36.49% during GEN1 winter operation and GEN2 summer operation, the minimum is 23.7% during GEN1 summer operation. At the 200 kW safety regulated maximum generating capacity the RFC has an efficiency of 34.4%, GEN1 has an efficiency of 38.7%, GEN2 has an efficiency of 36.8%, and GEN3 has an efficiency of 35.7%. The 200 kW system efficiencies further underline that diesel generator setups are better suited for prolonged operation at maximum capacity.

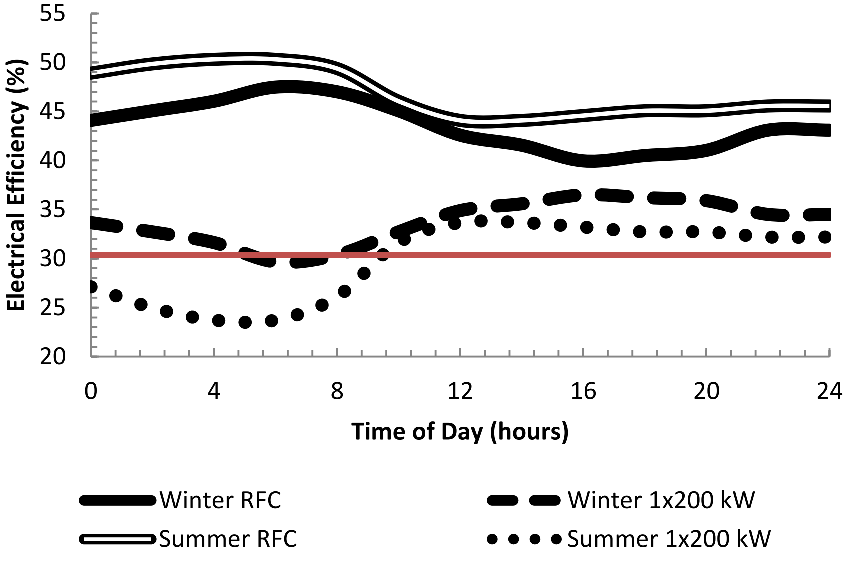

Figure 3-6: Summer and winter electrical efficiencies for the RFC and the 200 kW diesel generator setup. The area under the red line represents low load operation for the 200 kW diesel generator.

3.6.3: Environmental Analysis

Table 3-8 summarizes the environmental results of testing diesel generator setups against the RFC for the test case remote community. Replacing any of the three diesel generator setups with the RFC system would provide substantial efficiency improvements for the test case remote community, with diesel savings ranging between 57.8 kiloliters per year for GEN3 to 73.2 kiloliters per year for GEN1. These diesel savings would have the effect of reducing the annual number of supply trips, further augmenting greenhouse gas emission reductions. Moreover, the need to transport and store less diesel reduces the risk of fuel spills. Overall, replacing all of the Canadian remote community diesel generator systems with RFCs would result in annual CO_2 equivalent savings upwards of 175 kilotons (calculated from GEN3), the equivalent of taking 37,000 cars off of the road or preserving over 165,000 acres of forest [34].

Table 3-8: Test Case Remote Community Performance of RFC versus Diesel Generator Setups

	RFC	GEN1 (1x200 kW)	GEN2 (2x100 kW)	GEN3 (5x40 kW)
Annual Net Efficiency	45.3%	31.7%	33.9%	34.2%
Diesel CO_2 eq. Emissions (t/yr)	515.9	712.3	679.8	671.0
Air Trips/Year	26	35	34	33
Truck Trips/Year	1	2	2	2
Total CO_2 eq. Emissions (t/yr)	589.2	811.72	776.4	764.9

3.6.4: Economic Analysis

For the purpose of this economic analysis all values are in 2016 CAD, with the CAD and USD assumed to be equally valued.

3.6.4.1: Capital Costs

The total cost of an on-grid project can be broken down into 76% material capital costs, %18 installation costs, and 6% project management costs. Conducting off-grid and remote projects, however, results in added costs stemming from additional project difficulties: such as remote equipment transportation, accessibility of spare parts, the creation of a remote work force, contingency, and more. Arriaga *et al.* estimate that any project conducted in Kasabonika Lake, the basis for the test case community, would be approximately 2.25 times more expensive than an on-grid project [21].

3.6.4.1.1: Reformer and Fuel Cell System Capital Costs

The capital costs for the different RFC setups were calculated by adding the cost of the fuel cell stack to the cost of the RFC. Battelle Memorial Institute conducted a manufacturing cost analysis for both 1 kW and 5 kW diesel RFCs [35]. The materials capital cost of a 200 kW system was linearly extrapolated from Battelle Memorial Institute's 1 kW and 5 kW system cost estimations, with the fractional cost breakdown per balance of plant component estimated to be the same as the 5 kW system cost breakdown. The cost of the 200 kW system was estimated to be $87,705, with power conversion comprising 14.25% of the total system cost. Battelle Memorial Institute also suggested adding a 50% sales markup to the calculated cost, leading to a total 200 kW system cost of $131,557 with power conversion and a cost of $112,810 without [35].

The costs for two different RFCs were calculated. The difference between the two RFC setups was the selection of the SOFC stack. One system used the Bloom Energy Bloom Box and the other system used the Redox Power Systems Redox Cube. Both fuel cell stacks include fuel reformers for natural gas. The capital cost of a fuel processing unit, however, was still included in the capital cost calculations because of the additional reformer considerations associated with the much more difficult process of diesel reforming.

Bloom Energy's Bloom Box

The Bloom Energy Bloom Box is a SOFC stack that had its press debut in 2010 and costs between $7,000/kW and $8,000/kW [18]. Assuming an average Bloom Box cost of $7,500/kW, the required 200 kW stack would cost $1.5 million. $1.5 million is greater than the $1.1 million value that was used for the rough cost estimation of the optimized RFC in section 3.5: Optimized System Case. The Bloom Box comes with the necessary conversion to alternating current [18]. Therefore, the 200 kW system capital cost, including the price of the Bloom Box fuel cell stack, is $1.613 million. After installation at the test case remote community, the total project capital cost becomes $4.775 million.

Redox Power Systems' Redox Cube

Redox Power Systems has claimed that they can produce a SOFC stack, the Redox Cube, at a cost of $1,000/kW. Using a Redox Cube would result in a total stack cost of $200,000 for the RFC [36]. The Redox Cube, however, is still in the prototype phase and represents a futuristic cost approximation for SOFC stacks [37]. Furthermore, the Redox Cube cost does not include power conditioning. The 200 kW system capital cost, including the price of the Redox Cube fuel cell stack, is $331,557. After installation at the test case remote community, the total project capital cost becomes $981,582.

3.6.4.1.2: Capital Costs for Diesel Generator Systems

The capital cost for the diesel generator system was \$23,975 for GEN1 [38], \$31,498 for GEN2 [39], and \$52,495 for GEN3 [40]. After installation at the test case remote community, the total project capital cost becomes \$70,979 for GEN1, \$93,251 for GEN2, and \$155,413 for GEN3.

3.6.4.2: Operating Costs

Operating costs for the proposed power systems include diesel consumption, system maintenance, and system component replacement at the end of each component's lifecycle. The system was assumed to be installed at the end of 2017, with the first operating year being 2018. The system was also assumed to be operational for 20 years (until the end of 2037).

3.6.4.2.1: Diesel Consumption

The 2014 Northwest Ontario First Nation Transmission Planning Committee draft technical report and business case used information from the US Energy Information Administration's Annual Energy Outlook Early Release 2013 report to forecast the cost of delivering diesel to Ontario's remote communities from 2014 (\$1.49/L) to 2054 (\$2.58/L) [23]. For the purpose of this study, the diesel commodity price and the diesel transportation cost were calculated using a quadratic function (Equation 3-6) based on the information gleaned from the Northwest Ontario First Nation Transmission Planning Committee's report [23].

$$Delivered\ Diesel\ Cost\ \left(\frac{\$}{L}\right) = 5.00 \cdot 10^{-5} \cdot yr^2 - 0.18 \cdot yr + 152.53 \tag{3-6}$$

The total expenditure on diesel over time for each system is illustrated in Figure 3-7. From Figure 3-7 it is evident that the potential diesel savings associated with RFC operation are significant. More marginal diesel savings can be achieved by using multiple smaller diesel generators instead of one large one so as to increase diesel generator loading factors and efficiencies.

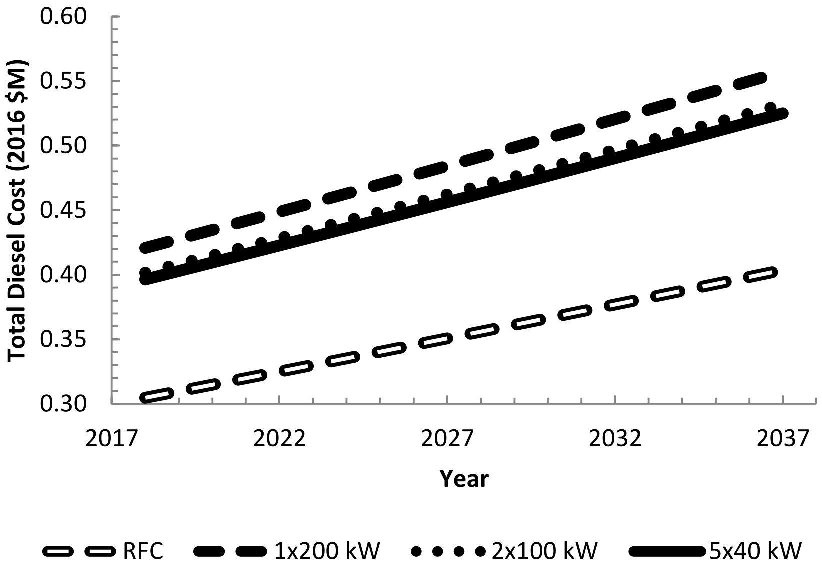

Figure 3-7: Total diesel expenditure for different system options over the lifecycle of the test case community diesel generation system.

3.6.4.2.2: System Maintenance

System maintenance for the diesel generators costs on average approximately $0.014/kWh, resulting in an annual maintenance cost of $11,932 [41]. System maintenance for the RFC system costs on average approximately $0.01/kWh, resulting in an annual maintenance cost of $8,523 [35].

Diesel generators, SOFCs, reformers, and desulfurizer units have lifecycles equivalent to around 5 years of continuous operation [42, 43, 44, 45]. Over a 20 year project lifespan the above system components would need to be replaced three times (once every 5 years). The GEN2 and GEN3 setups, however, do not continuously use every available generator. Therefore, assuming the hours of operation for the individual generators are kept relatively equal, the GEN2 generators would have to be replaced every 7 years and the GEN3 generators would have to be replaced every 8.5 years. The result is that the GEN2 and GEN3 generators have to be replaced twice during the course of the project. The replacement costs per system are summarized in Table 3-9.

Table 3-9: Replacement Costs for the Proposed Systems

Bloom Box	$1,503,508
Redox Cube	$203,508
GEN1 (1x200 kW)	$23,975
GEN2 (2x100 kW)	$31,498
GEN3 (5x40 kW)	$52,495

3.6.4.3: Cost Comparison

The cost breakdowns for the various power systems compared in this document can be found in Table 3-10. The Bloom Box RFC proves to be the least economic option. Over the 20 year lifespan of the project, the Redox Cube RFC is the most economic option, offering cost reductions ranging between $0.8 million and $1.3 million depending on the generator setup for the test case remote community over the project lifespan. Extrapolating the data out to all fossil fuel-reliant Canadian remote communities results in total savings over 20 years of more than $978 million, without taking future SOFC technology advancement into account.

Within the generator systems, the GEN1 system proved to be the least effective, whereas the GEN2 and GEN3 systems were equally effective at significantly reducing operating costs from GEN1 levels. Furthermore, for the test case community, GEN1 would have to occasionally operate at low loading factors which would have a negative impact on the diesel generator lifespan and would increase maintenance costs and generator replacement frequency, something that was not taken into account for this analysis. Therefore, supplying a remote community's electricity with several smaller diesel generators instead of one large one, although requiring a more extensive initial investment, results in much lower operating costs.

Table 3-10: Cost Breakdown of RFC and Generator Power Systems Over 20 Year Project Lifespan

	RFC Systems		Generator Systems		
	Bloom Box	**Redox Cube**	**GEN1 (1x200 kW)**	**GEN2 (2x100 kW)**	**GEN3 (5x40 kW)**
Capital Cost	$4,774,766	$981,582	$94,347	$116,619	$178,782
Annual Maintenance Cost	$8,523	$8,523	$11,932	$11,932	$11,932
Average Annual Diesel Cost	$353,615	$353,615	$488,205	$465,936	$459,891
Savings from GEN1 after 20 Years	-$6,382,420	$1,310,763	-	$432,042	$448,776
Payback Period from GEN1	-	9 years	-	2 years	4 years
Savings from GEN2 after 20 Years	-$6,814,462	$878,722	-$432,042	-	$16,734
Payback Period from GEN2	-	12 years	-	-	18 years
Savings from GEN3 after 20 Years	-$6,831,196	$861,988	-$448,776	-$16,734	-
Payback Period from GEN3	-	12 years	-	-	-

A graphical representation of this cost breakdown is illustrated in Figure 3-8. The rapid jumps in cost occur because of the need to replace system components whose lifespans are shorter than the project duration. As can be seen in Figure 3-8, the Bloom Box RFC is considerably more expensive than the rest of the setups. The Bloom Box system cost demonstrates that current SOFC technology is not inexpensive enough to allow for the economic replacement of diesel generators located in Canadian remote communities. On the other hand, the Redox Cube illustrates that in the near future reformer and SOFC systems will be able to provide reduced operating costs and a reduced environmental impact with reasonable payback periods.

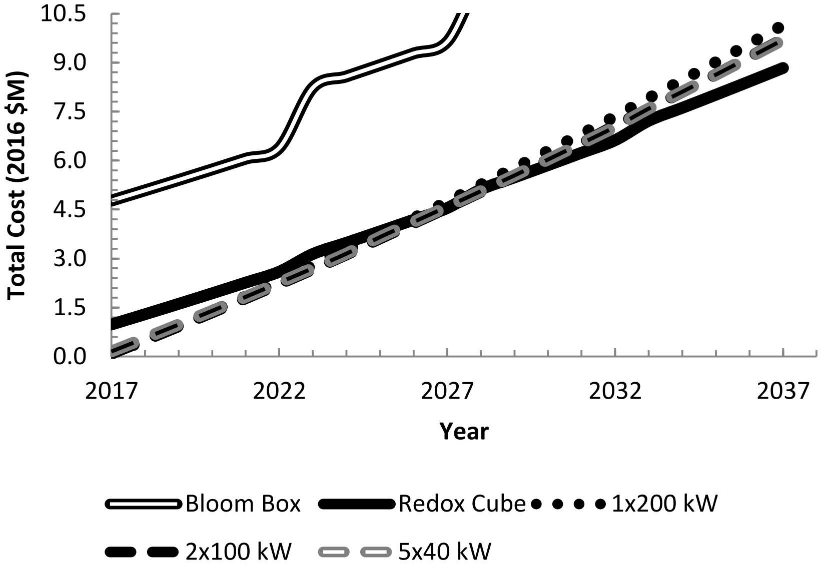

Figure 3-8: Total cost of the various test case remote community electric power systems over the course of the project lifespan.

3.7: Conclusion

In conclusion, remote community living standards and economic growth can be improved by stabilizing electricity prices through a reduction in the reliance of electricity prices on diesel prices. Current attempts to weaken the reliance of remote communities on diesel have resulted in low penetration renewable energy projects coupled with diesel generation. Increased renewable penetration, however, results in reduced diesel generator efficiencies, mitigating the benefits of implementing renewables.

A RFC operating on diesel would allow for improved baseline generation efficiencies without requiring any major overhauls in the fuel distribution network. Moreover, a RFC would have improved performance at lower loads, allowing for the seamless implementation of renewables. SOFCs, however, are an immature technology. The Bloom Box, representing current SOFC technology costs, is not an economically wise investment given the lack of payback period within the 20 year project timeframe. Future SOFC technology, such as the Redox Cube, shows promise with calculated payback periods ranging from 9 years to 12 years depending on the remote community’s diesel generator setup. Replacing diesel generators in Canadian remote communities with Redox Cubes would allow for reduced economic and environmental costs for electricity generation. Over a 20 year cycle, installing Redox Cubes in all fossil fuel-reliant Canadian remote communities would result in potential economic savings of nearly $1 billion and emission reductions of over 3.5 Mt of CO_2 equivalents.

3.8: References

[1] S. H. Salem and A. Bakr, "Naphtha Desulfurization by Adsorption," *Industrial & Engineering Chemistry Research,* vol. 33, pp. 336-340, 1994.

[2] A. Bakr, S. H. Salem and H. S. Hamid, "Removal of Sulfur Compounds from Naphtha Solutions Using Solid Adsorbents," *Chemical Engineering & Technology,* pp. 342-347, 1997.

[3] D. W. Savage, B. K. Kaul, G. D. Dupre, J. T. O'Bara, W. E. Wales and T. C. Ho, "Deep Desulfurization of Distiallate Fuels". United States of America Patent US5454933 A, 3 Oct. 1995.

[4] S. B. Zdonik, E. J. Green and L. P. Haller, "How Cracking Proceeds in the Ethylene-Pyrolysis Reaction," *Oil & Gas Journal,* vol. 65, no. 26, pp. 96-101, 1967.

[5] F. Joensen and J. R. Rostrup-Nielsen, "Conversion of Hydrocarbons and Alcohols for Fuel Cells," *Journal of Power Sources,* vol. 105, pp. 195-201, 2002.

[6] J. R. Rostrup-Nielsen, T. S. Christensen and I. Dybkjaer, "Steam Reforming of Liquid Hydrocarbons," *Studies in Surface Science and Catalysis,* vol. 113, pp. 81-95, 1998.

[7] T. S. Christensen, "Adiabatic Prereforming of Hydrocarbons - An Important Step in Syngas Production," *Applied Catalysis A: General,* vol. 138, pp. 285-309, 1996.

[8] Honeywell, "UniSim Design Simulation Basis," Honeywell, London, Canada, 2005.

[9] I. Kang, J. Bae and G. Bae, "Performance Comparison of Autothermal Reforming for Liquid Hydrocarbons, Gasoline and Diesel for Fuel Cell Applications," *Journal of Power Sources,* vol. 163, pp. 538-546, 2006.

[10] R. D. Parmar, A. Kundu and K. Karan, "Thermodynamic Analysis of Diesel Reforming Process: Mapping of Carbon Formation Boundary and Representative Independent Reactions," *Journal of Power Sources,* vol. 194, pp. 1007-1020, 2009.

[11] P. Costamagna, A. Selimovic, M. Del Borghi and G. Agnew, "Electrochemical Model of the Integrated Planar Solid Oxide Fuel Cell (IP-SOFC)," *Chemical Engineering Journal,* vol. 102, pp. 61-69, 2004.

[12] C. Rayment and S. Sherwin, "Introduction to Fuel Cell Technology," University of Notre Dame, Notre Dame, 2003.

[13] M. C. Williams, "Fuel Cells," in *Fuel Cells: Technologies for Fuel Processing*, Elsevier, 2011, pp. 11-27.

[14] R. H. Perry, D. W. Green and J. O. Maloney, "Appendix B: Physical Properties," in *Perry's Chemical Engineers' Handbook*, The McGraw-Hill Companies, 1999, pp. 641-672.

[15] M. W. Chase, "NIST-JANAF Thermochemical Tables," *Journal of Physical and Chemical Reference Data Monographs,* vol. 9, pp. 1-1951, 1998.

[16] J. D. Routhier and B. A. Peppley, "Study of a 0-D Steady-State Solid Oxide Fuel Cell Process Model using a Municipal Wastewater Biogas and Natural Gas Mix as a Fuel Source," Queen's University, Kingston, Canada, 2012.

[17] H. Dhingra and B. A. Peppley, "Sensitivity Analysis of a 1 kW Diesel-Fuelled SOFC Generators: A Single and Paired-Variable Study," *Journal of Power Sources,* vol. 239, pp. 527-537, 2013.

[18] B. Goodman, N. Bosowski and T. Sanford, "The Bloom Box: An Investigation into the Bloom Box Fuel Cell," Worcester Polytechnic Institute, 2011.

[19] "Fuel Prices," Sept. 2011. [Online]. Available: http://www.mei.gov.on.ca/en/energy/oilandgas/?page=fuelprices.

[20] P. Bouchard, *Management Officer,* Aboriginal Affairs and Development Canada, 2011.

[21] M. Arriaga, C. A. Canizares and M. Kazerani, "Renewable Energy Alternatives for Remote Communities in Northern Ontario, Canada," *IEEE Transactions on Sustainable Energy,* vol. 4, no. 3, pp. 661-670, 2013.

[22] Aboriginal Affairs and Northern Development Canada and Natural Resources Canada, "Status of Remote/Off-Grid Communities in Canada," Government of Canada, 2011.

[23] Northwest Ontario First Nation Transmission Planning Committee, "Draft Technical Report and Business Case for the Connection of Remote First Nation Communities in Northwest Ontario," The Independent Electricity System Operator, 2014.

[24] D. A. Johnson, "Wind-Diesel-Storage Project at Kasabonika Lake First Nation," Wind-Diesel Workshop, Ottawa, 2009.

[25] "Kasabonika Lake Geography," Aboriginal Affairs and Northern Development Canada, 08 2014. [Online]. Available: http://pse5-esd5.ainc-inac.gc.ca/fnp/Main/Search/FNGeography.aspx?BAND_NUMBER=210&lang=eng. [Accessed 04 2016].

[26] U.S. Energy Information Administration, "Fuel Emission Factors," May 2016. [Online]. Available: http://www.eia.gov/tools/faqs/faq.cfm?id=307&t=11.

[27] "Chapter 3: Heavy Trucks," in *2014 Vehicle Technologies Market Report*, Center for Transportation Analysis, 2014, pp. 97-114.

[28] "Aircraft - Basler BT-67," Cargo North, 2012. [Online]. Available: http://www.cargonorth.ca/fleet-basler.html. [Accessed Apr 2016].

[29] "Power and Performance," Basler Turbo Conversions, 2014. [Online]. Available: http://www.baslerturbo.com/power-and-performance.html. [Accessed Apr 2016].

[30] J. Larminie and A. Dicks, Fuel Cell Systems Explained, Chichester, England: John Wiley & Sons Ltd., 2003.

[31] R. O'Hayne, S. Cha, F. B. Prinz and W. Colella, Fuel Cell Fundamentals, Chichester, England: John Wiley & Sons Ltd., 2016.

[32] H. S. Bentsen, Interviewee, *Senior Engineer, Machinery and Systems, DNV GL..* [Interview]. Apr. 2014.

[33] E. D. Tufte and H. Valland, "Impacts of Low Load Operation of Modern Four-Stroke Diesel Engines in Generator Configuration," Norwegian University of Science and Technology, Trondheim, Norway, 2014.

[34] US Environmental Protection Agency, "Greenhouse Gas Equivalencies Calculator," May 2016. [Online]. Available: https://www.epa.gov/energy/greenhouse-gas-equivalencies-calculator. [Accessed Aug. 2016].

[35] Battelle Memorial Institute, "Manufacturing Cost Analysis of 1 kW and 5 kW Solid Oxide Fuel Cell (SOFC) for Auxilliary Power Applications," U.S. Department of Energy, Golden, CO, 2014.

[36] K. Bullis, "An Inexpensive Fuel-Cell Generator," *MIT Technology Review,* 22 Aug. 2013.

[37] Redox Power Systems Inc., "Redox Cube Datasheet," 2015. [Online]. Available: http://www.redoxenergy.com/docs/Redox%20Cube%20Datasheet.pdf. [Accessed Aug. 2016].

[38] Central Maine Diesel, "Perkins Diesel Generator 200 kW," 2016. [Online]. Available: http://www.centralmainediesel.com/order/Perkins-200-kw-diesel-generator.asp?page=9159. [Accessed Apr. 2016].

[39] Central Maine Diesel, "Perkins Diesel Generator 100 kW," 2016. [Online]. Available: http://www.centralmainediesel.com/order/09152.asp?page=9152. [Accessed Apr. 2016].

[40] Central Maine Diesel, "Cummins 40 kW Diesel Generator," 2016. [Online]. Available: http://www.centralmainediesel.com/order/Cummins-40-kW-Diesel-Generator.asp?page=6711. [Accessed 2016 Apr.].

[41] "Cost of Utility Distributed Generators, 1-10 MW: Twenty-Four Case Studies," EPRI, Palo Alto, CA, and Cooperative Research Network, Arlington, VA, 2003.

[42] P. O. Otasowie and P. I. Ezomo, "Life Cycle Cost Analysis of Diesel Generator Set and National Grid in Nigeria," *Journal of Emerging Trends in Engineering and Applied Sciences,* vol. 5, no. 5, pp. 363-367, 2014.

[43] T. M. Mahlia and P. L. Chan, "Life Cycle Cost Analysis of Fuel Cell Based Cogeneration System for Residential Application in Malaysia," *Renewable and Sustainable Energy Reviews,* vol. 15, pp. 416-426, 2011.

[44] H. Tu and U. Stimming, "Advances, Aging Mechanisms and Lifetime in Solid-Oxide Fuel Cells," *Journal of Power Sources,* vol. 127, pp. 284-293, 2004.

[45] A. L. Wagner, R. S. Osborne and J. P. Wagner, "Prediction of Deactivation Rates and Mechanisms of Reforming Catalysts," *Papers of the American Chemical Society,* vol. 48, no. 2, pp. 749-780, 2003.

Chapter 4: Reformer Fluent Model

4.1: Introduction

The UniSim® model presented in Chapter 3: Reformer and Fuel Cell System UniSim® Model utilized a zero-dimensional model of a steam reformer. The reformer was set as isothermal and was assumed to fully convert the hexadecane fuel. Furthermore, the product syngas was assumed to be at equilibrium and there was no pressure drop through the reformer. When determining the risk of carbon formation the UniSim® model neglected axial and radial temperature and gas composition variance within the reformer. ANSYS Fluent was used to more accurately model the performance of the RFC steam reformer, more specifically the performance of the steam reformer when the RFC is operating at 200 kW. ANSYS Fluent is a computational fluid dynamic software tool that provides physical modeling capabilities.

4.1.1: Reformer Selection

A microchannel reactor was chosen for steam reforming. A microchannel reactor was chosen because the small channel sizes and consequent higher surface area to volume ratios help reduce heat and mass transfer limitations [1, 2]. The reduction of heat transfer limitations provided by microchannel reactors is integral for steam reforming to avoid cold spot formation and catalyst deactivation. A microchannel reactor is composed of a number of rectangular channels with hydraulic diameters in the micrometre to millimetre range. The walls of a microchannel reactor are coated with a thin layer of porous catalyst. The advantage to using a microchannel reactor compared to a fixed-bed reactor was the proximity of reforming reactions to the channel walls, helping to dissipate thermal gradients and reducing the risk of catalyst deactivation. Moreover, the presence of a freestream region down the centre of each microchannel results in a lower pressure drop than the pressure drop in fixed-bed reactors. A microchannel reactor was chosen over a monolithic reactor because of the smaller channel sizes which further enhanced heat and mass transfer within the reactor, albeit at the expense of slightly higher pressure drops.

The proposed microchannel RFC uses the flue gas from the fuel cell stack tail gas burner to provide the requisite thermal energy for steam reforming. The flue gas can be coupled with the microchannel reactor by alternating reforming microchannels with flue gas microchannels in a catalytic plate reactor. Figure 4-9 illustrates the front view of the proposed catalytic plate reactor setup.

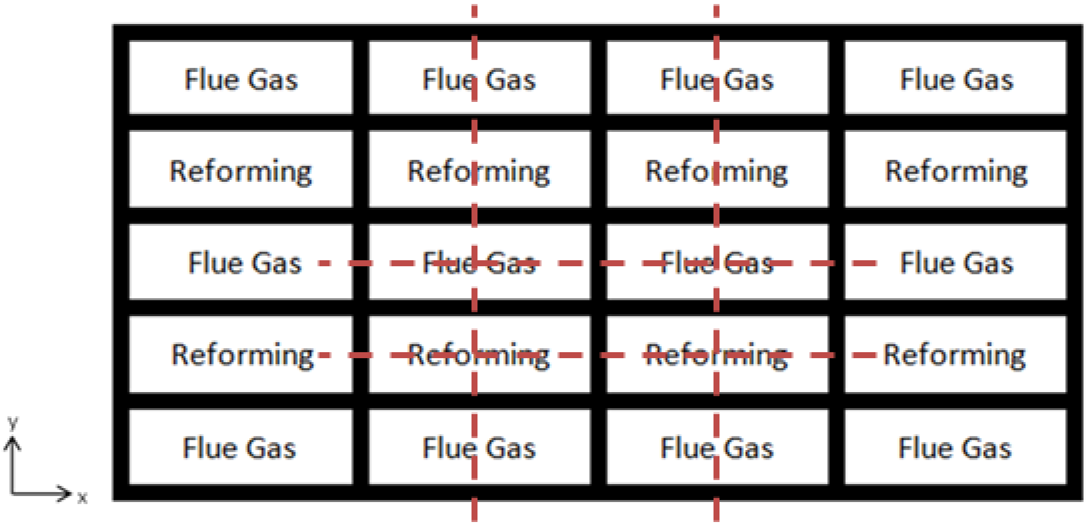

Figure 4-9: Catalytic plate reactor setup. The dotted red lines indicate planes of symmetry as explained in Chapter 4.1.2: Assumptions of Symmetry.

4.1.2: Assumptions of Symmetry

From Figure 4-9 two assumptions of symmetry can be made. Assuming an infinite number of channels in the reactor y-direction would result in the perpetual repetition of a unit consisting of a reforming half-channel followed by a flue gas half-channel. The net heat flux at the y-axis boundaries of these units would be zero as shown in Figure 4-10. A similar assumption can be made in the x-direction so that the repeating unit now consists of a reforming quarter-channel and a flue gas quarter-channel bounded on one side by a vertical wall with a vertical plane of symmetry down the middle (Figure 4-11).

Therefore, the region to be modeled in three-dimensions consists of two quarter-channels separated by a horizontal wall and bounded on one side by a vertical wall, with only half of the vertical wall thickness needing to be modeled.

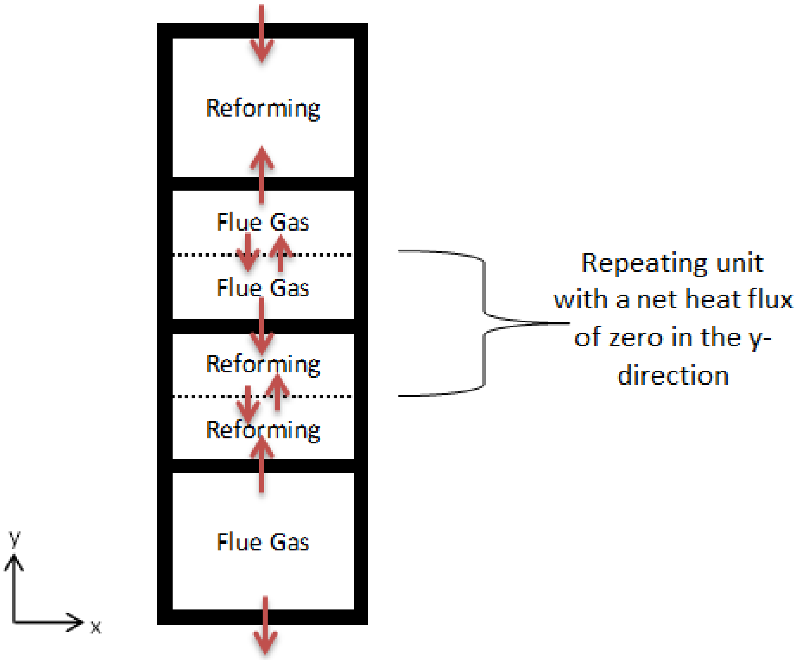

Figure 4-10: Basis for the use of a repeating unit consisting of a reforming half-channel and a flue gas half-channel with red arrows representing heat flux and dotted lines delineating the y-axis boundaries of one unit.

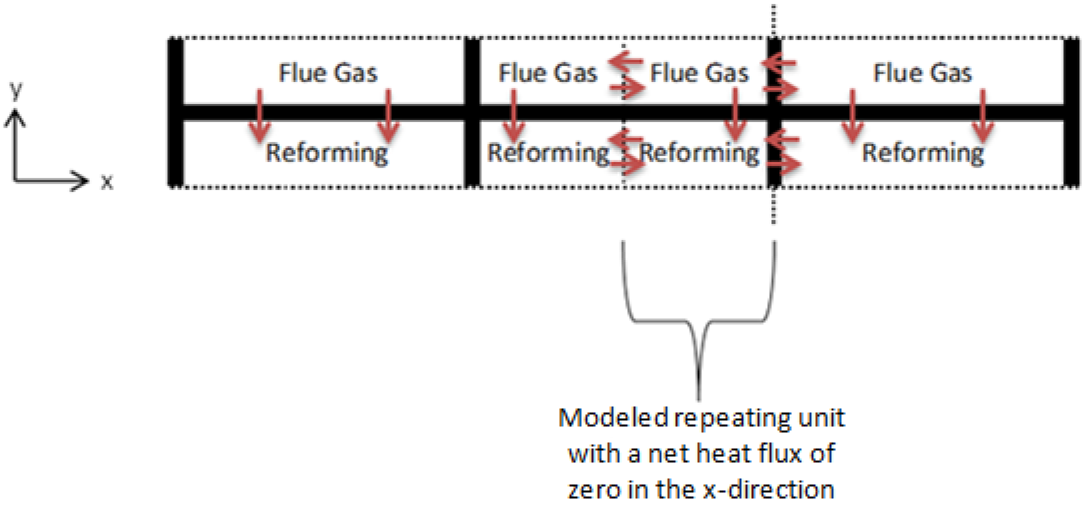

Figure 4-11: Basis for the use of a repeating unit consisting of a reforming quarter-channel and a flue gas quarter-channel with red arrows representing heat flux and dotted lines marking the planes of symmetry. This repeating unit was used to create the three-dimensional model in ANSYS Fluent.

4.1.3: Fluid Flow Parameters

4.1.3.1: Fluid Flow Direction and Flow Regime

Within the microchannel catalytic plate reactor the flow directions of the flue gas and process gases were co-current and the flow regime was laminar. Co-current flow was used because it has a small axial thermal gradient compared to other flow patterns [3]. Laminar flow was used despite turbulent flow resulting in better mixing and faster reaction rates. Laminar flow was used because the high fluid velocities necessary for turbulent flow result in lower residence times that require longer and more expensive reactors to compensate and achieve the desired conversion [4]. The use of laminar flow, however, reduces convective mixing, resulting in greater reliance on diffusion for radial mass transport. Furthermore, laminar flow causes a wider range of residence times within the reforming channel, resulting in reduced hydrogen selectivity [5].

4.1.3.2: Effect of Channel Geometry and Fluid Flow Parameters on Reformer Performance

The performance of a catalytic plate reactor is dependent on the inlet fluid properties and the reactor geometric configuration. Fluid compositions, temperatures, and pressures, as well as channel height, wall thickness, catalyst layer thickness, catalyst layer porosity, wall and catalyst material, channel aspect ratio, and reactor residence time all have an impact on the catalytic plate reactor performance. Previous studies by Karakaya and Avci's and Caglar *et al.*'s have found that thicker walls resulted in improved axial heat transfer. The reformer walls presented the least resistance to heat transfer and a larger wall cross-section allowed for more axial heat transport. Thicker walls resulted in higher conversion over the reactor length, but the higher radial thermal resistance of the thicker walls resulted in more pronounced cold spot formation near the reactor inlet [6, 7]. Zanfir and Gavriilidis' work has shown that larger catalyst layer thicknesses result in lower conversion per unit of catalyst because less of the catalyst is utilized. Zanfir and Gavriilidis also illustrated that lower fluid velocities (higher reactor residence times) result in an upstream movement of the reaction rate profile [8].

4.1.4: Model Dimension Selection

A two-dimensional or three-dimensional model is the preferred choice for modeling microchannel reactors since the transport equations change significantly in the radial direction going from the freestream transport equations to the catalyst layer transport equations. One-dimensional models do not account for variance in the radial direction, making them only effective when modeling fixed-bed reactors where the entire reactor channel is porous material. Overall, one-dimensional and two-dimensional models can be effective for modeling channels with circular cross-section, whereas three-dimensional models are necessary for modeling channels with rectangular cross-sections so that corner flow effects can be accounted for [9, 10].

Karakaya and Avci, however, argue that two-dimensional models can accurately model channels with rectangular cross-sections. Karakaya and Avci’s argument is that lateral heat flow along the x-direction in a given channel is nullified by equivalent heat flow originating from adjacent channels, resulting in x-direction temperature gradients being negligible compared to y-direction temperature gradients [6]. Karakaya and Avci’s approach, however, does not account for the heat transfer from the flue gas channel to the reforming channel along the vertical walls, instead only accounting for heat transfer through the horizontal wall.

Caglar *et al.* used a different approach than Karakaya and Avci to validate the use of a two-dimensional model. Caglar *et al.* assumed a very small channel aspect ratio (height to width ratio), thus making the vertical wall sections negligible compared to the horizontal wall sections, allowing for the use of a two-dimensional model that neglects the impact of the vertical wall region [7]. Caglar *et al.*’s decision to use a channel with a small aspect ratio is validated by Aubin *et al.*’s work. Aubin *et al.* found that very small aspect ratios resulted in narrower residence time distributions within the reforming channel, which in turn led to improved selectivity of the desired product [5].

Moreover, Mladenov *et al.* found that two-dimensional and three-dimensional models tend to have similar species profiles regardless of channel aspect ratio, thus suggesting that channels with rectangular cross-sections can be modeled with relative accuracy by two-dimensional representations of circular cross-section channels with equivalent catalyst layer thickness, porosity and activity, as well as equivalent fluid velocity, mass flow rate and cross-sectional area [9]. Mladenov *et al.* corrected for differing catalyst volumes between square and circular cross-sections by changing the number of active sites so that the activity of the catalyst layer in each geometric configuration was equal. In conclusion, the only advantage of three-dimensional modeling appears to be the ability to study the impact of channel aspect ratios on the performance of channels with rectangular cross-sections.

For this work, a three-dimensional model was originally implemented, modeling a flue gas quarter-channel and a reforming quarter-channel as illustrated in Figure 4-11. The objective was to optimize the reformer with respect to channel aspect ratio. The three-dimensional model, however, resulted in excessively long convergence times on the order of weeks and months. The objective of this work was therefore modified, with the impact of catalyst layer thickness and of varying catalyst porosity along the length of the reformer being studied with the use of a two-dimensional reformer model. Simulations were run on an 8 core Intel®Xeon® CPU E5-1620 v2 @ 3.70GHz with 64 GB of RAM.

4.2: Geometric Configuration and Adaptation for Two-Dimensional Model

The three-dimensional base case geometric parameters were based on previous modeling studies that were conducted with catalytic plate reactors. The three-dimensional model was converted into a two-dimensional model, as shown in Figure 4-12, with both sets of geometric parameters summarized in Table 4-1. The reforming channel was placed in the centre of the two-dimensional model to include the impact of radial reforming channel mass transfer from the freestream reforming channel to the catalyst layer. Flue gas channel radial mass transfer had negligible effects on simulation accuracy compared to reforming channel radial mass transfer.

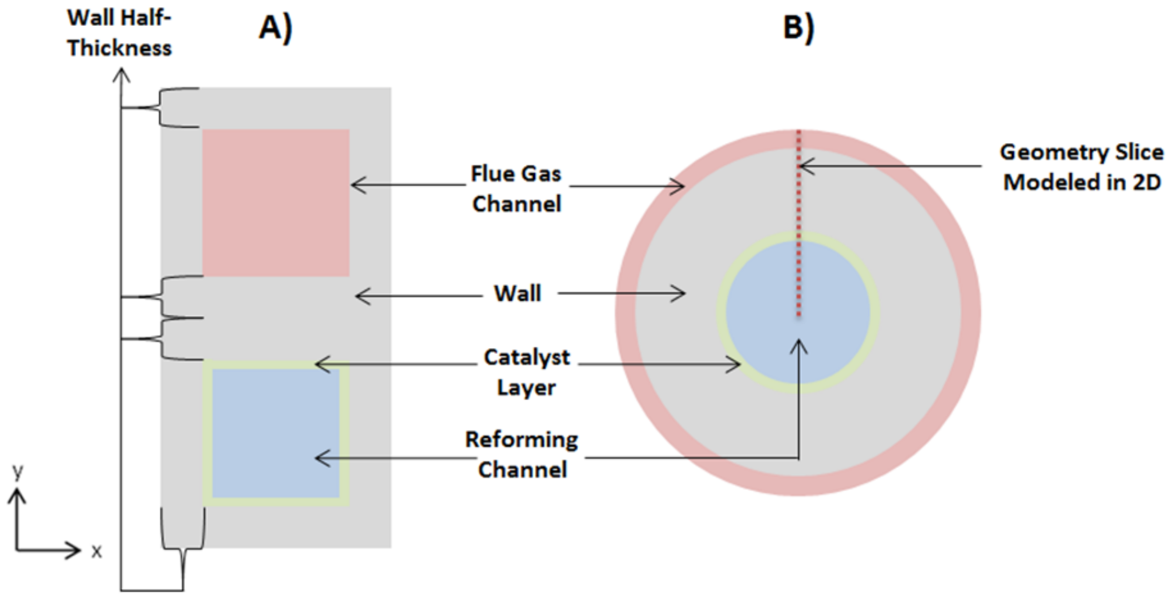

y

Figure 4-12: A) Front view for the geometric configuration for a square channel cross-section unit comprised of a flue gas channel and a reforming channel. The unit is assumed to repeat perpetually in both the x-direction and y-direction for a reformer that is indefinite in the x-direction and y-direction. B) Front view for the equivalent circular cross-section geometric configuration with equal component cross-sectional areas and equal catalyst thickness. Based on the method of Mladenov *et al.* [9].

Table 4-1: Geometric Parameters for the Three-Dimensional Model and the Equivalent Two-Dimensional Model

Square Cross-Section Geometric Parameters	Flue Gas Channel Side Length	0.450 mm
	Wall Thickness Between Channels	0.255 mm
	Catalyst Layer Thickness	0.030 mm
	Catalyst Layer Cross-Sectional Area	0.050 mm^2
	Reforming Channel Side Length	0.390 mm
Cross-Sectional Area Constants	Flue Gas Channel	0.202 mm^2
	Reforming Channel	0.152 mm^2
	Wall	0.589 mm^2
Circular Cross-Section Geometric Parameters	Flue Gas Channel Thickness	0.061 mm
	Wall Thickness	0.250 mm
	Catalyst Layer Thickness	0.030 mm
	Catalyst Layer Cross-Sectional Area	0.044 mm^2
	Reforming Channel Radius	0.220 mm

The equivalent two-dimensional model had the same flue gas channel and reforming channel cross-sectional areas to ensure equivalent mass flow rates and velocities. In addition, the two-dimensional model wall cross-sectional area between the flue gas channel and the reforming channel was made equal to the wall cross-sectional area attributed to a given flue gas channel-reforming channel pair. On the other hand, the three-dimensional geometry had 1.1376 times the catalyst cross-sectional area of the representative two-dimensional geometry being used in the simulations; therefore, an equivalency factor was included in the steam reforming kinetics so that the two-dimensional model had the same catalyst activity as the three-dimensional geometry. The catalytic plate reactor two-dimensional geometry was created using ANSYS DesignModeler (Figure 4-13).

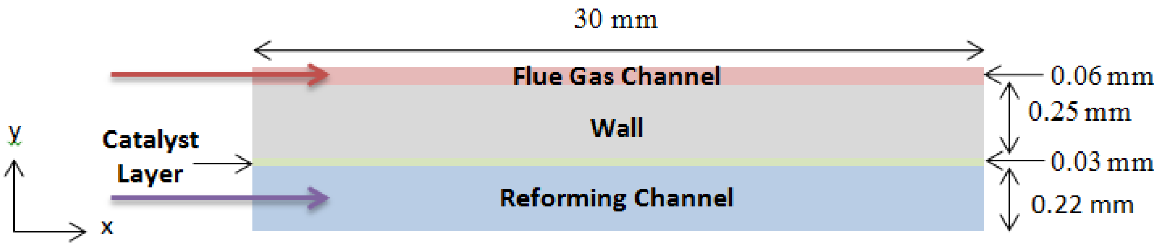

Figure 4-13: ANSYS DesignModeler geometry setup with labeled fluid flow directions.

4.2.1: Catalyst Layer Modeling

The catalyst layer can either be modeled as infinitely thin or it can be modeled with a finite thickness. Reforming reactions rely heavily on effective heat and mass transport to reaction sites because of fast reaction kinetics, particularly near the reforming channel inlet when reactant concentration is high. Modeling the catalyst layer in accordance with the volumetric reaction method (giving the catalyst layer thickness) allows for the thermal effects of the catalyst layer to be properly represented. Furthermore, reforming reactions are diffusion limited, making it essential to account for diffusion when modeling steam reforming reactions [11]. Mladenov *et al.* determined that diffusion within the catalyst layer has a much larger impact on reaction rates than diffusion from the freestream region to the catalyst layer [9]. Diffusion within the catalyst layer is not accounted for in infinitely thin catalyst layer models. Instead, infinitely thin catalyst layer models use effectiveness factors that vary along the reactor length to approximate the effects of mass transport limitations on reforming reaction rates. Overall, modeling the catalyst layer with a finite thickness is more accurate than using an infinitely thin catalyst layer model. However, modeling the catalyst layer with a finite thickness is much more computationally intensive. As illustrated in Figure 4-13, the reformer catalyst layer was modeled with a finite thickness to achieve more accurate results and to allow for the study of the impact of catalyst layer parameters on reformer performance (conversion per unit length of reforming channel) and catalyst utilization (conversion per unit mass of catalyst).

4.3: Mesh Generation

ANSYS Meshing was used to mesh the catalytic plate reactor geometry. Convergence speeds are fastest for polyhedral meshes and slowest for tetrahedral meshes, with hexahedral meshes providing moderate convergence speeds. On average, polyhedral meshes and hexahedral meshes respectively converge 75% and 55% faster than tetrahedral meshes [12]. A hexahedral mesh was used to model the catalytic plate reactor geometry, with the meshes used in this work as well as their quality information included in Appendix C. A hexahedral mesh was chosen over a faster polyhedral mesh because ANSYS Fluent adaptive meshing was compatible with hexahedral meshes, but not with polyhedral meshes. Adaptive meshing allowed for a more robust and straightforward grid independence study.

4.4: ANSYS Fluent Model Development

4.4.1: General Fluent Setup

A steady state ANSYS Fluent model was created to determine the steam reformer performance within the bounds of the RFC UniSim® model explained in Chapter 3: Reformer and Fuel Cell System UniSim® Model. The pressure-based solver was chosen over the density-based solver because the pressure-based solver was originally developed for low-speed incompressible flows and because it allowed for more accurate modeling of the porous region [13]. The primary difference between the pressure-based solver and the density-based solver is the order with which equations are solved. The pressure-based solver solves for momentum, solves the pressure-based continuity equation, before finally solving the energy equation and any source terms derived from chemical reactions, radiation, and more. The density-based solver simultaneously solves the continuity, momentum, energy, and species equations before solving any additional scalar equations. The model was solved using the absolute velocity formulation because there were no moving reference frames [14]. Gravity was ignored in the model since the implementation of gravity in any direction not along the length of the reformer would nullify the previous symmetry assumptions.

4.4.2: Reformer Feed from UniSim®

4.4.2.1: Hexadecane Implementation

As explained in Chapter 3.3.1: System Feed, hexadecane was used as a surrogate for diesel in order to reduce model complexity and accelerate convergence. Using hexadecane as a surrogate fuel meant that the species count was reduced to one species from the 25 species diesel composition presented by Dhingra and Peppley [15]. The result was the reduction of the number of reforming reactions that needed to be implemented. Originally, the hexadecane reforming kinetics presented by Shi *et al.* were used [16]. Shi *et al.*'s kinetics, however, resulted in steam reforming reactions that, depending on which reaction was occurring, consumed 16 or 32 moles of steam and produced 49 or 65 moles of product for every mole of hexadecane reacted (Equation 4-1 and Equation 4-2).

$$\mathrm{C_{16}H_{34} + 16H_2O \rightleftarrows 16CO + 33H_2} \tag{4-1}$$

$$\mathrm{C_{16}H_{34} + 32H_2O \rightleftarrows 16CO_2 + 49H_2} \tag{4-2}$$

The large number of moles involved in Shi *et al.*'s reforming reactions caused large density swings within the mesh cells that acted as a destabilizing force in the model. The destabilization was exacerbated by the reactions occurring in the catalyst layer. Negligible convective transport fluxes in the catalyst layer meant that the large density gradients created by the reforming reactions could not be easily resolved. Finally, the rapid reaction rate of hexadecane steam reforming contributed to the formation of large density gradients faster than they could be resolved. Shi *et al.* created their hexadecane kinetics for a monolithic reactor, but modeled the monolithic reactor as a fixed-bed reactor with a porosity reflecting the combination of the channel freestream space, the catalyst layer, and the channel walls. Therefore, Shi *et al.*'s model had a much higher porosity than is present in a monolithic reactor catalyst layer, resulting in much faster convective and diffusive mass transport that could manage large density gradients.

Shi *et al.*'s modeling approach was not used since it put insufficient value on mass transport limitations within the catalyst layer and it over-estimated heat transport resistance within the channel. Instead of using Shi *et al.*'s modeling approach feed gas-phase reactions were taken into consideration and a feed composed of smaller hydrocarbon chains was used. The gas-phase reactions were based on the evidence that large hydrocarbon chains, such as those found in diesel fuel, typically undergo high temperature gas-phase cracking to form smaller molecules. Therefore, steam reforming of large hydrocarbon feeds generally results in a mixture of propane, propylene, ethane, ethylene, and methane reaching the catalyst layer [17].

4.4.2.2: Gas-Phase Reactions and Implementation of Propylene Kinetics

The diesel and steam mixture fed into the RFC modeled using UniSim® enters the reformer at 693°C. Rostrup-Nielsen *et al.* found that large paraffins undergo gas-phase cracking in the presence of low catalyst activity and at temperatures above 600°C-650°C [18]. The larger hydrocarbons and aromatics present in diesel fuel have slower reforming reaction rates which result in a higher likelihood for them to undergo thermal cracking. Furthermore, before entering the microchannels the feed is first put through a splitter to ensure that all of the microchannels have near equal mass flow rates. The splitter has a low catalyst activity and would promote gas-phase cracking upstream from the microchannels. Parmar's work shows how thermal cracking of higher hydrocarbons results in a product gas comprised primarily of ethylene and propylene [17]. Therefore, propylene was used instead of hexadecane for the reformer model since propylene is a major product of gas-phase reactions. An additional advantage of using propylene is that propylene reforming reactions induce substantially smaller density gradients than hexadecane reforming reactions.

Table 4-2 contains the reformer feed stream table information for the optimized UniSim® RFC with a net power output (after parasitic losses) of 100 kW. Table 4-2 includes the feed stream information for both hexadecane and propylene as the hydrocarbon feed. The propylene feed was created from the hexadecane feed using the reaction in Equation 4-3.

Table 4-2: UniSim® Reformer Feed Stream Table

			Reformer Inlet (Hexadecane)	**Reformer Inlet (Propylene)**	**Flue Gas from Tail Gas Burner**
Flowrate	Mass (kg/h)		108.6	108.6	591.1
	Volumetric (m^3/h)		0.1643	0.1525	1.278
Mole Fractions	H_2O		0.9849	0.9117	0.2869
	Hydrocarbon Fuel	$C_{16}H_{34}$	$1.506 \cdot 10^{-2}$	0	0
		C_3H_6	0	$7.437 \cdot 10^{-2}$	0
	H_2		0	$1.394 \cdot 10^{-2}$	$3.684 \cdot 10^{-5}$
	CO		0	0	$2.389 \cdot 10^{-4}$
	CO_2		0	0	$5.602 \cdot 10^{-2}$
	O_2		0	0	$7.297 \cdot 10^{-2}$
	N_2		0	0	0.5841
Temperature	K		966.05	829.95	1754.15
Pressure	kPa		120	120	120

$$3C_{16}H_{34} \rightarrow 16C_3H_6 + 3H_2 \qquad \Delta H^0 = 484 \text{ kJ/mol} \qquad (4\text{-}3)$$

4.4.3: Fluent Governing Equations

The governing equations for a default Fluent model are limited to flow equations. In order to properly simulate feed conversion to syngas energy and species equations were also included. The energy equation allowed for the inclusion of heat transport effects on reactions rates and the inclusion of heat of reaction effects on the reformer temperature profile. The species equations were necessary so that species diffusion could be used to simulate radial species transport to the catalyst layer from the freestream laminar flow regime. In addition, and more importantly, species equations allowed for the modeling of species transport within the catalyst layer, where convective effects are minimal [19]. Thermal diffusion was also included to account for the Soret effect within the reformer, where the Soret effect accounts for species separation along a temperature gradient. A comparison of thermal diffusion and mass diffusion contributions to the overall diffusion flux of hydrogen in the base case catalyst layer is shown in Appendix E. Initially thermal diffusion and mass diffusion evenly contribute to overall diffusion flux before mass diffusion becomes the dominant contributor approximately 1 mm downstream from the reforming channel inlet. In addition to thermal diffusion, Fluent has an option to enable inlet diffusion. The inlet diffusion option would include diffusive mass transport into and out of the reformer inlets instead of limiting the inlets to convective transport. Inlet diffusion was disabled because the low inlet velocities that were used in the simulation could result in substantial unaccounted for mass gain and/or loss through the inlets if inlet diffusion was included.

Fluent modifies the governing equations within the porous domain to account for the presence of solids. One example of this is the increase in porous domain fluid velocity to ensure equal volumetric flow rates in the porous and freestream domains. In addition, Fluent accounts for porosity effects when calculating diffusion and source terms. For the energy equation Fluent offers the choice between two methods of modeling porous domains. Fluent can either model porous domains as a fluid region with an arbitrary porosity that artificially represents a solid region (equilibrium model), or as a fluid region with solid regions meshed into the domain (non-equilibrium model). Both of the modelling approaches are only different when it comes to modeling heat transfer. The equilibrium model assumes that the temperature of the solid regions and fluid regions are in equilibrium, resulting in the solving of one conservation of energy equation for the domain. The non-equilibrium model separates the solid regions from the fluid regions and solves a conservation of energy equation for each region. The non-equilibrium model is computationally more expensive, albeit more accurate. The non-equilibrium model has the significant drawback of not being compatible with radiation modeling. Including radiation effects was one of the model objectives since a large temperature differential between the flue gas channel and the reforming channel was shown to result in large radiative heat fluxes that played a major role in reducing axial temperature gradients. The porous media parameters provided by Naseri *et al.*'s were only compatible with the equilibrium model and provided a more accurate representation of the porous domain than the non-equilibrium model [20]. Therefore, the equilibrium model was used in conjunction with Naseri *et al.*'s porous media parameters, thus saving computation time and allowing for the inclusion of radiation modeling. The governing equations used in the Fluent model are summarized in Table 4-3 and Table 4-4, with the relevant nomenclature summarized in Table 4-5.

Table 4-3: Fluent Model Governing Equations for Fluid and Solid Domains

Fluid Domain Equations	
Conservation of Mass	$\frac{\partial \rho}{\partial t} + \nabla \cdot (\rho \vec{v}) = 0$
Conservation of Species i	$\frac{\partial}{\partial t}(\rho Y_i) + \nabla \cdot (\rho \vec{v} Y_i) = -\nabla \cdot \vec{J}_i$ $\vec{J}_i = -\rho D_{i,m} \nabla Y_i - D_{T,i} \frac{\nabla T}{T}$
Conservation of Momentum	$\frac{\partial}{\partial t}(\rho \vec{v}) + \nabla \cdot (\rho \vec{v} \vec{v}) = -\nabla P + \nabla \cdot (\bar{\bar{\tau}})$ $\bar{\bar{\tau}} = \mu \left[(\nabla \vec{v} + \nabla \vec{v}^T) - \frac{2}{3} \nabla \cdot \vec{v} B \right]$
Conservation of Energy	$\frac{\partial}{\partial t}(\rho E) + \nabla \cdot \big(\vec{v}(\rho E + P)\big) = \nabla \cdot \left(k \nabla T - \sum_i h_i \vec{J}_i + (\bar{\bar{\tau}} \vec{v}) \right) + S_{h,rad}$ $E = \sum_i Y_i h_i + \frac{v^2}{2}$ $h_i = \int_{298.15\,K}^{T} C_{p,i} dT$
Solid Domain Equations	
Conservation of Energy	$\frac{\partial}{\partial t}(\rho h) = \nabla \cdot (k \nabla T) + S_{h\_rad}$

Table 4-4: Fluent Model Governing Equations for Porous Domain with Velocity Calculated from the Superficial Velocity

Porous Domain Equations	
Conservation of Mass	$\frac{\partial(\gamma\rho)}{\partial t} + \nabla \cdot (\gamma\rho\vec{v}) = 0$ $\vec{v} = \vec{v}_{porous} = \frac{\vec{v}_{superficial}}{\gamma}$
Conservation of Species i	$\frac{\partial}{\partial t}(\gamma\rho Y_i) + \nabla \cdot (\gamma\rho\vec{v}Y_i) = -\nabla \cdot (\gamma\vec{J}_{i,eff}) + \gamma R_i M_{w,i}$
Conservation of Momentum	$\frac{\partial}{\partial t}(\gamma\rho\vec{v}) + \nabla \cdot (\gamma\rho\vec{v}\vec{v}) = -\gamma\nabla P + \nabla \cdot (\gamma\bar{\bar{\tau}}) - \left(\frac{\gamma^2\mu}{\alpha}\vec{v} + \frac{\gamma^3 C_2}{2}\rho\lvert\vec{v}\rvert\vec{v}\right)$
Energy Equation	$\frac{\partial}{\partial t}\left(\gamma\rho_f E_f + (1-\gamma)\rho_s E_s\right) + \nabla \cdot \left(\gamma\vec{v}\left(\rho_f E_f + P\right)\right) = \nabla \cdot \left(k_{eff}\nabla T - \sum_i \gamma h_i \vec{J}_{i,eff} + (\gamma\bar{\bar{\tau}}\vec{v})\right) + \gamma S_{h,rxn} + \gamma S_{h,rad}$ $E = \sum_i Y_i h_i + \frac{v^2}{2}$ $h_i = \int_{298.15\ K}^{T} C_{p,i} dT$ $S_{h,rxn} = -\sum_i h_i^0 R_i$

Table 4-5: Fluent Model Nomenclature

ρ	Density	kg/m^3
t	Time	s
v	Velocity	m/s
Y_i	Mass fraction of species i	-
J_i	Diffusion flux of species i	kg/(m^2·s)
$D_{i,m}$	Mass diffusion coefficient for species i in the mixture	m^2/s
$D_{T,i}$	Thermal (Soret) diffusion coefficient for species i	kg/(m·s)
T	Temperature	K
R_i	Molar rate of creation/destruction of species i	kmol/(m^3·s)
$M_{w,i}$	Molecular weight of species i	kg/kmol
P	Pressure	Pa
$\bar{\bar{\tau}}$	Stress tensor	kg/(m^3·s^2)
μ	Molecular viscosity	kg/(m·s)
B	Unit tensor	-
h_i	Sensible enthalpy of species i	J/kg
$C_{p,i}$	Specific heat	J/(kg·K)
k	Thermal conductivity	W/(m·K)
$S_{h,rxn}$	Energy sources due to reactions	W/m^3
h_i^0	Enthalpy of formation of species i	J/kmol
$S_{h,rad}$	Energy sources due to radiation	W/m^3
γ	Porosity	-
α	Porous media permeability	m^2
C_2	Porous media inertial loss coefficient	1/m
d_p	Mean particle size of porous media	m
d_{pore}	Mean pore size of porous media	m
τ	Tortuosity	-
R	Gas constant	J/(kmol·K)
	Common Subscripts	
eff	Effective value	-
f	Value for fluid region	-
s	Value for solid region	-

4.4.4: Fluid and Solid Material Properties

4.4.4.1: Fluid Materials

Temperature dependent polynomial functions for density, specific heat capacity, thermal conductivity, and viscosity were created for each relevant material from the UniSim® model (see Table 4-2 for a list of relevant materials). The data for the polynomial functions were obtained for the reformer operating pressure of 120 kPa using data from the National Institute of Standards and Technology (NIST) and data compiled using Honeywell's UniSim® Design Suite operating with the PRSV property package [21]. The NIST and UniSim® property data for each material and the fitted polynomial equations can be found in Appendix C. In addition, Lennard-Jones parameters for the different fluid materials were entered into Fluent for species diffusion modeling. The Lennard-Jones parameters for the fluid materials can be found in Appendix C.

4.4.4.2: Fluid Mixture

The fluid materials in the flue gas channel and the reforming channel were combined into a mixture in Fluent. The fluid materials were listed in the mixture in the following order: steam, propylene, hydrogen, carbon monoxide, carbon dioxide, oxygen, nitrogen, and helium. Helium was included in the materials list, despite not being present in the RFC UniSim® model, because the last material listed in Fluent acts to normalize any mass imbalance. The mass fraction of helium would therefore vary to account for computational error and to represent vacuum space within the system. Helium was used instead of another species, such as nitrogen which is already present in the flue gas channel; because helium could have unrealistically altered properties to minimize its impact on the simulation and to more closely represent empty space. The properties of helium were kept at the default Fluent values, except for thermal conductivity which was reduced from 0.152 W/m·K to 1E-10 W/m·K and specific heat which was reduced from 5,193 J/kg·K to 1E-05 J/kg·K. Furthermore, the binary diffusion coefficient for helium was set to 5, about 10,000 times greater than the binary diffusion coefficients for the other species, so that other species would diffuse through helium with much greater ease and helium would diffuse through other species more easily as well.

The fluid mixture was assumed to behave ideally and be incompressible thanks to the low operating pressure (~120 kPa for the base case), high temperature (>550^{o}C) and low velocities (~0.1-1 m/s for the base case) in the reformer that resulted in Mach numbers significantly below the 0.1 threshold above which compressibility effects must be accounted for [13]. The equations used by Fluent to calculate the fluid mixture properties can be found in Appendix C.

4.4.4.3: Solid Materials

Nickel-chromium alloy was used to represent the wall and alumina was used to represent the catalyst layer. Nickel-chromium alloy was chosen because it has a high stress rupture value, allowing for high temperature operation without compromising the reformer walls [22]. In addition, nickel-chromium alloys are resistant to oxidation and high temperature corrosion, the latter being very useful for the processing of contaminant heavy fuels such as diesel [23]. Alumina was chosen because it best represented the catalyst supports in the studies that served as the basis for the model kinetics. The relevant material properties for nickel-chromium alloy (the average properties for Ni/14-46Cr were used) and alumina are summarized in Table 4-6.

Table 4-6: Solid Material Properties

	Nickel-Chromium Alloy [23]	**Alumina [24]**
Density (kg/m^3)	8200	3900
Maximum Service Temperature (K)	1272	1973
Melting Point (K)	1592	2373
Specific Heat (J/kg·K)	440	875
Thermal Conductivity (W/m·K)	12.5	30.5

The radiation parameters for the solid materials were only calculated for nickel-chromium alloy because alumina was only used in the porous layer and Fluent does not account for the solid region of porous media when calculating radiative heat transfer [13]. The radiation parameters at a given wavelength for nickel-chromium alloy were calculated based on a weighted average of nickel and chromium properties for an 80/20 Ni/Cr alloy. The peak radiation wavelength at which the radiation properties were calculated was determined using Wien's displacement law. The peak radiation wavelength was calculated at both the minimum operating temperature of 829.95 K (3.49 μm) and the maximum operating temperature of 1,150 K (2.52 μm). The absorption coefficient and refractive index of nickel-chromium alloy was calculated at both temperatures using data from Rakic *et al.* [25]. The calculated absorption coefficients and refractive indexes were then averaged to yield an absorption coefficient of $4.55 \cdot 10^7$ m^{-1} and a refractive index of 3.85. The errors between the averaged values and the values at each temperature extreme were below 1.8%. Therefore, it was considered unnecessary to increase computation time by making the radiation properties functions of temperature when constant radiation properties exhibited minimal error.

4.4.5: Catalyst Layer Effective Transport Parameters

The catalyst layer was modeled as a porous media with porosity, effective thermal conductivity, and effective mass diffusivity based on X-ray tomography research conducted by Naseri *et al.* on a nickel-alumina spinel reformer catalyst coating [20]. Naseri *et al.* separated the catalyst layer into two domains: the intra-particle domain and the inter-particle domain, where the inter-particle domain assumes that there are no intra-particle pores. Naseri *et al.*'s catalyst domain properties are summarized in Table 4-7.

Table 4-7: Intra-Particle and Inter-Particle Characteristics of a Nickel-Alumina Spinel Reformer Catalyst Coating

	Intra-Particle	**Inter-Particle**
Porosity	0.42	0.14
Mean Pore Size (μm)	0.37	10.82
Effective Diffusivity Factor	0.22	0.30
Effective Thermal Conductivity Factor	0.24	0.76

A limitation of Fluent is an inability to model a catalyst layer in multiple domains. Therefore, the intra-particle and inter-particle catalyst layer domains had to be blended and modeled uniformly. The overall reformer catalyst coating that was modeled had a porosity of 0.5 as calculated from Naseri *et al.*'s work with Equation 4-4.

$$\gamma_{tot} = \gamma_{inter} + (1 - \gamma_{inter})\gamma_{intra} \tag{4-4}$$

The intra-particle domain has a much larger specific surface area upon which reactions can take place than the inter-particle domain. Using the porosities and average pore sizes in Table 4-7, assuming pores are spherical in shape and that there is no pore overlap, the intra-particle specific surface area (surface area divided by volume) was found to be 87 times greater than the inter-particle specific surface area. These findings indicate that the majority of reforming reactions would take place in the intra-particle domain. Therefore, the focus of the catalyst layer model was put on mass transport to and from the intra-particle pores to ensure that proper reaction diffusion limitations were modeled. To reach the intra-particle domain mass and energy must first pass through the inter-particle domain. Therefore, to accomplish a mass transport limited kinetics model the individual momentum, diffusion, and energy transport resistances within the blended domain must be equivalent to the largest resistance from either domain.

4.4.5.1: Mass Transport Limitations

Mass transport limitations that were applied to the catalyst layer included viscous and inertial resistance terms applied to the momentum equation as well as an effective diffusivity factor. These mass transport limitations were assumed to be isotropic. The viscous and inertial resistance source terms were derived from the Ergun equation [26]. To calculate viscous and inertial resistance Fluent required the input of catalyst permeability and the inertial loss coefficient. The momentum resistance terms were based on the inter-particle domain (porosity of 0.14) since momentum losses increased as porosity decreased, resulting in higher momentum losses occurring in the inter-particle domain. The porous media permeability (α) and the porous media inertial loss coefficient (C_2) were calculated using Equation 4-5 and Equation 4-6 respectively. The mean particle diameter in the inter-particle domain determined by Naseri *et al.* was 31 microns, resulting in a permeability of $2.38 \cdot 10^{-14}$ m^2 (viscous resistance of $4.21 \cdot 10^{13}$ m^{-2}) and an inertial loss coefficient of $3.54 \cdot 10^{7}$ m^{-1} [20].

$$\alpha = \frac{d_p^2}{150} \frac{\gamma^3}{(1-\gamma)^2} \tag{4-5}$$

$$C_2 = \frac{3.5}{d_p} \frac{1-\gamma}{\gamma^3} \tag{4-6}$$

The effective diffusivity factor was taken from the intra-particle domain since, based on data from Naseri *et al.*, it presented the highest diffusion resistance [20]. From Naseri *et al.*, the effective diffusivity factor (G_D) is equal to porosity (γ) divided by tortuosity (τ), as shown in Equation 4-7. The effective catalyst layer mass diffusion coefficient was calculated from the effective diffusivity factor using Equation 4-8. Knudsen diffusion (D_{iK}) is included since the Knudsen numbers in the intra-particle domain, as calculated in Appendix C, are all above 0.1, resulting in Knudsen diffusion being no longer negligible [27]. The Knudsen diffusivity of species *i* was calculated using Equation 4-9 from the intra-particle mean pore size of 0.37 μm [28]. The Lennard-Jones characteristic length and characteristic energy (σ_i and ε_i/k_B respectively), given in Appendix C, allow for the calculation of the diffusion collision integral (Ω_D in Equations 4-10 and 4-11) and the calculation of the average characteristic length (σ_{ij} in Equation 4-12) [29, 30]. The diffusion coefficient for species *i* in the mixture before Knudsen modification ($D_{I,m}$) is given by Equation 4-13, with x_i being the mole fraction of species *i* [31]. The binary diffusivity of species *i* in species *j* (D_{ij}) was calculated using Equation 4-14 [32]. Species diffusion was implemented into Fluent in the form of a user-defined function (UDF) included in Appendix D, with catalyst layer diffusion calculated using Equation 4-8 and reforming channel and flue gas channel diffusion calculated using Equation 4-13.

$$G_D = 0.22 = \frac{\gamma}{\tau} \tag{4-7}$$

$$D_{i,m,eff} = G_D D^*_{i,m} = G_D \left(\frac{1}{D_{iK}} + \frac{1}{D_{i,m}}\right)^{-1} \tag{4-8}$$

$$D_{iK} = \frac{d_{pore}}{3}\sqrt{\frac{8RT}{\pi M_{w,i}}} \tag{4-9}$$

$$\Omega_D = \frac{1.06036}{(T^*)^{0.1561}} + \frac{0.193}{\exp(0.47635(T^*))} + \frac{1.03587}{\exp(1.52996(T^*))} + \frac{1.76474}{\exp(3.89411(T^*))} \tag{4-10}$$

$$T^* = \frac{T}{(\epsilon_i \epsilon_j)^{\frac{1}{2}}} \tag{4-11}$$

$$\sigma_{ij} = \frac{\sigma_i + \sigma_j}{2} \tag{4-12}$$

$$D_{i,m} = \frac{(1-x_i)}{\sum_{j\neq i}\frac{x_j}{D_{ij}}} \tag{4-13}$$

$$D_{ij} = \frac{\left[T^3\left(\frac{1}{M_{w,i}} + \frac{1}{M_{w,j}}\right)\right]^{1/2}}{P\sigma_{ij}^2 \Omega_D} \tag{4-14}$$

4.4.5.2: Energy Transport Limitations

The energy transport limitations applied to the catalyst layer were implemented into Fluent as a reduction in catalyst thermal conductivity. The energy transport limitation was assumed to be isotropic. From Naseri *et al.*, the total effective thermal conductivity factor of the catalyst layer was equal to 0.18 [20]. The equation for effective thermal conductivity used in Fluent is Equation 4-15, with k_f being negligible [14]. The result is that, for a porosity of 0.5, Fluent calculates an effective conductivity of $0.5 \cdot k_s$, whereas the actual effective thermal conductivity calculated by Naseri *et al.* is $0.18 \cdot k_s$. Therefore, the thermal conductivity of alumina was multiplied by 0.36 so that Fluent computed the true thermal conductivity of the catalyst layer. The new alumina thermal conductivity inputted into Fluent was 11.07 W/(m·K).

$$k_{eff} = \gamma k_f + (1-\gamma)k_s \cong (1-\gamma)k_s \tag{4-15}$$

4.4.6: Chemical Reaction Kinetics

The chemical reactions inside the catalyst layer were simulated using the volumetric reaction model in Fluent. The combination of Figueiredo and Trimm and Xu and Froment kinetics used by Sadooghi and Rauch were also used in this Fluent model [33]. Figueiredo and Trimm's propylene steam reforming equation (Equation 4-16) and propylene steam reforming kinetics (and Equation 4-17) over alumina-supported nickel catalyst were implemented in the model, with temperature in Kelvin and the partial pressure of propylene in kPa [34].

$$C_3H_6 + 6H_2O \rightleftarrows 3CO_2 + 9H_2 \qquad \Delta H^0 = 110 \text{ kJ/mol} \tag{4-16}$$

$$R_1 = 0.0281 \cdot \frac{P_{C_3H_6}}{1+0.09 \cdot P_{C_3H_6}} \cdot \exp\left(-\frac{8000}{T}\right) \quad \frac{mol}{s \cdot g_{cat}} \tag{4-17}$$

The WGS reaction, the methanation reaction, and the carbon dioxide reforming reaction (dry reforming) were considered for inclusion within the model. The dry reforming reaction was excluded from the model because dry reforming kinetics are slower than steam reforming kinetics. Dry reforming is often considered negligible when steam is present [35, 36]. The methanation reaction (Equation 4-18) was also excluded from the model because it has low methane selectivity at the RFC operating conditions (low pressure and high temperature), with the UniSim® model showing negligible quantities of methane at the reformer outlet assuming syngas equilibrium composition. Furthermore, Liu *et al.* reported negligible amounts of methane at reformer exit temperatures above 700°C and Thormann *et al.* reported negligible amounts of methane at temperatures above 550°C [37, 38, 39]. The WGS reaction (Equation 4-19), however, was included in the model since the reverse reaction produced carbon monoxide. The UniSim® reformer outlet equilibrium composition predicted a significant carbon monoxide concentration, justifying the inclusion of carbon monoxide in the Fluent model.

$$CO + 3H_2 \rightleftarrows CH_4 + H_2O \qquad \Delta H^0 = -206.2 \text{ kJ/mol} \tag{4-18}$$

$$CO + H_2O \rightleftarrows CO_2 + H_2 \qquad \Delta H^0 = -41.2 \text{ kJ/mol} \tag{4-19}$$

The kinetic rate expression (Equation 4-20) for the WGS reaction was implemented from the mathematical model developed by Xu and Froment for nickel catalyst on magnesium aluminate spinel [40].

$$R_2 = \frac{\frac{k_2}{P_{H_2}}\left[P_{CO}P_{H_2O} - \frac{P_{H_2}P_{CO_2}}{K_2}\right]}{DEN^2} \quad \frac{mol}{h \cdot g_{cat}} \tag{4-20}$$

Species partial pressures in Equation 4-20 are in kPa, the *DEN* term is defined in Equation 4-21, and any remaining variables are defined in Table 4-8.

$$DEN = 1 + K_{CO}P_{CO} + K_{H_2}P_{H_2} + \frac{K_{H_2O}P_{H_2O}}{P_{H_2}} \tag{4-21}$$

Table 4-8: Kinetic Parameters for the WGS Reaction [40]

Rate Coefficient	$k_2 = 4.39 \cdot 10^4 \cdot e^{-8074.3/T}$	mol·kPa^{-1}/(h·g$_{cat}$)
Adsorption Coefficient Constants	$K_{H_2O} = 1.77 \cdot 10^3 \cdot e^{-10666.35/T}$	kPa^{-1}
	$K_{H_2} = 6.12 \cdot 10^{-11} \cdot e^{9971.13/T}$	kPa^{-1}
	$K_{CO} = 8.23 \cdot 10^{-7} \cdot e^{8497.71/T}$	kPa^{-1}
Equilibrium Constant	$K_2 = e^{\frac{4400}{T} - 4.063}$	kPa^{2}

The UDF used to create the species reaction rate source terms for the Fluent simulation is included in Appendix D. Within the UDF the reaction rate was converted to Fluent units of kmol/(m^3·s) by multiplying the calculated reaction rate by the density of alumina and by the fraction of solid in the catalyst layer. Alumina was assumed to represent the catalyst density since alumina was the dominant compound in the catalyst used to determine the kinetics. The reaction rate was also multiplied by the equivalency factor of 1.1376 to account for the added catalyst that would be in a square cross-section channel. Finally, the reaction rate was divided by porosity to counteract the governing equations in Fluent which multiply the reaction rate by porosity.

4.4.7: Radiative Heat Transport

Radiative heat transfer was included in the Fluent model because the high temperatures required for the reforming reactions resulted in thermal radiation playing a significant role in heat transport. Overall, the radiation model was used to account for axial radiation along the length of the fluid channels as well as radial radiation exchange between the wall and the fluid channels.

The discrete ordinates radiation model was chosen because, unlike other radiation models available in Fluent, the discrete ordinates model allowed for the accurate simulation of surface-to-fluid and fluid-to-fluid radiative heat transfer for media of any optical thickness. Gray radiation was modeled since discrete ordinates non-gray radiation increases simulation computation times and is intended to be used with semi-transparent solid media, which is not present in this simulation [13].

4.4.7.1: Fluid Domain Radiative Heat Transport

The discrete ordinates model describes radiative transfer for an absorbing, emitting, and scattering medium at position $\vec{r}$ in the direction $\vec{s}$ using Equation 4-22. The first term on the left-hand side represents the difference in radiation beam intensity across a given simulation mesh cell. The second term on the left-hand side represents absorption and scattering heat transfer from the radiation beam to a cell. The first term on the right-hand side represents absorption heat transfer from the cell to the radiation beam. The final term on the right-hand side represents scattering heat transfer from the cell to the radiation beam. Because there are no semi-transparent solid media in the simulation Equation 4-22 only applies to radiation exchange within fluid domains. The variables in Equation 4-22 are defined in Table 4-9.

$$\nabla \cdot (I(\vec{r},\vec{s})\vec{s}) + (a+\sigma_s)I(\vec{r},\vec{s}) = an^2\frac{\sigma T^4}{\pi} + \frac{\sigma_s}{4\pi}\int_0^{4\pi} I(\vec{r},\vec{s})\Phi(\vec{s}\cdot\vec{s}')d\Omega' \qquad (4\text{-}22)$$

Table 4-9: Discrete Ordinates Radiation Model Nomenclature

$\vec{r}$	Position vector
$\vec{s}$	Direction vector
$\vec{s}'$	Scattering direction vector
s	Path length
$I(\vec{r},\vec{s})$	Radiation intensity
a	Absorption coefficient
n	Refractive index
σ_s	Scattering coefficient
σ	Stefan-Boltzmann constant ($5.669\cdot10^{-8}$ W/($m^2\cdot K^4$))
Φ	Phase function
Ω'	Solid angle
ε	Emissivity
$a_{\varepsilon,i}$	Emissivity weighting factor for i^{th} gray gas
κ_i	Absorption coefficient for the i^{th} gray gas
p	Sum of partial pressures for all absorbing gases
$b_{\varepsilon,i,j}$	Emissivity gas temperature polynomial coefficient
ε_w	Wall emissivity
T_w	Wall temperature
q_{in}	Amount of radiative energy incident on the wall

Scattering was set to zero since scattering by molecules is always negligible for the purpose of heat transfer [41]. The refractive indexes of the fluid species were set to unity as their reference values were less than a percentile off of unity [42]. With the above changes Equation 4-22 became Equation 4-23.

$$\nabla\cdot(I(\vec{r},\vec{s})\vec{s}) + aI(\vec{r},\vec{s}) = a\frac{\sigma T^4}{\pi} \qquad (4\text{-}23)$$

Originally the fluid radiation parameters were estimated using Hottel and Sarofim's charts for radiation properties of combustion gases [43, 44]. A UDF (see Appendix D) was created based on the Hottel and Sarofim charts using the equations presented in *Radiative Heat Transfer* by Modest [41]. The UDF, however, contained numerous equations that resulted in a slower convergence and negligible improvements in accuracy compared to using the weighted-sum-of-gray-gases model (WSGGM) method already present in Fluent. Therefore, WSGGM was used to estimate the emissivity and absorption coefficients for the fluid domains.

The total emissivity of a fluid over the distance *s* is calculated from Equation 4-24. The temperature dependence of the emissivity weighting factors is expressed by Equation 4-25. The emissivity gas temperature polynomial coefficients and the absorption coefficients are estimated by Fluent by fitting Equation 4-24 to a table of stored emissivities obtained from Coppalle and Vervisch's work on total emissivities of CO_2-H_2O mixtures, Denison and Webb's work on generating WSGGMs ,and Smith *et al.*'s work on the evaluation of coefficients for the WSGGM [45, 46, 47]. The table of stored emissivities are for different relative pressures of CO_2 and H_2O, assuming a total pressure of 1 atm. When the pressure does not equate to 1 atm Fluent uses scaling rules from Edwards Matavosian's work on scaling rules for gas absorptivity and emissivity presented in Equation 4-26, where *m* is a non-dimensional value from Edwards and Matavosian's work and is a function of absorbing gas partial pressures and temperature [48]. The WSGGM absorption coefficient is calculated from Equation 4-27. The WSGGM path length is calculated from Equation 4-28 presented by Siegel and Howell [49].

$$\varepsilon = \sum_{i=0}^{I} a_{\varepsilon,i} T\left(1 - e^{-\kappa_i p s}\right) \tag{4-24}$$

$$a_{\varepsilon,i} = \sum_{j=1}^{J} b_{\varepsilon,i,j} T^{j-1} \tag{4-25}$$

$$\kappa_i \to \kappa_i p_{tot}^{m} \tag{4-26}$$

$$a = -\frac{\ln(1-\varepsilon)}{s} \tag{4-27}$$

$$s = 3.6\frac{V}{A} \tag{4-28}$$

The negligible propylene partial pressure in the reforming stream as well as the general dominance of steam and carbon dioxide concentrations over concentrations of other absorbing species in the simulation (primarily carbon monoxide) meant that the WSGGM model presented an adequate estimation of reforming channel and flue gas channel radiation properties.

4.4.7.2: Catalyst Layer Radiative Heat Transport

For the purpose of implementing radiation in the catalyst layer Fluent scales the radiative heat flux and radiative heat source by the porosity, but still only considers the fluid domain for radiative heat transport and assumes open pathways through the porous region. Moreover, Fluent warns that the way radiation is modeled makes the interaction of radiation and porous media strictly valid for porosities very close or equal to unity [13]. Therefore, to avoid over-estimated heat transfer in the catalyst layer Equation 4-23 was applied to the reforming channel and flue gas channel, but not to the catalyst layer. A UDF (see Appendix D) was applied to the catalyst layer to set the absorption coefficient to zero. The assumption of a catalyst layer absorption coefficient of zero was validated by the short radiation path lengths that would be present in a catalyst layer with an inter-particle porosity of 0.14. These short radiation path lengths would result in thermal conduction and thermal convection being the dominant pathways for heat transport through the catalyst layer. Furthermore, the thermal equilibrium model that models heat transport in the porous domain forces the fluid and solid temperatures within a given cell to be equal, thus eliminating the need to model any short path length radiative heat transport between solid and fluid regions.

4.4.7.3: Solid Interactions of Radiative Heat Transport

The interaction of radiation with the opaque walls in the simulation is different from the manner in which radiation interacts with the fluid cells. The incident radiative heat flux on the wall is calculated using Equation 4-29. Radiative heat transfer to opaque walls takes the form of absorbed radiation (Equation 4-30). Radiative heat transfer from the opaque walls takes the form of reflected radiation (Equation 4-31) and emitted radiation (Equation 4-32). The radiation intensity leaving the wall is described by Equation 4-33. The radiation reflected by the walls was assumed to be entirely diffuse since even for a perfectly smooth material, which would not be the case for a reformer heat exchange wall during operation, scattering centers beneath the materials surface often cause diffuse radiation reflection [50]. The wall emissivity, by Kirchhoff's law, is equal to the wall absorptivity as long as the wall temperature and gas temperature do not differ excessively [51]. For the purpose of the simulation Kirchhoff's law was deemed to hold.

$$q_{in} = \int_{\vec{s}\cdot\vec{n}>0} I_{in}\vec{s}\cdot\vec{n}\,d\Omega \tag{4-29}$$

$$absorption\ at\ the\ wall\ surface = \epsilon_w q_{in} \tag{4-30}$$

$$reflected\ radiation = (1-\varepsilon_w)q_{in} \tag{4-31}$$

$$emission\ from\ the\ wall\ surface = n^2\epsilon_w\sigma T_w^4 \tag{4-32}$$

$$I_o = \frac{q_{out}}{\pi} = \frac{reflected\ radiation + emissions\ from\ the\ wall\ surface}{\pi} \tag{4-33}$$

4.4.8: Fluent Boundary Conditions

4.4.8.1: Reforming Channel and Flue Gas Channel inlets

The velocity inlet boundary condition was chosen for the reforming channel inlet and for the flue gas channel inlet. Inlet radiation from any upstream body was neglected. The inputs for the reforming channel and flue gas channel velocity inlets are summarized in Table 4-10. For the base case Fluent simulation a reforming channel feed velocity of 0.1 m/s was used. The equivalent flue gas channel feed velocity that resulted in an equal number of reforming channels and flue gas channels was 0.6294 m/s.

4.4.8.1.2: Inlet Temperature Adjustments from UniSim®

The tail gas burner exhaust, as mentioned in Chapter 4.4.2: Reformer Feed from UniSim®, is initially at 1754.15 K, which is above the maximum service temperature for nickel-chromium alloy (Table 4-6). Furthermore, to avoid catalyst activity loss, the alumina support sintering temperature must be considered when determining the maximum allowable temperature in the reformer. The Tamman temperature is generally assumed to be the temperature limit above which sintering becomes a significant risk [52]. The Tamman temperature can be estimated as half of the material melting temperature [53]. Therefore, the Tamman temperature for alumina would be 1,187 K, making 1,187 K the maximum allowable temperature in the Fluent reformer model. The tail gas burner exhaust temperature was therefore reduced to 1,150 K by first using the stream to partially heat the air feed before it was allowed to enter the flue gas channels.

Table 4-10: Reforming Channel and Flue Gas Channel Fluent Velocity Inlet Inputs

		Reforming Channel Inlet	Flue Gas Channel Inlet
Inlet Velocity	m/s	0.1	0.6294
Reynolds Number	Circular Cross-Section	0.31	0.24
	Square Cross-Section	0.28	1.83
Mole Fractions	H_2O	0.9117	0.2869
	C_3H_6	$7.437 \cdot 10^{-2}$	0
	H_2	$1.394 \cdot 10^{-2}$	$3.684 \cdot 10^{-5}$
	CO	0	$2.389 \cdot 10^{-4}$
	CO_2	0	$5.602 \cdot 10^{-2}$
	O_2	0	$7.297 \cdot 10^{-2}$
	N_2	0	0.5841
Temperature	K	829.95	1,150.00
Pressure	kPa	120	120

4.4.8.2: Reforming Channel and Flue Gas Channel Outlets

The pressure outlet boundary condition was used for both the reforming channel and flue gas channel outlets. The outlet gauge pressure was set to 0 Pa (the Fluent model operating pressure was already set to 120 kPa). The average pressure specification was used to allow the pressure to vary across the outlet boundary while maintaining an overall pressure of 120 kPa. The outlet boundary pressure was determined by Equation 4-34, where P_e is the specified outlet pressure, P_c is the interior cell pressure at the neighbouring exit face, $P_{c,avg}$ is the averaged interior cell pressure at a boundary, and F is a blending factor with a range of 0-1 [14]. Inlet radiation from any downstream body was neglected.

$$P_f = P_e + (1 - F)\left(P_c - P_{c,avg}\right) \tag{4-34}$$

4.4.8.3: Wall and Catalyst Layer Ends

The wall and catalyst layer ends used the wall boundary condition and were assumed to be adiabatic. The catalyst layer ends were treated as infinitely thin slip walls. Slip walls were used since the slip regime was dominant in both the inter-particle and intra-particle domains of the catalyst (see Appendix C for details on determining slip flow).

4.4.8.4: Wall and Channel Boundaries

The wall-flue gas channel and wall-catalyst layer boundaries were modeled as coupled walls to allow for heat transfer through the boundary. The wall-flue gas channel boundary was modelled as a no-slip wall with radiative heat transfer described by the properties of nickel-chromium alloy. An 80/20 nickel-chromium alloy has an emissivity of around 0.88 for a temperature between 600^oC and 1,300^oC [54]. The wall-flue gas channel boundary radiation reflection was given a diffuse fraction of unity to represent the effect of scattering centers beneath the surface on incoming radiation [50]. The wall-catalyst layer boundary was modelled as a slip boundary with no radiation emission and a diffuse fraction of unity for reflected radiation to represent the rough surface of a catalyst layer. As explained in Chapter 4.4.8.3: Wall and Catalyst Layer Ends, the slip wall assumption is acceptable given the catalyst layer Knudsen numbers. In turn, as explained in Chapter 4.4.7.2: Catalyst Layer Radiative Heat Transport, radiation can be ignored because it is not the driving force for heat transfer in the catalyst layer.

4.4.8.5: Symmetry Boundaries

A symmetry boundary condition does not allow any heat flux, mass flux, or radiative heat transfer through the boundary. The symmetry boundary condition was used for the bottom of the reforming channel and for the top of the flue gas channel. The bottom of the reforming channel, as seen in part B of Figure 4-12, is set at the centre of the reforming channel with a horizontal line of symmetry at the bottom. The top of the flue gas channel, although technically being a wall in part B of Figure 4-12 above, acts to represent the horizontal channel centreline of the square cross-section channel as illustrated in Figure 4-10 above. Therefore, the top of the flue gas channel was treated as a plane of symmetry as it would have been in the modeling of a square cross-section channel. See Chapter 4.1.2: Assumptions of Symmetry for details on how symmetry boundaries were established.

4.5: Fluent Solution Method

4.5.1: Spatial Discretization

In order to solve the simulation ANSYS Fluent converts scalar transport equations to algebraic equations that can be solved numerically. Parameter values are stored at the centre of each mesh cell and cell face parameter values are interpolated from the cell centre. The least squares cell-based gradient averaging scheme was used in the simulation because it was cheaper than the alternatives and still provided equivalent simulation accuracy. The PRESTO! Pressure discretization scheme was used since it is recommended for flows involving porous media [14]. The rest of the discretization schemes were set to second order upwind in order to ensure simulation accuracy by using Taylor series expansions from the parameter values at the cell centre, as compared to first order upwind which sets all cell face values equal to cell centre values.

4.5.2: Improving Stability in Stiff Reacting Flows

Rapid reaction rates, large heats of reaction, and high mass transport resistances in the catalyst layer resulted in a relatively unstable simulation. Chapter 4.4.2: Reformer Feed from UniSim® covered how the Fluent model was changed to improve simulation stability given the minimal mass transport effects that were available to resolve the large density gradients created during steam reforming. In addition, initially the model completely discounted convective mass transport in the catalyst layer since convection was believed to be negligible due to high convective resistances. Stability difficulties forced the re-implementation of convective mass transport in the catalyst layer. The re-implementation of convection transport improved simulation stability and thus illustrated that convective resistances, at least in the inter-particle domain, did not render convective transport negligible.

The destabilizing effect of rapid reaction rates was partially mended by using the Fluent stiff chemistry solver to solve for the species reaction rates. The stiff chemistry solver was employed to improve solution stability. Steam reforming reactions are often diffusion limited with the large magnitude of the reaction source term for steam reforming resulting in reaction time scales that are much faster than convection and diffusion time scales. The stiff chemistry solver implements a time step (τ) when solving species reaction rates. The implemented time step is equal to around one-tenth of the minimum convective or diffusive time-scale in the cell (Equation 4-35). The time step forcefully reduces the reaction source term to a value manageable with the given mass transport time scales, increasing simulation stability.

$$R_i^* = \frac{1}{\tau}\int_0^\tau R_i dt \tag{4-35}$$

Further advances in stabilizing the large species and energy source terms associated with the steam reforming reactions were achieved by using the coupled pressure-velocity scheme. The coupled scheme solves the momentum and pressure-based continuity equations simultaneously, resulting in improved stability and efficiency when solving steady state simulations [13]. The large heat sinks and molar concentration changes created by the steam reforming reaction resulted in large density shifts and a simulation that had heavy coupling between the momentum and mass balances and the species transport equations. The coupled scheme allowed for improved stability for simulations with large density fluctuations. Furthermore, the coupled scheme also allowed for the use of the pseudo-transient solver, which helped speed convergence.

The pseudo-transient solver improved convergence speed by allowing for the specification of separate times steps for the solid domain and the fluid domains. One of the factors that was slowing convergence was the low time step applied universally to all domains. Energy convergence in the solid domain in particular acted to significantly slow overall convergence speeds. Moreover, the solid domain was not overly affected by the instabilities caused by the reactions in the fluid domains. Therefore, the solid domain did not require as small a time step as what was needed to maintain stability in the fluid domains. The pseudo-transient method allowed for the solid domain to have a larger time step, thus speeding convergence.

4.5.3: Solution Initialization

To reduce convergence time the solution was initialized with parameter values resembling the hypothesized simulation results. Solution initialization was conducted using a patching approach to achieve different compositions and velocities in the different channels. The flue gas channel was patched with the flue gas channel inlet composition from UniSim® and velocity (as shown in Table 4-10) since they were assumed to remain relatively unchanged through the flue gas channel. The catalyst layer and reforming channel were patched with the UniSim® reformer outlet composition for the relevant materials (see Appendix A). The catalyst layer velocity was patched to 0 m/s to reflect the high momentum resistance in the catalyst layer. The reforming channel velocity was patched to the inlet value of 0.1 m/s. The entire system had temperature patched to the average inlet temperature (990 K) and gauge pressure patched to 0 kPa (the operating pressure was already set to 120 kPa). Only the base case model was initialized using the above approach, with subsequent simulations being initialized from previous model results.

4.5.4: Determining Convergence

During simulation computation solution convergence was determined by monitoring equation residuals, outlet mass flow rates, outlet energy flow rates, as well as species fractions at different points along the reformer length. The species fractions that were monitored were each species' reforming channel outlet mole fraction, as well as the maximum mole fraction of helium in the catalyst layer, the catalyst layer mole fraction of helium at a third of the reformer length, and the catalyst layer mole fraction of helium at two thirds of the reformer length. The outlet monitors were useful in determining whether the reformer products were unchanging. The outlet monitors, however, due to the length of the reformer were inadequate at conveying solution changes that may be occurring upstream and had yet to impact outlet composition. Monitoring helium, the species used by Fluent to rectify mass imbalances which occur particularly during chemical reactions, in the catalyst layer along the entire length of the reformer allowed for convergence to be determined once the outlet monitors became constant.

4.5.5: Solution Refinement

4.5.5.1: Minimizing Chemical Reaction Error

The converged solution had to be checked for independence from the in situ adaptive tabulation (ISAT) error tolerance. The ISAT integration method was used in conjunction with the stiff chemistry solver. ISAT creates a chemistry table updated after every chemistry iteration. The default Fluent ISAT error tolerance is 10^{-3}. Although the default error tolerance is accurate for major species, it does not adequately capture minor species. The default value was used for the initial simulation. After convergence the ISAT error tolerance was reduced in stages until the reforming channel outlet concentration of hydrogen and carbon monoxide became relatively unchanged (a change of less than 2%). Moreover, higher error tolerances resulted in longer computation times.

Three ISAT error tolerances were tested before solution independence was achieved: 10^{-3}, 10^{-5}, and 10^{-7}. The percent change for the hydrogen species at the reforming channel outlet was 0.22% from ISAT error tolerances of 10^{-3} to 10^{-5} and 0% from 10^{-5} to 10^{-7} (Figure 4-14). Moreover, carbon monoxide had a reforming channel outlet concentration change of 6.86% from ISAT error tolerances of 10^{-3} to 10^{-5} and 0.23% from 10^{-5} to 10^{-7} (Figure 4-14). As expected, ISAT error reduction had a larger effect on species with low concentrations, such as carbon monoxide. Overall, an ISAT error tolerance of 10^{-5} was used during subsequent simulations since further reducing the ISAT error tolerance resulted in negligible changes in reforming channel outlet species concentrations.

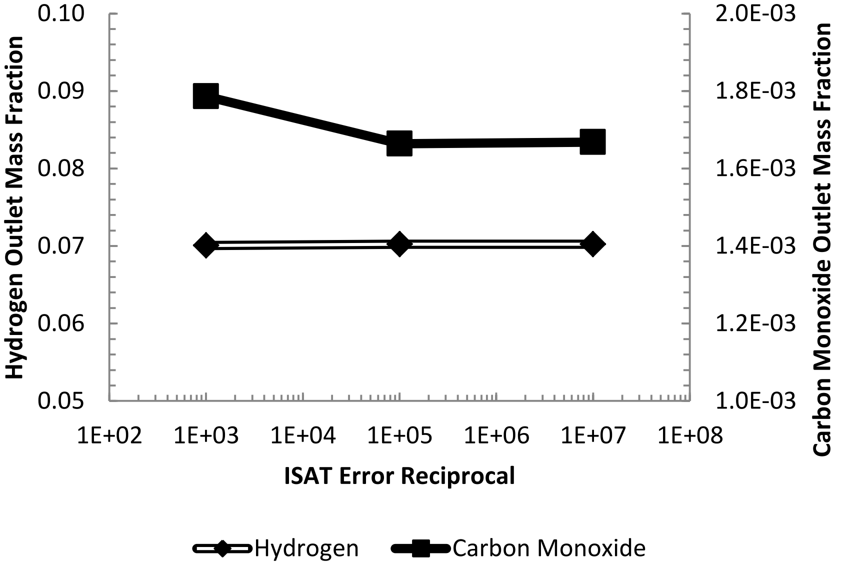

Figure 4-14: ISAT error tolerance solution independence study.

4.5.5.2: Achieving Grid Independence

The converged solution had to be checked for independence from the mesh. The base case Fluent simulation was also tested for solution grid independence. The mesh was refined until the outlet concentration of hydrogen and carbon monoxide became relatively unchanged (a change of less than 2% over a 50% increase in mesh cell count). Figure 4-15 shows that increasing the mesh size from 8,091 cells to 12,333 cells did not cause the simulation results to differ significantly. Therefore, from the mesh independence study it is evident that a coarser mesh could potentially be used to speed convergence. However, previous attempts to implement a coarser mesh were met with stability issues.

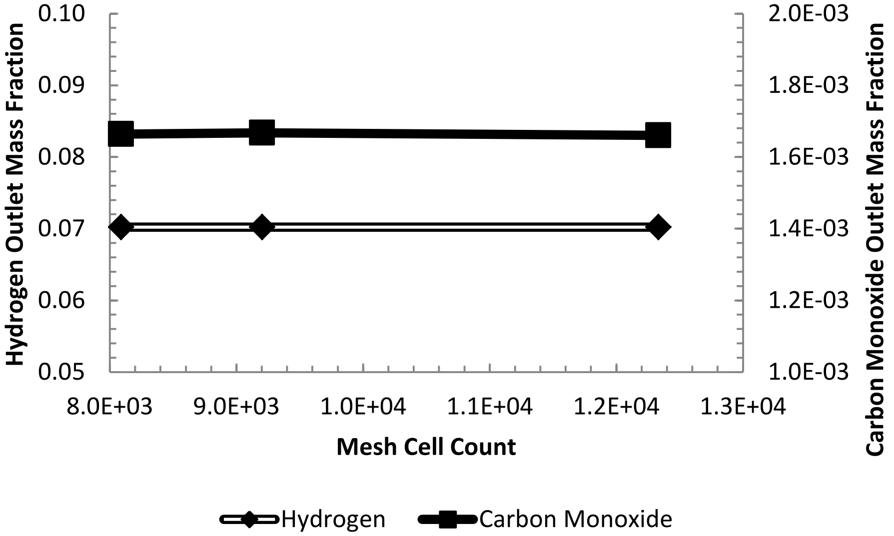

Figure 4-15: Solution grid independence study.

4.6: Fluent Model Results

The following sections outline the conclusions drawn from the ANSYS Fluent simulations. Simulation results and performance comparisons to the UniSim® RFC model are summarized in Appendix E. Any additional UDFs that were used when varying catalyst porosity are included in Appendix F.

4.6.1: Base Case Simulation

The base case simulation featured a constant catalyst layer porosity of 0.5. The base case reforming channel axial mole fraction profile (Figure 4-16) illustrates how 99% propylene conversion was achieved 7.6 mm into the 30 mm long reforming channel. The reforming channel required just 0.75 g of catalyst instead of the 2.95 g of catalyst that were provided. High propylene partial pressures allowed for high propylene conversion to be achieved near the reforming channel inlet. Furthermore, rapid propylene conversion near the reforming channel inlet was aided by effective heat transport from the flue gas channel to the reforming channel, with both channels achieving a uniform temperature approximately 0.6 mm into the reformer. As propylene was consumed, however, the consumption rate of propylene decreased, resulting in reduced rates of downstream hydrogen generation, as seen in Figure 4-16.

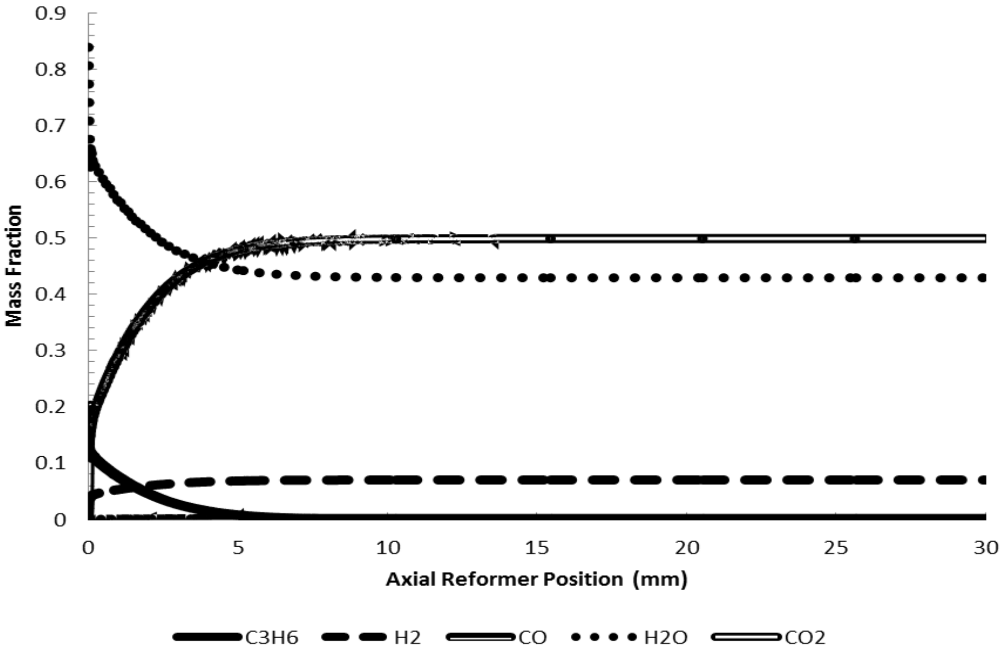

Figure 4-16: Base case reforming channel axial mass fraction profile.

The base case results indicate that shorter reformer channels, less catalyst, higher fluid velocities, and/or lower flue gas temperatures could be used for this case without significantly impacting reformer hydrocarbon conversion. Shorter reformer channels, less catalyst, and higher fluid velocities would allow for reformer cost reductions by reducing the requisite material per channel or by reducing the number of channels required. On the other hand, reduced flue gas temperatures would slow the reaction kinetics, would provide minimal net benefit to the RFC performance, and would not reduce reformer costs.

4.6.1.1: Reformer Steam to Carbon Ratio

The base case had a minimum steam to carbon ratio in the catalyst layer of 4.6. Such a high steam to carbon ratio, when combined with the reformer temperature, essentially eliminated any risk of carbon formation. In addition, high steam partial pressures drive the WGS reaction forwards, resulting in higher hydrogen yields and improved SOFC cell voltage. High steam partial pressures, however, increase SOFC activation and concentration losses, thus reducing SOFC performance. Therefore, picking an optimal steam to carbon ratio for the reformer is a balancing act between optimizing hydrogen yield and minimizing steam partial pressure.

4.6.2: Impact of Mass Transport Limitations on Reforming Channel and Catalyst Layer Species Concentration Profiles

The base case hydrogen mass fraction profile is shown in Figure 4-17. The delay in hydrogen being transferred through the catalyst layer and to the reforming channel is caused by radial transport resistances which limit the radial mixing of high hydrogen concentration zones located near the catalyst layer-wall boundary (associated with the higher reaction rates near the catalyst wall boundary shown in Figure 4-18 below). The hydrogen concentration delay becomes less impactful downstream from the reforming channel inlet because the higher hydrogen concentrations located further from the inlet result in improved axial and radial mass transfer.

The subsequent differences in hydrogen concentration between the catalyst layer-reforming channel boundary and the centre of the reforming channel is caused by a combination of radial mass transfer resistance as well as faster convective axial mass transfer near the centre of the reforming channel. The faster convective axial mass transfer near the centre of the reforming channel pushes lower hydrogen concentrations further downstream before full radial mixing can be achieved.

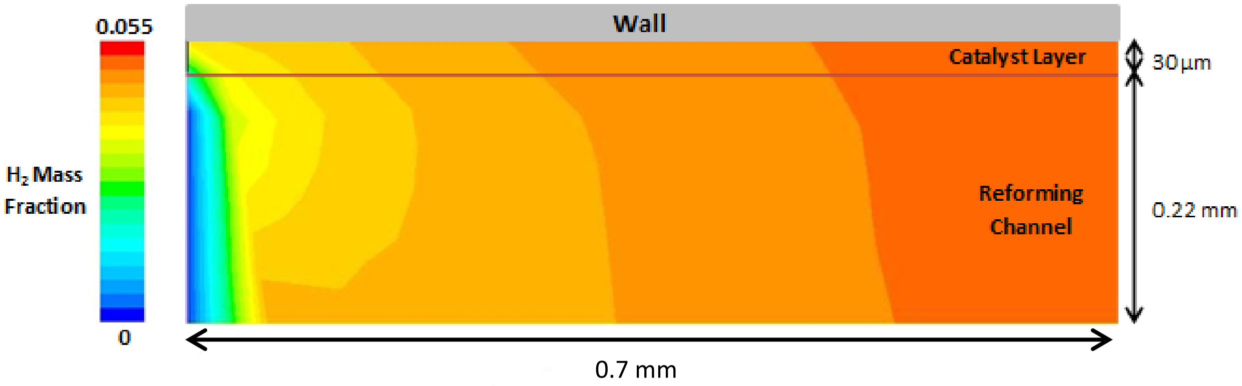

Figure 4-17: Base case reforming channel and catalyst layer hydrogen mass fraction profile.

4.6.3: Base Case Simulation UniSim® Coupling

The ANSYS Fluent base case reformer simulation outlet was inputted into the RFC 200 kW UniSim® model to replace the zero-dimensional reformer that had previously been modeled. The primary difference between the UniSim® and Fluent reformer results was the extent of the WGS reaction, with the UniSim® model having a 5.5% higher carbon monoxide mole percentage and a 5.7% higher steam mole percentage. The rapid reaction rate of WGS and the discrepancy between the UniSim® and Fluent results suggests a difference between the reaction equilibrium constants used by UniSim® and Xu and Froment [40]. Upon further investigation it was found that the equilibrium constants were within a 2% error. Therefore, the discrepancy in carbon monoxide outlet concentrations could be caused by a combination of high steam partial pressures, the species catalyst absorption coefficient constants used by Xu and Froment, as well as differences in species diffusion within the catalyst layer. The result was that the predicted reformer outlet carbon monoxide equilibrium concentration was not achieved in the Fluent simulation. Future modeling work should ensure that implemented WGS kinetics meet the expected species equilibrium concentrations.

Overall, the difference in WGS reaction equilibrium resulted in the Fluent model having a 5.7% higher hydrogen yield which led to an RFC electrical efficiency of 35.2%, 0.7% higher than the reported equilibrium steady state UniSim® RFC electrical efficiency. Furthermore, the higher reformer outlet temperature and higher hydrogen yield of the coupled Fluent model allowed for a lower air temperature and increased SOFC and tail gas burner heat output respectively. Therefore, the coupled Fluent model resulted in a high-quality CHP efficiency of 86.1% instead of the 49.0% of the original UniSim® model. Conclusively, a multi-dimensional reformer model tends to provide different outputs than a zero-dimensional model, with the multi-dimensional model's output seeming to result in the prediction of a more effective RFC.

4.6.4: Effect of Varying Catalyst Layer Thickness

The impact of catalyst layer thickness on reformer performance was evaluated by increasing the catalyst layer thickness from 30 μm to 50 μm. The thicker catalyst layer resulted in 99% propylene conversion in 65% of the reformer length (4.92 mm instead of 7.59 mm) needed for the thinner catalyst layer. The thicker catalyst layer reformer, however, required 13% more catalyst to achieve 99% propylene conversion. The thicker catalyst layer reformer suffered from lower catalyst utilization because of mass transport limitations in the thicker catalyst layer leading to lower reaction rates near the wall (see Figure 4-18). Overall, higher temperatures near the wall (Figure 4-19) caused higher local reaction rates, but mass transport limitations in the thicker catalyst layer resulted in lower propylene concentrations at the wall, leading to lower local reaction rates and by extension lower catalyst utilization. The thicker catalyst layer has higher wall-adjacent catalyst layer temperatures because of lower local endothermic heats of reaction associated with lower local reaction rates. Overall, a thicker catalyst layer allows for a shorter reforming channel, but without any means to improve radial mass transport within the catalyst layer the reformer with the thicker catalyst layer will require a larger catalyst volume.

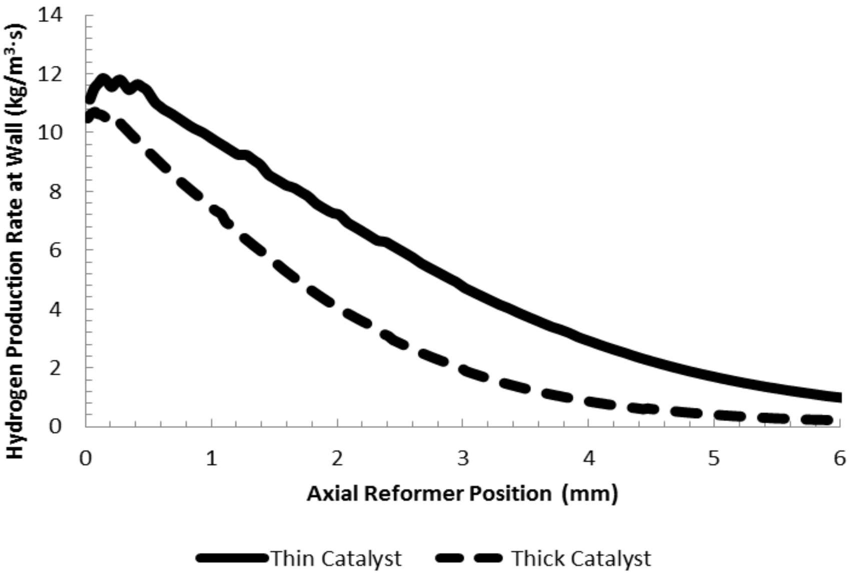

Figure 4-18: Wall-adjacent catalyst layer axial hydrogen production profiles for catalyst layer thicknesses of 30 μm and 50 μm.

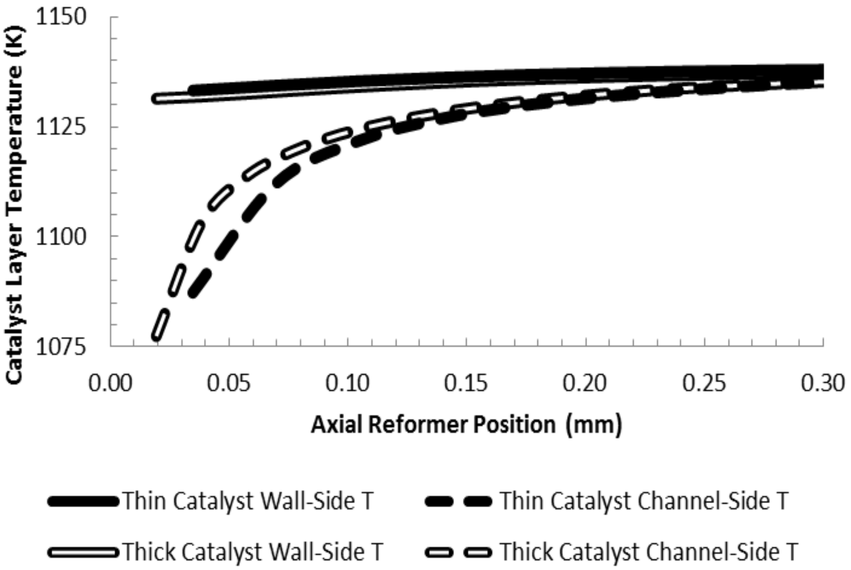

Figure 4-19: Catalyst Layer wall-adjacent and reforming channel-adjacent axial temperature profiles for catalyst layer thicknesses of 30 μm and 50 μm.

4.6.5: Effect of Varying Porosity along Reformer Length

Two simulations were conducted to determine the effects of catalyst layer porosity on reformer performance. The first simulation (Trial 1) determined the effects of increasing catalyst layer porosity along the length of the reformer. The second simulation (Trial 2) determined the effects of decreasing catalyst layer porosity along the length of the reformer. The catalyst layer axial porosity distributions of Trial 1, Trial 2, and of the base case are illustrated in Figure 4-20.

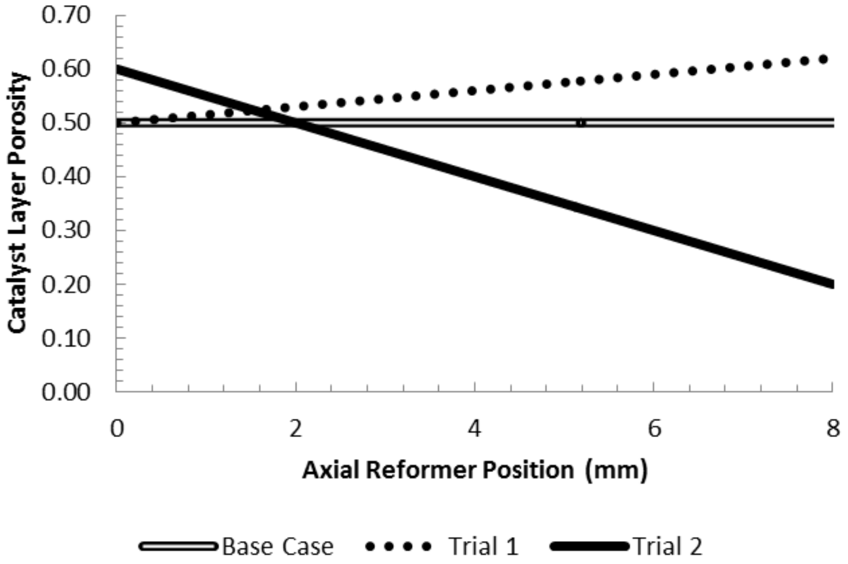

Figure 4-20: Catalyst layer axial porosity distributions for Trial 1, Trial 2, and for the base case.

Increasing the catalyst layer porosity along the length of the reformer resulted in reduced local propylene conversion as local reaction rates decreased with the reduction in available catalyst. The reduction in local propylene conversion resulted in a reformer that had to be 18% longer than the base case reformer (8.97 mm instead of 7.59 mm) to achieve 99% propylene conversion. The longer reformer also required 2% more catalyst than the base case reformer to achieve 99% propylene conversion. Conclusively, increasing catalyst layer porosity does not improve reformer performance, but instead reduces reformer performance. Increasing catalyst layer porosity along the length of the reformer does little to improve mass transport at regions of high reactant concentration located near the reforming channel inlet. Instead, the catalyst layer porosity distribution of Trial 1 improved mass transport further downstream at a point when mass transport is less limiting because of the presence of smaller reforming product species and where catalyst availability has become the greatest reaction limitation.

Trial 2 was conducted with a porosity that decreased along the reformer length with the objective of increasing catalyst availability downstream and of improving mass transport near the reforming channel inlet. The result of having higher catalyst layer porosity than the base case reformer at the reforming channel inlet was that propylene conversion values immediately downstream of the reforming channel inlet were lower than those for the base case reformer. Lower catalyst layer porosities further downstream the reforming channel in Trial 2, however, resulted in higher propylene conversions. The propylene conversion in Trial 2 surpassed the base case propylene conversion 4 mm downstream from the reforming channel inlet, at the conversion value of 90%. Therefore, Trial 2 resulted in a 99% propylene conversion reformer 2% shorter than the conversion equivalent base case reformer (7.44 mm instead of 7.59 mm).

Although Trial 2 allowed for the use of a shorter reformer to achieve 99% propylene conversion it required 2% more catalyst than the base case reformer. The catalyst utilization for Trial 2 and the catalyst utilization for the base case reformer are compared in Figure 4-21 and magnified in Figure 4-22 with the inclusion of the Damköhler number. The Damköhler number was defined as the quotient of the flow time scale and the chemical time scale. The catalyst utilization for Trial 2 is superior for propylene conversions between 52% and 95%, indicating that Trial 2 would require less catalyst than the base case to achieve propylene conversions within this range. Despite improved performance upstream, trial 2 catalyst utilization decreased below base case catalyst utilization for conversions above 95%, suggesting mass transfer limitations associated with lower catalyst porosities may have affected catalyst utilization.

Trial 2 mass transfer limitations near the reforming channel outlet are further illustrated by a sudden rise in Damköhler number (Figure 4-22). Overall, higher catalyst porosities near the reforming channel inlet are beneficial for reformer performance, but the rate at which catalyst porosity is reduced along the reformer length should be monitored to ensure that downstream catalyst utilization is not lower in comparison to the local catalyst utilization in higher porosity catalyst layers.

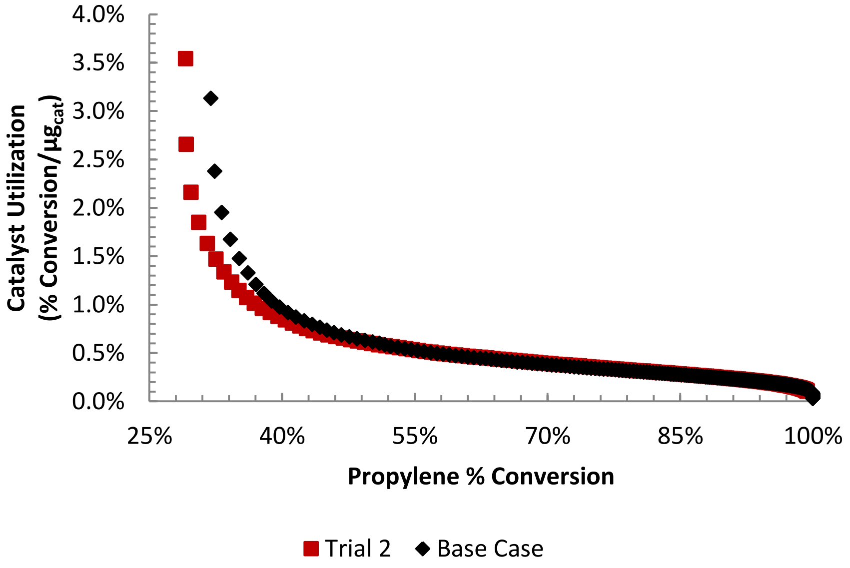

Figure 4-21: Catalyst utilization as a function of propylene conversion.

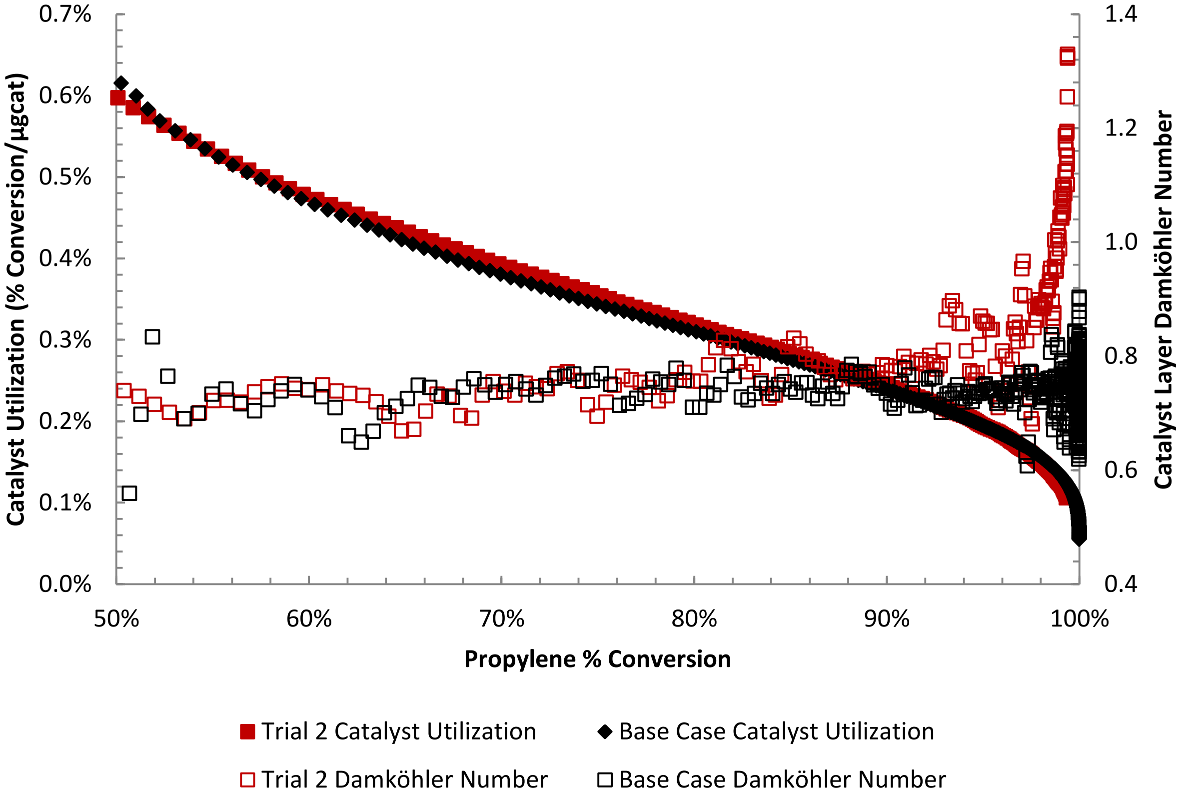

Figure 4-22: Magnified graphic of catalyst utilization as a function of propylene conversion.

4.7: Conclusion

In conclusion, model instability and long computation times associated with steam reformer modeling for large hydrocarbon molecules such as hexadecane makes three-dimensional reformer modeling impractical for any systematic optimization study and two-dimensional modeling extremely time consuming because of the very small time steps that must be used to ensure stability. However, previous research has shown that a three-dimensional square cross-section reformer can be represented by a circular cross-section reformer with channels of equal cross-sectional area and equivalent catalyst activity. Moreover, further work must be conducted in order to find suitable representative small hydrocarbons for larger hydrocarbon fuels to reduce convergence times of large hydrocarbon steam reforming models.

Propylene was used as a representative fuel for diesel along with a two-dimensional model in order to avoid the limitations associated with steam reforming models for large hydrocarbon molecules. The effects of catalyst layer thickness and of catalyst layer porosity distributions were studied to determine their effects on reformer performance. It was determined that increasing catalyst layer thickness resulted in a reduction in reformer length needed to achieve 99% propylene conversion. A thicker catalyst layer, however, required more catalyst to achieve the same conversion as a thinner catalyst layer because of radial mass transport limitations within the thicker catalyst layer resulting in reduced catalyst utilization. Moreover, it was determined that reducing catalyst layer porosity along the length of the reformer resulted in improved reformer performance as long as the axial reduction in catalyst layer porosity did not engender the downstream presence of excess catalyst.

4.8: References

[1] W. Ehrfeld, V. Hessel and H. Lowe, "Microreactors: New Technology for Modern Chemistry," *Organic Process Research & Development,* vol. 5, no. 1, p. 89, 2001.

[2] L. Kiwi-Minsker and A. Renken, "Microstructured Reactors for Catalytic Reactions," *Catalysis Today,* vol. 110, pp. 2-14, 2005.

[3] G. Arzamendi, P. M. Dieguez, M. Montes, M. A. Centeno, J. A. Odriozola and L. M. Gandia, "Integration of Methanol Steam Reforming and Combustion in a Microchannel Reactor for H2 Production: A CFD Simulation Study," *Catalysis Today,* vol. 143, pp. 25-31, 2009.

[4] J. E. Kent and A. G. Dixon, "Steam Reforming of Biodiesel By-Product Glycerol," Worcester Polytechnic Institute, 2013.

[5] J. Aubin, L. Prat, C. Xuereb and C. Gourdon, "Effect of Microchannel Aspect Ratio on Residence Time Distributions and the Axial Dispersion Coefficient," *Chemical Engineering and Processing,* vol. 48, pp. 554-559, 2009.

[6] M. Karakaya and A. K. Avci, "Microchannel Reactor Modeling for Combustion Driven Reforming of Iso-Octane," *Internation Journal of Hydrogen Energy,* vol. 36, pp. 6569-6577, 2011.

[7] O. Y. Caglar, C. D. Demirhan and A. K. Avci, "Modeling and Design of a Microchannel Reformer for Efficient Conversion of Glycerol to Hydrogen," *International Journal of Hydrogen Energy,* vol. 40, pp. 7579-7585, 2015.

[8] M. Zanfir and A. Gavriilidis, "Catalytic Combustion Assisted Methane Steam Reforming in a Catalytic Plate Reactor," *Chemical Engineering Science,* vol. 58, pp. 3947-3960, 2003.

[9] N. Mladenov, J. Koop, S. Tischer and O. Deutschmann, "Modeling of Transport and Chemistry in Channel Flow of Automotive Catalytic Converters," *Chemical Engineering Science,* vol. 65, pp. 812-826, 2010.

[10] S. T. Kolaczkowski, R. Chao, S. Awdry and A. Smith, "Application of a CFD Code (Fluent) to Formulate Models of Catalytic Gas Phase Reactions in Porous Catalyst Pellets," *Chemical Engineering Research and Design,* vol. 85, no. 11, pp. 1539-1552, 2007.

[11] E. Massing, J. F. Brilhac, A. Brillard, P. Gilot and G. Prado, "Modelling of the Behaviour of a Three Way Catalytic Converter at Steady State Influence of the Propene Diffusion Inside the Catalytic Layer," *Chemical Engineering Science,* vol. 55, pp. 1707-1716, 2000.

[12] Symscape, "Polyhedral, Tetrahedral, and Hexahedral Mesh Comparison," Feb. 2013. [Online]. Available: http://www.symscape.com/polyhedral-tetrahedral-hexahedral-mesh-comparison. [Accessed 2016].

[13] "ANSYS Fluent Theory Guide," ANSYS Inc., Canonsburg, PA, USA, 2016.

[14] "ANSYS Fluent User's Guide," ANSYS Inc., Canonsburg, PA, USA, 2016.

[15] H. Dhingra and B. A. Peppley, "Sensitivity Analysis of a 1 kW Diesel-Fuelled SOFC Generator: A Single and Paired-Variable Study," *Jounral of Power Sources,* vol. 239, pp. 527-537, 2013.

[16] L. Shi, D. J. Bayless and M. E. Prudich, "A CFD Model of Autothermal Reforming," *Internation Journal of Hydrogen Energy,* vol. 34, pp. 7666-7675, 2009.

[17] R. D. Parmar, "A Combined Gas-Phase and Surface Reaction Mechanistic Model of Diesel Surrogate Reforming for SOFC Application," Queen's University, Kingston, 2013.

[18] J. R. Rostrup-Nielsen, T. S. Christensen and I. Dybkjaer, "Steam Reforming of Liquid Hydrocarbons," *Studies in Surface Science and Catalysis,* vol. 113, pp. 81-95, 1998.

[19] Y. Mizutani, M. Tamura, M. Kawai, K. Nomura and Y. Nakamura, "Characterization of the Sc2O3-ZrO2 System and its Application as the Electrolyte in Planar SOFC," in *Proceedings of the Fourth International Symposium on Solid Oxide Fuel Cells*, Pennington, USA, 1995.

[20] A. T. Naseri, B. A. Peppley, J. G. Pharoah, P. Mandal, S. Litster and N. Abatzoglou, "X-Ray Tomography-Based Analysis of Transport and Reaction in the Catalyst Coating of a Reformer," *Chemical Engineering Science,* vol. 138, pp. 499-509, 2015.

[21] "Water," National Institute of Standards and Technology, 1998. [Online]. Available: http://webbook.nist.gov/cgi/cbook.cgi?ID=C7732185&Mask=1. [Accessed Jan. 2015].

[22] F. Ullmann, Ullmann's Encyclopedia of Industrial Chemistry, Weinheim, DE , 2011.

[23] JLC Electromet Pvt. Ltd., "Nickel Chrome Alloys," 2015. [Online]. Available: http://www.nickel-alloys.net/nickel_chrome_alloys.html. [Accessed 2015].

[24] The Goodfellow Group, "Alumina (Al2O3): Material Information," 2016. [Online]. Available: http://www.goodfellow.com/E/Alumina.html. [Accessed 2016].

[25] A. D. Rakic, A. B. Djurisic, J. M. Elazar and M. L. Majewski, "Optical Properties of Metallic Films for Vertical-Cavity Optoelectronic Devices," *Applied Optics,* vol. 37, no. 22, pp. 5271-5283, 1998.

[26] S. Ergun, "Fluid Flow through Packed Columns," *Chemical Engineering Progress,* vol. 48, no. 2, pp. 89-94, 1952.

[27] W. He, W. Lv and J. Dickerson, "Gas Diffusion Mechanisms and Models," in *Gas Transport in Solid Oxide Fuel Cells*, Springer Publishing, 2014, pp. 9-17.

[28] R. E. Cunningham and R. J. Williams, Diffusion in Gases and Porous Media, New York, USA: Plenum Press, 1980.

[29] B. E. Poling, J. M. Prausnitz and J. P. O'Connell, "Diffusion Coefficients," in *The Properties of Gases and Liquids*, The McGraw-Hill Companies Inc., 2001.

[30] P. D. Neufeld, A. R. Janzen and R. A. Aziz, "Empirical Equations to Calculate 16 of the Transport Collision Integrals for the Lennard-Jones (12-6) Potential," *Journal of Chemical Physics,* vol. 57, pp. 1100-1102, 1972.

[31] C. R. Wilke, "Diffusional Properties of Multicomponent Gases," *Chemical Engineering Progress,* vol. 46, pp. 95-104, 1950.

[32] H. A. McGee, Molecular Engineering, New York, USA: McGraw-Hill, 1991.

[33] P. Sadooghi and R. Rauch, "Experimental and Modeling Study of Catalytic Steam Reforming of Methane Mixture with Propylene in a Packed Bed Reactor," *Internation Journal of Heat and Mass Transfer,* vol. 78, pp. 515-521, 2014.

[34] J. L. Figueiredo and D. L. Trimm, "Carbon Formation on Unsupported and Supported Nickel Catalysts," *Journal of Chemical Technology and Biotechnology,* vol. 28, no. 9, pp. 611-616, 1978.

[35] J. R. Rostrup-Nielsen and B. Hansen, "CO2-Reforming of Methane over Transition Metals," *Journal of Catalysis,* vol. 144, pp. 38-49, 1993.

[36] D. L. Trimm and Z. I. Onsan, "Onboard Fuel Conversion for Hydrogen-Fuel-Cell-Driven Vehicles," *Catalysis Reviews,* vol. 43, no. 1-2, pp. 31-84, 2001.

[37] J. R. Rostrup-Nielsen, J. Sehested and J. K. Norskov, "Hydrogen and Synthesis Gas by Steam- and CO2 reforming," *Advances in Catalysis,* vol. 47, pp. 65-139, 2002.

[38] D. J. Liu, T. D. Kaun, H. K. Liao and S. Ahmed, "Characterization of Kilowatt-Scale Autothermal Reformer for Production of Hydrogen from Heavy Hydrocarbons," *International Journal of Hydrogen Energy,* vol. 29, pp. 1035-1046, 2004.

[39] J. Thormann, L. Maier, P. Pfeifer, U. Kunz, O. Deutschmann and K. Schubert, "Steam Reforming of Hexadecane over a Rh/CeO2 Catalyst in Microchannels: Experimental and Numerical Investigation," *International Journal of Hydrogen Energy,* vol. 34, pp. 5108-5120, 2009.

[40] J. Xu and G. F. Froment, "Methane Steam Reforming, Methanation and Water-Gas Shift: I. Intrinsic Kinetics," *AlChE Journal,* vol. 35, no. 1, pp. 88-96, 1989.

[41] M. F. Modest, "Radiative Properties of Molecular Gases," in *Radiative Heat Transfer*, Oxford, UK, Elsevier Inc., 2013, pp. 303-386.

[42] K. P. Birch, "Refractive," in *Kaye & Laby: Tables of Physical & Chemical Constants*, National Physical Laboratory, 1995.

[43] H. C. Hottel, "Radiant Heat Transmission," in *Heat Transmission*, New York, USA, McGraw-Hill, 1954.

[44] H. C. Hottel and A. F. Sarofim, Radiative Transfer, New York, USA: McGraw-Hill, 1967.

[45] A. Coppalle and P. Vervisch, "The Total Emissivities of High-Temperature Flames," *Combustion and Flame,* vol. 49, no. 1-3, pp. 101-108, 1983.

[46] M. K. Denison and B. W. Webb, "A Spectral Line-Based Weighted-Sum-of-Gray-Gases Model for Arbitrary RTE Solvers," *Journal of Heat Transfer,* vol. 115, no. 4, pp. 1002-1012, 1993.

[47] T. F. Smith, Z. F. Shen and J. N. Friedman, "Evaluation of Coefficiencts for the Weighted Sum of Gray Gases Model," *Journal of Heat Transfer,* vol. 104, no. 4, pp. 602-608, 1982.

[48] D. K. Edwards and R. Matavosian, "Scaling Rules for Total Absorptivity and Emissivity of Gases," *Journal of Heat Transfer,* vol. 106, no. 4, pp. 684-689, 1984.

[49] R. Siegel and J. R. Howell, Thermal Radiation Heat Transfer, Washington, USA: Hemisphere Publishing Corporation, 1992.

[50] P. Hanrahan and W. Krueger, "Reflection from Layered Surfaces due to Subsurface Scattering," in *Proceedings of the 20th Annual Conference on Computer Graphics and Interactive Techniques*, New York, USA, 1993.

[51] M. F. Modest, "Fundamentals of Thermal Radiation," in *Radiative Heat Transfer*, Oxford, UK, Elsevier Inc., 2013, pp. 1-30.

[52] M. Baerns, Basic Principles in Applied Catalysis, Springer Science & Business Media, 2013.

[53] T. Popa, G. Xu, T. F. Barton and M. D. Argyle, "High Temperature Water Gas Shift Catalysts with Alumina," *Applied Catalysis A: General,* vol. 379, pp. 15-23, 2010.

[54] Transmetra GmbH, "Table of Emissivity of Various Surfaces," Mikron Instrument Company Inc., Schaffhausen, SUI, 2003.

Chapter 5: Conclusions and Recommendations for Future Work

The goal of this research was to study the environmental and economic impact of replacing diesel generators in Canadian remote communities with RFCs as well as to formulate a diesel reformer model based on previous work by Naseri *et al.* and to study the sensitivity of the reformer to changes in catalyst volume.

5.1: Reformer and Fuel Cell System UniSim® Model

A steady state UniSim® model was created to study the impact of a diesel-fed electricity generating system comprised of a steam reformer and SOFC stack on Canadian remote community electricity generation. The UniSim® model was optimized for a 100 kW load. The RFC performance was then compared to the performance of various diesel generator setups for a remote community with a peak load of 150 kW and an average load of approximately 100 kW. The RFC had an average annual electrical efficiency of 45.30%, with a minimum electrical efficiency of 39.96% that exceeded the maximum diesel generator efficiency of 36.49%. Extrapolating the RFCs performance from the test case remote community to all fossil fuel reliant Canadian remote communities indicates that replacing diesel generators with RFCs would result in CO_2 equivalent savings comparable to removing 37,000 cars from the road. The modeled RFC, however, is not economically feasible given the current SOFC technology, but a hypothetical end of 2017 implementation of the yet unreleased Redox Cube would result in a 9 to 12 year payback period depending on the remote community's diesel generator setup. Moreover, implementing the Redox Cube in all fossil fuel reliant Canadian remote communities would result in total savings approaching $1 billion after 20 years of operation, without taking future advancements in SOFC technology into account.

5.1.1: Future Work

Future work should focus on the modeling of RFCs for individual remote communities, taking into account each community's environmental conditions, diesel supply, and current diesel generation setup.

5.2: Reformer Fluent Model

A steady state diesel reformer model was created using ANSYS Fluent. At first the diesel reformer was modeled in three dimensions and used hexadecane as a diesel surrogate. Hexadecane steam reforming caused large density fluctuations that resulted in long computation times and model instability. Therefore, the model was re-done in two dimensions and with a smaller hydrocarbon as a fuel feed. The use of a two-dimensional model only limited the study by eliminating the possibility of studying the effects of reformer channel aspect ratios on reformer performance. A smaller hydrocarbon was implemented as a fuel feed by accounting for hexadecane gas-phase reactions that were assumed to result in 100% conversion to propylene.

This work re-iterated a theory prevalent in literature that increased catalyst layer thickness allows for the use of a shorter reforming channel, but results in the need for larger catalyst volumes because of increased mass transport limitations within the catalyst layer. Furthermore, this work demonstrated that reducing the catalyst layer porosity along the length of the reformer can help achieve improved reformer performance since lower downstream porosities help maintain adequate levels of reactant consumption despite low reactant partial pressures.

5.2.1: Future Work

Future work should focus on filling gaps in the current literature by further studying the impact of geometry and fluid parameters on reformer performance, with a focus on further optimizing the catalyst layer thickness and porosity distribution. It would be beneficial for a study to be conducted to determine whether it is beneficial to gradually increase catalyst layer thickness instead of gradually reducing catalyst layer porosity. Most of the current literature comprises two-dimensional methane reforming models. Therefore, the focus of future work should be to evaluate fluid and geometry parameter effects using a computationally lengthy large hydrocarbon reforming model. Future work with large hydrocarbon reforming models should also focus on determining methods to accurately model large hydrocarbon reforming in shorter timeframes, such as establishing adequate surrogate fuel compositions for large hydrocarbon fuels.

Appendix A: UniSim® Optimized RFC Stream Table

A complete stream table of the optimized RFC case is enclosed in Table A1 and Table A2.

Table A1: Optimized RFC 100 kW Stream Table 1

System Feed		
Mass Flow Rate (kg/h)	H_2O	91.08
	Diesel ($C_{16}H_{34}$)	17.51
	Air	482.48
Inlet Temperature (°C)		25
Pressure (kPa)		101.325
System Operating Pressure (kPa)		120
Feed Temperature after Heating (°C)	H_2O	800
	$C_{16}H_{34}$	300 (liquid)
	Air	900
Heat Exchanger Network Heat Load (kJ/h)	Air	75.71
	Steam	61.98
	Diesel HEX	27.59
Parasitic Losses (kW)		2.65
Reformer		
Temperature (°C)		693
Heat Load (kJ/h)		29.06
Inlet Molar S/C Ratio		4.67
Outlet Mass %	H_2O	50.07
	$C_{16}H_{34}$	0.00
	H_2	6.20
	CO	10.94
	CO_2	32.70
	CH_4	0.09
Outlet Mole %	H_2O	39.74
	$C_{16}H_{34}$	0.00
	H_2	43.98
	CO	5.59
	CO_2	10.62
	CH_4	0.08

Table A2: Optimized RFC 100 kW Stream Table 2

Fuel Cell Stack		
Average Temperature (°C)		946
Fuel Utilization		0.8
Oxygen Utilization		0.4
Voltage per Cell (V/cell)		0.6972
Current (A)		24.75
Cell Count		5,948
Total Power Generated (kW)		102.65
Net Power Output (kW)		100
Electrical Efficiency (%)		47.45
Outlet Mass %	H_2O	17.14
	H_2	0.24
	CO	1.69
	CO_2	6.58
	CH_4	0.00
	N_2	61.79
	O_2	11.44
	Ar	1.13
Tail Gas Burner		
Outlet Temperature (°C)		1,370
Available Excess Heat (kJ/h)	High Quality Heat (T > 100°C)	2.53
	Low Quality Heat (T > 25°C)	54.25
Combined Heat and Power Efficiencies (%)	High Quality Heat	49.43
	Low Quality Heat	89.98
Outlet Mass %	H_2O	19.23
	H_2	0.00
	CO	0.00
	CO_2	9.23
	CH_4	0.00
	N_2	61.73
	O_2	8.53
	Ar	1.13
	NO	0.14
	NO_2	0.00

Table A3 presents relevant performance parameters for operation of the optimized RFC at electrical loads of 26 kW to 207 kW.

Table A3: Optimized 100 kW Reformer and Fuel Cell System Performance from 25 kW to 200 kW

Net Power Output	**Total Power Generated**	**Parasitic Losses**	**Electrical Efficiency**	**Mass Flow Rate (kg/h)**			**Avg. Fuel Cell Temperature**	**Combined Heat and Power Efficiency (%)**	
kW	**kW**	**kW**	**%**	**H_2O**	**$C_{16}H_{34}$**	**Air**	**^{o}C**	**High Quality**	**Low Quality**
206.52	213.91	7.39	34.43	259.21	49.83	1,344.05	996.40	49.04	89.77
197.62	204.44	6.83	35.85	238.19	45.79	1,240.66	990.50	49.09	89.81
187.54	193.79	6.26	37.32	217.18	41.75	1,137.27	984.65	49.12	89.82
176.42	182.01	5.59	38.87	196.16	37.71	1,016.65	979.40	49.22	89.90
163.85	168.87	5.02	40.43	175.14	33.67	913.26	973.05	49.28	89.92
154.76	159.40	4.64	41.51	161.13	30.98	844.34	969.15	49.30	89.94
145.08	149.34	4.26	42.62	147.12	28.28	775.41	964.80	49.32	89.95
134.78	138.66	3.89	43.76	133.11	25.59	706.49	959.95	49.32	89.94
123.84	127.35	3.51	44.94	119.10	22.90	637.56	955.15	49.32	89.94
112.31	115.34	3.03	46.19	105.09	20.20	551.40	951.70	49.45	90.00
100.00	102.65	2.65	47.45	91.08	17.51	482.48	946.40	49.43	89.98
93.57	96.04	2.46	48.10	84.07	16.16	448.02	944.05	49.46	90.00
86.95	89.22	2.27	48.76	77.06	14.82	413.55	941.20	49.44	89.98
73.17	75.06	1.90	50.15	63.05	12.12	344.63	935.60	49.38	89.94
58.59	60.01	1.42	51.63	49.04	9.43	258.47	931.30	49.58	90.02
43.08	44.12	1.04	53.15	35.03	6.73	189.54	925.40	49.55	90.00
26.62	27.28	0.66	54.73	21.02	4.04	120.62	918.75	49.30	89.86

Appendix B: Electrical Efficiencies of the RFC and the Diesel Generator Systems

The electrical efficiencies of the RFC and GEN2 are compared in Figure B-1 using the test case remote community's electricity demand curves.

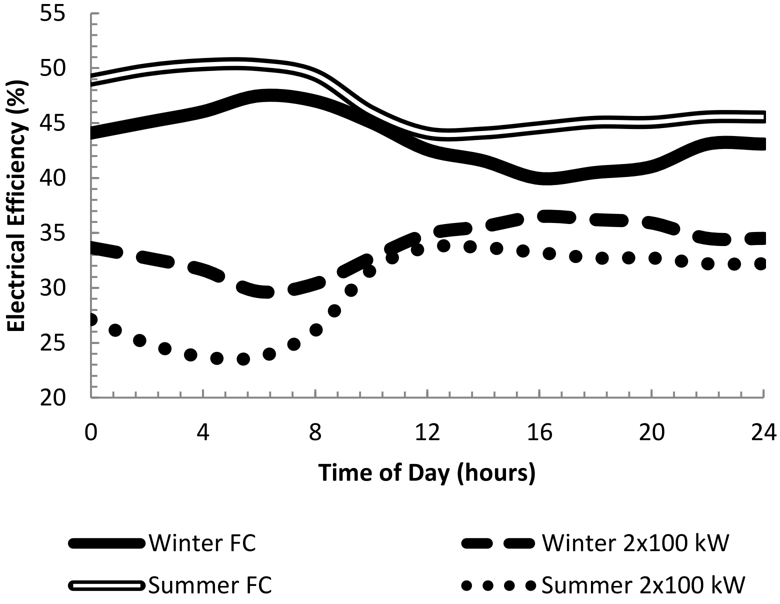

Figure B-1: Summer and winter electrical efficiencies for the RFC and the 100 kW diesel generator setup.

The electrical efficiencies of the RFC and GEN3 are compared in Figure B-2 using the test case remote community's electricity demand curves.

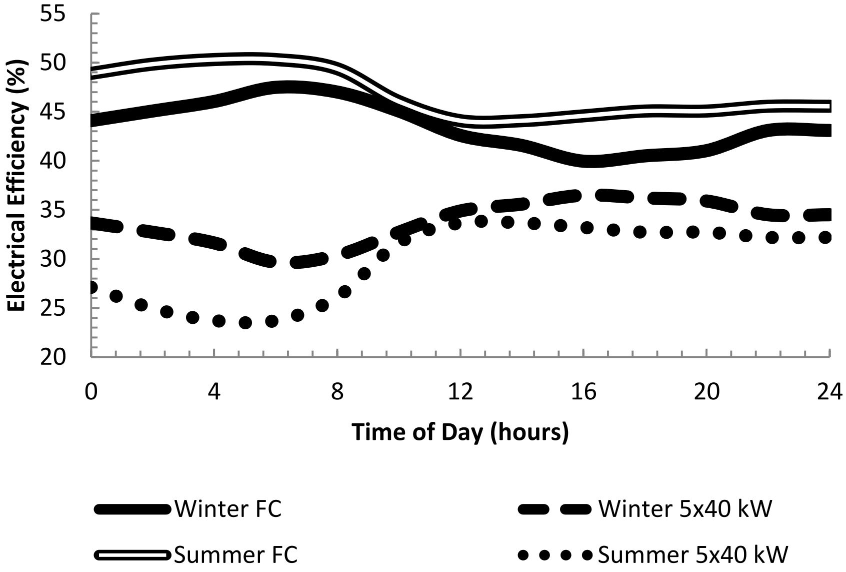

Figure B-2: Summer and winter electrical efficiencies for the RFC and the 40 kW diesel generator setup.

Appendix C: Fluent Model Inputs

Fluent Meshes

The base case mesh is shown in Figure C3 and the mesh for the thicker catalyst layer trial is shown in Figure C4. Size and quality information for both the base case mesh and the thicker catalyst layer trial mesh are summarized in Table C4. Skewness above 0.25 is considered by ANSYS to result in “good” cell quality, while skewness below 0.25 is considered to result in “excellent” cell quality [1]. Moreover, ANSYS considers an aspect ratio below 20 to be acceptable for mesh cells.

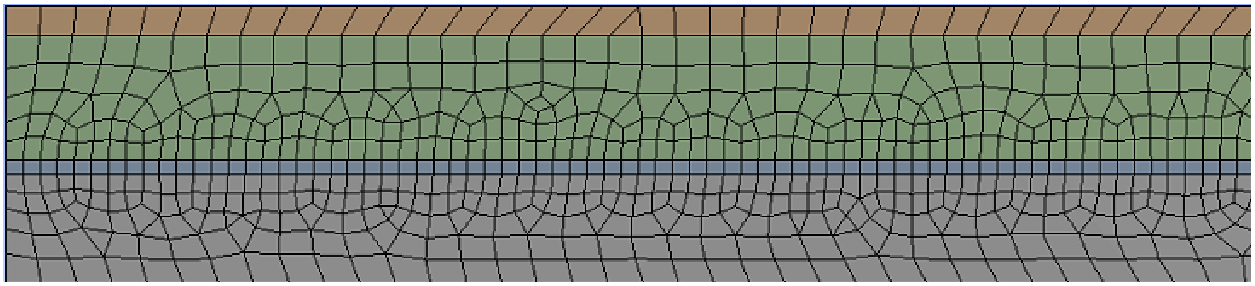

Figure C3: Base case ANSYS Fluent simulation mesh. The orange region represents the flue gas channel, the green region represents the wall, the blue region represents the catalyst layer, and the grey region represents the reforming channel.

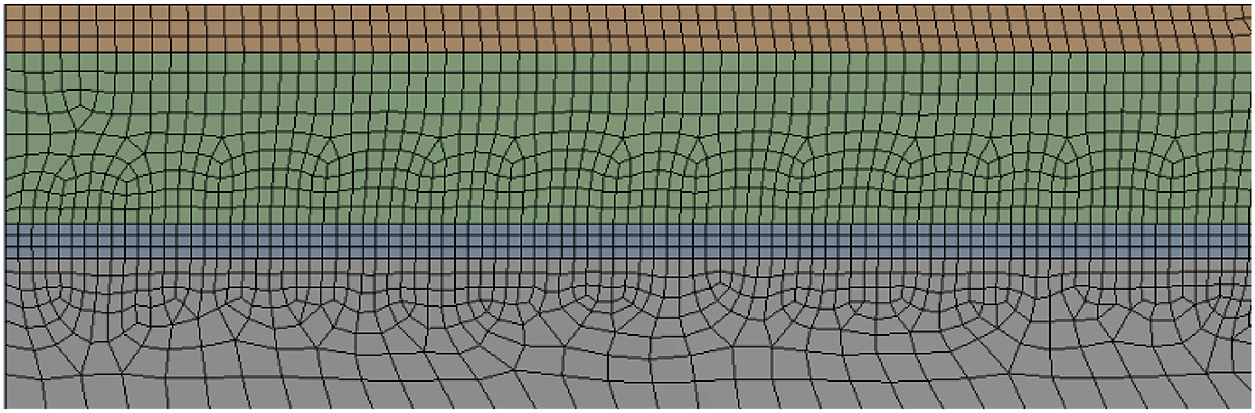

Figure C4: ANSYS Fluent simulation mesh for the 50 µm thick catalyst layer trial. The orange region represents the flue gas channel, the green region represents the wall, the blue region represents the catalyst layer, and the grey region represents the reforming channel.

Table C4: Mesh Size and Quality Information

Parameter	Base Case Mesh	Thicker Catalyst Layer Trial Mesh
Cell Count	8,091	11,132
Maximum Orthogonal Skew	0.334099	0.327733
Maximum Aspect Ratio	4.94524	4.43285

Steam Property Data

Steam property data is summarized in Table C5. Equations C1 to C4 summarize the data presented in Table C5 and were input into Fluent.

$$\rho_{H_2O} = 2.0519 \cdot 10^{-19}T^6 - 1.6614 \cdot 10^{-15}T^5 + 5.5865 \cdot 10^{-12}T^4 - 1.0082 \cdot 10^{-8}T^3 + 1.0511 \cdot 10^{-5}T^2 - 6.3073 \cdot 10^{-3}T + 2.0083 \tag{C1}$$

$$C_{P,H_2O} = 1.7186 \cdot 10^{-17}T^6 - 1.3387 \cdot 10^{-13}T^5 + 9.5064 \cdot 10^{-10}T^4 - 2.7192 \cdot 10^{-6}T^3 + 3.3441 \cdot 10^{-3}T^2 - 1.1693T + 2.0031 \cdot 10^3 \tag{C2}$$

$$k_{H_2O} = -4.2372 \cdot 10^{-17}T^5 + 2.0997 \cdot 10^{-13}T^4 - 4.2592 \cdot 10^{-10}T^3 + 4.6456 \cdot 10^{-7}T^2 - 1.4095 \cdot 10^{-4}T + 3.1796 \cdot 10^{-2} \tag{C3}$$

$$\mu_{H_2O} = -6.9872 \cdot 10^{-21}T^5 + 3.6880 \cdot 10^{-17}T^4 - 7.7884 \cdot 10^{-14}T^3 + 7.6428 \cdot 10^{-11}T^2 + 6.6953 \cdot 10^{-9}T + 2.4601 \cdot 10^{-6} \tag{C4}$$

Table C5: Steam Property Data

T (K)	ρ (kg/m^3) [2]	C_p (J/kg-K) [2]	k (W/m-K) [3]	μ (kg/m-s) [3]
473	0.5523	1955	0.0335	1.62E-05
573	0.4550	2014	0.0434	2.03E-05
673	0.3869	2080	0.0548	2.44E-05
773	0.3366	2148	0.0670	2.86E-05
873	0.2980	2214	0.0799	3.26E-05
973	0.2673	2276	0.0934	3.65E-05
1073	0.2423	2335	0.1073	4.04E-05
1173	0.2217	2391	0.1217	4.41E-05
1273	0.2042	2446	0.1363	4.77E-05
1373	0.1893	2504		
1473	0.1765	2568		
1573	0.1653	2646		
1673	0.1554	2743		
1773	0.1466	2869		
1873	0.1388	3033		

Propylene Property Data

Propylene property data is summarized in Table C6. Equations C5 to C8 summarize the data presented in Table C6 and were input into Fluent.

$$\rho_{C_3H_6} = (1.4403 \cdot 10^{-19}T^6 - 1.1512 \cdot 10^{-15} \cdot T^5 + 3.8107 \cdot 10^{-12} \cdot T^4 - 6.7983 \cdot 10^{-9}T^3 + 7.1668 \cdot 10^{-6}T^2 - 4.6673 \cdot 10^{-3}T + 1.9725 \qquad \text{(C5)}$$

$$C_{p,C_3H_6} = 2.0731 \cdot 10^{-18}T^6 - 1.6159 \cdot 10^{-14}T^5 + 5.1527 \cdot 10^{-11}T^4 + 4.3736 \cdot 10^{-7}T^3 - 2.245 \cdot (10^{-3}T^2 + 4.1406T + 1.4261 \cdot 10^3 \qquad \text{(C6)}$$

$$k_{C_3H_6} = 4.6515 \cdot 10^{-22}T^6 - 5.3305 \cdot 10^{-18}T^5 + 3.225 \cdot 10^{-14}T^4 - 8.0128 \cdot 10^{-11}T^3 + 7.4093 \cdot 10^{-8}T^2 + 1.0082 \cdot 10^{-4}T + 1.3924 \cdot 10^{-2} \qquad \text{(C7)}$$

$$\mu_{C_3H_6} = -9.0164 \cdot 10^{-25}T^6 + 8.0135 \cdot 10^{-21}T^5 - 2.9933 \cdot 10^{-17}T^4 + 6.0293 \cdot 10^\wedge - 14T^3 - 6.8112 \cdot 10^{-11}T^2 + 5.8329 \cdot 10^{-8}T + 4.1182 \cdot 10^{-6} \qquad \text{(C8)}$$

Table C6: Propylene Property Data

T (K)	ρ (kg/m^3) [2]	C_p (J/kg-K) [2]	k (W/m-K) [2]	μ (kg/m-s) [2]
273	1.1140	2398	0.0455	1.61E-05
373	0.9407	2682	0.0583	1.89E-05
473	0.8141	2931	0.0712	2.16E-05
573	0.7177	3149	0.0841	2.38E-05
673	0.6417	3338	0.0968	2.58E-05
773	0.5803	3502	0.1093	2.77E-05
873	0.5296	3644	0.1213	2.95E-05
973	0.4871	3766	0.1330	3.13E-05
1073	0.4509	3873	0.1443	3.31E-05
1173	0.4198	3967	0.1552	3.49E-05
1273	0.3926	4051	0.1659	3.67E-05
1373	0.3688	4129	0.1763	3.85E-05
1473	0.3477	4204	0.1867	4.04E-05
1573	0.3288	4278	0.1971	4.23E-05
1673	0.3119	4355	0.2077	4.42E-05
1773	0.2967	4438	0.2187	4.61E-05
1873	0.2829	4531	0.2303	4.80E-05
1973	0.2703	4635	0.2426	4.99E-05

Hydrogen Property Data

Hydrogen property data is summarized in Table C7. Equations C9 to C12 summarize the data presented in Table C7 and were input into Fluent.

$$\rho_{H_2} = 6.011 \cdot 10^{-20}T^6 - 4.6177 \cdot 10^{-16}T^5 + 1.4443 \cdot 10^{-12}T^4 - 2.3659 \cdot 10^{-9}T^3 + 2.1723 \cdot 10^{-6}T^2 - 1.1071 \cdot 10^{-3}T + 2.873 \cdot 10^{-1} \quad \text{(C9)}$$

$$C_{p,H_2} = 4.1554 \cdot 10^{-17}T^6 - 2.9837 \cdot 10^{-13}T^5 + 8.9267 \cdot 10^{-10}T^4 - 1.6279 \cdot 10^{-6}T^3 + 1.9935 \cdot 10^{-3}T^2 + 2.300 \cdot 10^{-1}T + 1.3894 \cdot 10^{4} \quad \text{(C10)}$$

$$k_{H_2} = 1.8808 \cdot 10^{-16}T^4 + 1.5526 \cdot 10^{-10}T^3 - 4.1406 \cdot 10^{-7}T^2 + 6.6752 \cdot 10^{-4}T + 8.5598 \cdot 10^{-3} \quad \text{(C11)}$$

$$\mu_{H_2} = 5.5234 \cdot 10^{-24}T^6 - 4.5524 \cdot 10^{-20}T^5 + 1.4994 \cdot 10^{-16}T^4 - 1.9892 \cdot 10^{-13}T^3 + 1.0466 \cdot 10^{-10}T^2 + 4.755 \cdot 10^{-9}T + 2.7021 \cdot 10^{-6} \quad \text{(C12)}$$

Table C7: Hydrogen Property Data

T (K)	ρ (kg/m^3) [2]	C$_p$ (J/kg-K) [2]	k (W/m-K) [2]	μ (kg/m-s) [2]
273	0.1064	14077	0.1631	8.53E-03
373	0.0779	14187	0.2080	1.13E-02
473	0.0615	14315	0.2481	1.38E-02
573	0.0508	14454	0.2843	1.59E-02
673	0.0432	14601	0.3176	1.77E-02
773	0.0376	14756	0.3489	1.92E-02
873	0.0333	14916	0.3792	2.07E-02
973	0.0299	15081	0.4093	2.25E-02
1073	0.0271	15247	0.4401	2.50E-02
1173	0.0248	15415	0.4728	2.84E-02
1273	0.0229	15583	0.5081	3.31E-02
1373	0.0212	15749	0.5470	3.94E-02
1473	0.0197	15913	0.5905	4.77E-02
1573	0.0185	16073	0.6395	5.82E-02
1673	0.0174	16229	0.6949	7.12E-02
1773	0.0164	16380	0.7577	8.71E-02
1873	0.0155	16525	0.8287	1.06E-01
1973	0.0147	16663	0.9091	1.29E-01

Carbon Monoxide Property Data

Carbon monoxide property data is summarized in Table C8. Equations C13 to C16 summarize the data presented in Table C8 and were input into Fluent.

$$\rho_{CO} = 8.4846 \cdot 10^{-19}T^6 - 6.5138 \cdot 10^{-15}T^5 + 2.0358 \cdot 10^{-11}T^4 - 3.3309 \cdot 10^{-8}T^3 + 3.0534 \cdot 10^{-5}T^2 - 1.5525 \cdot 10^{-2}T + 4.0141 \quad \text{(C13)}$$

$$C_{p,co} = -5.0527 \cdot 10^{-15T^5} + 1.3241 \cdot 10^{-10}T^4 - 6.2945 \cdot 10^{-7}T^3 + 1.0008 \cdot 10^{-3}T^2 - 3.9933 \cdot 10^{-1}T + 1.0862 \cdot 10^3 \quad \text{(C14)}$$

$$k_{CO} = -2.1339 \cdot 10^{-21}T^6 + 2.0091 \cdot 10^{-17}T^5 - 7.1083 \cdot 10^{-14}T^4 + 1.1784 \cdot 10^{-10}T^3 - 1.038 \cdot 10^{-7}T^2 + 1.0343 \cdot 10^{-4}T + 9.8573 \cdot 10^{-4} \quad \text{(C15)}$$

$$\mu_{CO} = -6.8593 \cdot 10^{-24}T^6 + 5.2618 \cdot 10^{-20}T^5 - 1.5851 \cdot 10^{-16}T^4 + 2.3238 \cdot 10^{-13}T^3 - 1.7165 \cdot 10^{-10}T^2 + 1.0018 \cdot 10^{-7}T - 1.4505 \cdot 10^{-6} \quad \text{(C16)}$$

Table C8: Carbon Monoxide Property Data

T (K)	ρ (kg/m^3) [2]	C_p (J/kg-K) [2]	k (W/m-K) [2]	μ (kg/m-s) [2]
273	1.4807	1040	0.0235	1.70E-05
373	1.0829	1046	0.0300	2.14E-05
473	0.8539	1061	0.0360	2.54E-05
573	0.7049	1082	0.0418	2.92E-05
673	0.6002	1105	0.0475	3.32E-05
773	0.5226	1131	0.0531	3.72E-05
873	0.4628	1156	0.0585	4.14E-05
973	0.4153	1180	0.0639	4.56E-05
1073	0.3766	1201	0.0691	4.98E-05
1173	0.3445	1218	0.0742	5.38E-05
1273	0.3174	1232	0.0789	5.77E-05
1373	0.2943	1241	0.0834	6.15E-05
1473	0.2744	1246	0.0876	6.50E-05
1573	0.2569	1246	0.0915	6.83E-05
1673	0.2416	1243	0.0949	7.14E-05
1773	0.2280	1236	0.0981	7.42E-05
1873	0.2158	1226	0.1010	7.69E-05
1973	0.2049	1215	0.1037	7.94E-05

Carbon Dioxide Property Data

Carbon dioxide property data is summarized in Table C9. Equations C17 to C20 summarize the data presented in Table C9 and were input into Fluent.

$$\rho_{CO_2} = 1.3947 \cdot 10^{-18}T^6 - 1.0693 \cdot 10^{-14}T^5 + 3.3358 \cdot 10^{-11}T^4 - 5.4439 \cdot 10^{-8}T^3 + 4.9714 \cdot 10^{-5}T^2 - 2.5127 \cdot 10^{-2}T + 6.4306 \qquad \text{(C17)}$$

$$C_{p,co_2} = 1.4612 \cdot 10^{-17}T^6 - 1.1011 \cdot 10^{-13}T^5 + 3.2826 \cdot 10^{-10}T^4 - 4.3518 \cdot 10^{-7}T^3 + 4.0476 \cdot 10^{-6}T^2 + 7.6604 \cdot 10^{-1}T + 6.5653 \cdot 10^{2} \qquad \text{(C18)}$$

$$k_{CO_2} = 6.6276 \cdot 10^{-23}T^6 - 5.081 \cdot 10^{-19}T^5 + 1.5849 \cdot 10^{-15}T^4 - 1.3116 \cdot 10^{-11}T^3 + 7.8336 \cdot 10^{-9}T^2 + 7.8959 \cdot 10^{-5}T - 6.8978 \cdot 10^{-3} \qquad \text{(C19)}$$

$$\mu_{CO_2} = 1.6652 \cdot 10^{-23}T^6 - 1.1584 \cdot 10^{-19}T^5 + 3.1138 \cdot 10^{-16}T^4 - 3.973 \cdot 10^{-13}T^3 + 2.2957 \cdot 10^{-10}T^2 - 2.1284 \cdot 10^{-9}T + 3.1982 \cdot 10^{-6} \qquad \text{(C20)}$$

Table C9: Carbon Dioxide Property Data

T (K)	ρ (kg/m^3) [2]	C_p (J/kg-K) [2]	k (W/m-K) [2]	μ (kg/m-s) [2]
273	2.3439	859	0.0150	1.33E-05
373	1.7068	926	0.0230	1.88E-05
473	1.3437	988	0.0309	2.44E-05
573	1.1084	1044	0.0386	2.99E-05
673	0.9435	1095	0.0461	3.42E-05
773	0.8213	1140	0.0532	3.79E-05
873	0.7272	1180	0.0600	4.13E-05
973	0.6525	1215	0.0663	4.46E-05
1073	0.5917	1246	0.0721	4.78E-05
1173	0.5412	1273	0.0774	5.11E-05
1273	0.4987	1297	0.0820	5.43E-05
1373	0.4624	1317	0.0859	5.77E-05
1473	0.4311	1334	0.0891	6.10E-05
1573	0.4037	1348	0.0915	6.44E-05
1673	0.3795	1361	0.0929	6.79E-05
1773	0.3581	1371	0.0934	7.14E-05
1873	0.3390	1379	0.0929	7.49E-05
1973	0.3219	1386	0.0914	7.85E-05

Oxygen Property Data

Oxygen property data is summarized in Table C10. Equations C21 to C24 summarize the data presented in Table C10 and were input into Fluent.

$$\rho_{O_2} = 9.7111 \cdot 10^{-19}T^6 - 7.4553 \cdot 10^{-15}T^5 + 2.3299 \cdot 10^{-11}T^4 - 3.8121 \cdot 10^{-8}T^3 + 3.4943 \cdot 10^{-5}T^2 - 1.7764 \cdot 10^{-2}T + 4.5912 \tag{C21}$$

$$C_{p,O_2} = 4.7827 \cdot 10^{-18}T^6 - 3.6074 \cdot 10^{-14}T^5 + 1.2875 \cdot 10^{-10}T^4 - 2.6632 \cdot 10^{-7}T^3 + 1.693 \cdot 10^{-4}T^2 + 2.6417 \cdot 10^{-1}T + 8.2587 \cdot 10^{2} \tag{C22}$$

$$k_{O_2} = -8.797 \cdot 10^{-22}T^6 + 8.3032 \cdot 10^{-18}T^5 - 3.0747 \cdot 10^{-14}T^4 + 5.5614 \cdot 10^{-11}T^3 - 6.3685 \cdot 10^{-8}T^2 + 1.0417 \cdot 10^{-4}T - 3.3567 \cdot 10^{-4} \tag{C23}$$

$$\mu_{O_2} = -6.4691 \cdot 10^{-24}T^6 + 5.2086 \cdot 10^{-20}T^5 - 1.6812 \cdot 10^{-16}T^4 + 2.7122 \cdot 10^{-13}T^3 - 2.2569 \cdot 10^{-10}T^2 + 1.3497 \cdot 10^{-7}T - 5.1989 \cdot 10^{-6} \tag{C24}$$

Table C10: Oxygen Property Data

T (K)	ρ (kg/m^3) [2]	C_p (J/kg-K) [2]	k (W/m-K) [2]	μ (kg/m-s) [2]
273	1.6927	906	0.0243	1.95E-05
373	1.2378	936	0.0320	2.49E-05
473	0.9759	966	0.0392	2.96E-05
573	0.8055	995	0.0461	3.39E-05
673	0.6859	1021	0.0526	3.82E-05
773	0.5972	1045	0.0590	4.25E-05
873	0.5288	1067	0.0650	4.70E-05
973	0.4744	1086	0.0709	5.16E-05
1073	0.4302	1102	0.0765	5.62E-05
1173	0.3936	1115	0.0819	6.09E-05
1273	0.3627	1125	0.0871	6.55E-05
1373	0.3363	1132	0.0919	7.00E-05
1473	0.3134	1136	0.0965	7.44E-05
1573	0.2935	1137	0.1008	7.86E-05
1673	0.2760	1135	0.1048	8.27E-05
1773	0.2604	1131	0.1084	8.65E-05
1873	0.2465	1124	0.1118	9.02E-05
1973	0.2340	1115	0.1149	9.37E-05

Nitrogen Property Data

Nitrogen property data is summarized in Table C11. Equations C25 to C28 summarize the data presented in Table C11 and were input into Fluent.

$$\rho_{N_2} = 8.496 \cdot 10^{-19} T^6 - 6.5222 \cdot 10^{-15} T^5 + 2.0382 \cdot 10^{-11} T^4 - 3.3345 \cdot 10^{-8} T^3 + 3.0564 \cdot 10^{-5} T^2 - 1.5537 \cdot 10^{-2} T + 4.0162 \tag{C25}$$

$$C_{p,N_2} = 5.3737 \cdot 10^{-18} T^6 - 4.0518 \cdot 10^{-14} T^5 + 1.2544 \cdot 10^{-10} T^4 - 2.088 \cdot 10^{-7} T^3 + 1.6555 \cdot 10^{-4} T^2 + 1.1943 \cdot 10^{-1} T + 9.9697 \cdot 10^2 \tag{C26}$$

$$k_{N_2} = -1.5502 \cdot 10^{-21} T^6 + 1.297 \cdot 10^{-17} T^5 - 4.5074 \cdot 10^{-14} T^4 + 8.3502 \cdot 10^{-11} T^3 - 9.1049 \cdot 10^{-8} T^2 + 1.0625 \cdot 10^{-4} T + 3.816 \cdot 10^{-4} \tag{C27}$$

$$\mu_{N_2} = -6.974 \cdot 10^{-24} T^6 + 5.3099 \cdot 10^{-20} T^5 - 1.5811 \cdot 10^{-16} T^4 + 2.2786 \cdot 10^{-13} T^3 - 1.6466 \cdot 10^{-10} T^2 + 9.6817 \cdot 10^{-8} T - 8.5101 \cdot 10^{-7} \tag{C28}$$

Table C11: Nitrogen Property Data

T (K)	ρ (kg/m^3) [2]	C_p (J/kg-K) [2]	k (W/m-K) [2]	μ (kg/m-s) [2]
273	1.4810	1038	0.0241	1.71E-05
373	1.0831	1056	0.0309	2.15E-05
473	0.8540	1074	0.0371	2.55E-05
573	0.7050	1092	0.0430	2.94E-05
673	0.6003	1109	0.0485	3.34E-05
773	0.5227	1126	0.0538	3.76E-05
873	0.4628	1143	0.0590	4.18E-05
973	0.4153	1159	0.0641	4.61E-05
1073	0.3766	1175	0.0691	5.02E-05
1173	0.3445	1189	0.0739	5.43E-05
1273	0.3175	1203	0.0787	5.82E-05
1373	0.2944	1217	0.0835	6.19E-05
1473	0.2744	1229	0.0881	6.54E-05
1573	0.2569	1241	0.0927	6.86E-05
1673	0.2416	1252	0.0972	7.16E-05
1773	0.2280	1262	0.1016	7.44E-05
1873	0.2158	1271	0.1059	7.70E-05
1973	0.2049	1280	0.1102	7.95E-05

Lennard-Jones Parameters and Knudsen Numbers

The Knudsen number for each species in the catalyst layer were calculated using Equation C29, where k_B is the Boltzmann constant with a value of $1.38065 \cdot 10^{-23}$ J/K. The pore diameter was taken from Naseri *et al.*'s work on the X-ray tomography-based analysis of reformer catalyst coatings, where the inter-particle pore size was determined to be 10.82 microns and the intra-particle pore size was determined to be 0.37 microns [4]. A Knudsen number was deemed to be in the slip flow regime if it was between 0.01 and 0.1, with transitional flow up to a Knudsen number of 10 [5]. The Lennard-Jones parameters for the molecules (Table C12) were taken from Poling *et al.*'s book entitled *The Properties of Gases and Liquids* [6]. The Knudsen numbers (Table C13) were calculated for the maximum reformer temperature of 1,150 K and the minimum reformer temperature of 829.95 K. Only propylene was in the no-slip regime, and this was only in the inter-particle domain at temperatures under 915 K.

$$K_n = \frac{k_B T}{\sqrt{2} d_{pore} P \pi \sigma^2} \tag{C29}$$

Table C12: Lennard-Jones Parameters

Molecule	Characteristic Energy, ε/k_B (K)	Characteristic Length, σ (Angstroms)
H_2O	809.1	2.641
C_3H_6	298.9	4.678
H_2	59.7	2.827
CO	91.7	3.69
CO_2	195.2	3.941
O_2	106.7	3.467

Table C13: Knudsen Numbers for Reforming Channel Molecules in the Inter-Particle and Intra-Particle Catalyst Domains

	Temperature	Knudsen Number		Flow Regime	
	K	Inter-Particle	Intra-Particle	Inter-Particle	Intra-Particle
H_2O	**1150**	0.039	1.154	slip	slip
C_3H_6	**1150**	0.013	0.368	slip	slip
H_2	**1150**	0.034	1.007	slip	slip
CO	**1150**	0.020	0.591	slip	slip
CO_2	**1150**	0.018	0.518	slip	slip
H_2O	**829.95**	0.028	0.833	slip	slip
C_3H_6	**829.95**	0.009	0.265	no-slip	slip
H_2	**829.95**	0.025	0.727	slip	slip
CO	**829.95**	0.015	0.427	slip	slip
CO_2	**829.95**	0.013	0.374	slip	slip

Fluid Mixture Properties

The inputs and equations used by Fluent to calculate the fluid mixture properties are summarized in Table C14.

Table C14: Fluid Mixture Properties

Mixture Species Order	H_2O C_3H_6 H_2 CO CO_2 O_2 N_2 He	
Density	Incompressible Ideal Gas	$\rho = \frac{P}{\frac{R}{M_w}T}$
Specific Heat	Mixing Law	$C_p = \sum_i C_{p,i} x_i$ $x_i = mole\ fraction$
Thermal Conductivity	Ideal Gas Mixing Law	$k = \sum_i k_i x_i$
Viscosity	Ideal Gas Mixing Law	$\mu = \sum_i \mu_i x_i$
Thermal Diffusion	Kinetic Theory [7]	$D_{T,i} = -2.59 \cdot 10^{-7} T^{0.659} \left[\frac{M_{w,i}^{0.511} x_i}{\sum_{i=1}^{N} M_{w,i}^{0.511} x_i} - Y_i\right] \cdot \left[\frac{\sum_{i=1}^{N} M_{w,i}^{0.511} x_i}{\sum_{i=1}^{N} M_{w,i}^{0.489} x_i}\right]$
Mass Diffusivity	User Defined Function	
Absorption Coefficient	User Defined WSGGM	
Scattering Coefficient	0	
Refractive Index	1	

References

[1] "ANSYS Fluent Meshing User's Guide," ANSYS Inc., Canonsburg, PA, USA, 2016.

[2] Honeywell, "UniSim Design Simulation Basis," Honeywell, London, Canada, 2005.

[3] National Institute of Standards and Technology, "Water," 1998. [Online]. Available: http://webbook.nist.gov/cgi/cbook.cgi?ID=C7732185. [Accessed Jan 2015].

[4] A. T. Naseri, B. A. Peppley, J. G. Pharoah, P. Mandal, S. Litster and N. Abatzoglou, "X-Ray Tomography-Based Analysis of Transport and Reaction in the Catalyst Coating of a Reformer," *Chemical Engineering Science,* vol. 138, pp. 499-509, 2015.

[5] W. He, W. Lv and J. Dickerson, "Gas Diffusion Mechanisms and Models," in *Gas Transport in Solid Oxide Fuel Cells*, Springer Publishing, 2014, pp. 9-17.

[6] B. E. Poling, J. M. Prausnitz and J. P. O'Connell, "Appendix B: Lennard-Jones Potentials as Determined from Viscosity Data," in *The Properties of Gases and Liquids*, The McGraw-Hill Companies Inc., 2001, pp. 779-780.

[7] K. K. Kuo, Principles of Combustion, New York, USA: John Wiley and Sons, 1986.

Appendix D: Base Case Model User-Defined Functions

Diffusion User-Defined Function

```
/**************************************************************************************
********
Custom diffusion coefficients
***************************************************************************************
***********/

#include "udf.h"
#include "mem.h"
#include <stdio.h>
#include <stdlib.h>

DEFINE_DIFFUSIVITY(eff_diff_prop_nonbinary_better,c,t,i)
{
Material *m;
real divide;
#define pi 3.1415926535897 /* constant pi */
#define D_pore 0.00000037 /* intra-particle average pore size in meters from Naseri et al. */
#define G_DI 0.22 /* intra-particle diffusion correction factor from Naseri et al. */
#define R 8314 /* gas constant in J/(kmol-K) or (kg-m^2)/(kmol-K-s^2) */

real sigma[7] = {2.641,4.678,2.827,3.69,3.941,3.467,3.798}; /* characteristic length in angstroms */
real epsilon[7] = {809.1,298.9,59.7,91.7,195.2,106.7,71.4}; /* Energy parameter in Kelvin */
real T = C_T(c,t); /* temperature in kelvin */
real P = (120000 + C_P(c,t))/(100*1000); /* pressure in bars */
real diff;
real MW[8] = {18.01534,42.08127,2.01594,28.01055,44.00995,31.9988,28.0134,4.0026}; /* molecule
molecular weights in kg/kmol */
real sigma_bin[7][7];
real epsilon_bin[7][7];
real omega[7][7];
real MW_bin[7][7];
real d_bin[7][7];
real modT[7][7];
real d_ipor;
real d_k1;
real molmassfract[8];
real sum,porosity;
real y[8];
int z;
real d_i;

porosity = C_POR(c,t);
```

```
/* Mole Fraction Calculation */
sum = 0;
for (int a = 0; a < 7; a++)
{
molmassfract[a] = (C_YI(c,t,a))/MW[a]; /* kmol of species "a" per kg of mixture */
sum+=molmassfract[a]; /* kmol of mixture per kg of mixture */
}
for (int a = 0; a < 7; a++)
{
y[a] = molmassfract[a]/sum; /* mole fraction of species "a" */
}

for (int a = 0; a < 7; a++)
{
for (int b = 0; b < 7; b++)
{
sigma_bin[a][b] = (sigma[a] + sigma[b])/2; /* interaction value in angstroms */
epsilon_bin[a][b] = pow((epsilon[a]*epsilon[b]),0.5); /* energy parameter geometric average in kelvin */
modT[a][b] = T/epsilon_bin[a][b]; /* modified unitless temperature */
omega[a][b] =
(1.06036/(pow((modT[a][b]),0.1561)))+(0.193/(exp(0.47635*modT[a][b])))+(1.03587/(exp(1.52996*mod
T[a][b])))+(1.76474/(exp(3.89411*modT[a][b]))); /* unitless diffusion collision integral */
MW_bin[a][b] = 2/((1/MW[a])+(1/MW[b])); /* averaged molecular weight in kg/kmol */
d_bin[a][b] =
(0.00266*(pow(T,1.5))/(P*(pow(MW_bin[a][b],0.5))*(pow(sigma_bin[a][b],2))*omega[a][b]))/(100*100)
; /* binary diffusion coefficient in m^2/s */
}
}

if (i == 0)
{
/* H2O diffusion coefficient */
z = 0.0;
if (y[z] == 1)
{
d_i = d_bin[z][z];
}
else
{
d_i = (1-
y[z])/((y[1]/d_bin[z][1])+(y[2]/d_bin[z][2])+(y[3]/d_bin[z][3])+(y[4]/d_bin[z][4])+(y[5]/d_bin[z][5])+(y[6]/
d_bin[z][6])+(y[7]/5));
}
if ((THREAD_ID(t) == 2) || (THREAD_ID(t) == 9))
{
d_k1 = (D_pore/3)*sqrt(8*R*T/(pi*MW[z])); /* knudsen diffusivity in m^2/s */
d_ipor = (1/porosity)*G_DI/((1/d_i)+(1/d_k1)); /* effective diffusion coefficient for species a in m^2/s */
```

```
return d_ipor;
}
else
{
return d_i;
}
}

else if (i==1)
{
/* C3H6 diffusion coefficient */
z = 1.0;
if (y[z] == 1)
{
d_i = d_bin[z][z];
}
else
{
d_i = (1-
y[z])/((y[2]/d_bin[z][2])+(y[3]/d_bin[z][3])+(y[4]/d_bin[z][4])+(y[5]/d_bin[z][5])+(y[6]/d_bin[z][6])+(y[0]/
d_bin[z][0])+(y[7]/5));
}
if ((THREAD_ID(t) == 2) || (THREAD_ID(t) == 9))
{
d_k1 = (D_pore/3)*sqrt(8*R*T/(pi*MW[z])); /* knudsen diffusivity in m^2/s */
d_ipor = (1/porosity)*G_DI/((1/d_i)+(1/d_k1)); /* effective diffusion coefficient for species a in m^2/s */
return d_ipor;
}
else
{
return d_i;
}
}

else if (i==2)
{
/* H2 diffusion coefficient */
z = 2.0;
if (y[z] == 1)
{
d_i = d_bin[z][z];
}
else
{
d_i = (1-
y[z])/((y[3]/d_bin[z][3])+(y[4]/d_bin[z][4])+(y[5]/d_bin[z][5])+(y[6]/d_bin[z][6])+(y[0]/d_bin[z][0])+(y[1]/
d_bin[z][1])+(y[7]/5));
}
```

```
if ((THREAD_ID(t) == 2) || (THREAD_ID(t) == 9))
{
d_k1 = (D_pore/3)*sqrt(8*R*T/(pi*MW[z])); /* knudsen diffusivity in m^2/s */
d_ipor = (1/porosity)*G_DI/((1/d_i)+(1/d_k1)); /* effective diffusion coefficient for species a in m^2/s */
return d_ipor;
}
else
{
return d_i;
}
}

else if (i==3)
{
/* CO diffusion coefficient */
z = 3.0;
if (y[z] == 1)
{
d_i = d_bin[z][z];
}
else
{
d_i = (1-
y[z])/((y[4]/d_bin[z][4])+(y[5]/d_bin[z][5])+(y[6]/d_bin[z][6])+(y[0]/d_bin[z][0])+(y[1]/d_bin[z][1])+(y[2]/
d_bin[z][2])+(y[7]/5));
}
if ((THREAD_ID(t) == 2) || (THREAD_ID(t) == 9))
{
d_k1 = (D_pore/3)*sqrt(8*R*T/(pi*MW[z])); /* knudsen diffusivity in m^2/s */
d_ipor = (1/porosity)*G_DI/((1/d_i)+(1/d_k1)); /* effective diffusion coefficient for species a in m^2/s */
return d_ipor;
}
else
{
return d_i;
}
}

else if (i==4)
{
/* CO2 diffusion coefficient */
z = 4.0;
if (y[z] == 1)
{
d_i = d_bin[z][z];
}
else
{
```

```
d_i = (1-
y[z])/((y[5]/d_bin[z][5])+(y[6]/d_bin[z][6])+(y[0]/d_bin[z][0])+(y[1]/d_bin[z][1])+(y[2]/d_bin[z][2])+(y[3]/
d_bin[z][3])+(y[7]/5));
}
if ((THREAD_ID(t) == 2) || (THREAD_ID(t) == 9))
{
d_k1 = (D_pore/3)*sqrt(8*R*T/(pi*MW[z])); /* knudsen diffusivity in m^2/s */
d_ipor = (1/porosity)*G_DI/((1/d_i)+(1/d_k1)); /* effective diffusion coefficient for species a in m^2/s */
return d_ipor;
}
else
{
return d_i;
}
}

else if (i==5)
{
/* O2 diffusion coefficient */
z = 5.0;
if (y[z] == 1)
{
d_i = d_bin[z][z];
}
else
{
d_i = (1-
y[z])/((y[6]/d_bin[z][6])+(y[0]/d_bin[z][0])+(y[1]/d_bin[z][1])+(y[2]/d_bin[z][2])+(y[3]/d_bin[z][3])+(y[4]/
d_bin[z][4])+(y[7]/5));
}
if ((THREAD_ID(t) == 2) || (THREAD_ID(t) == 9))
{
d_k1 = (D_pore/3)*sqrt(8*R*T/(pi*MW[z])); /* knudsen diffusivity in m^2/s */
d_ipor = (1/porosity)*G_DI/((1/d_i)+(1/d_k1)); /* effective diffusion coefficient for species a in m^2/s */
return d_ipor;
}
else
{
return d_i;
}
}

else if (i==6)
{
/* N2 diffusion coefficient */
z = 6.0;
if (y[z] == 1)
{
```

```
d_i = d_bin[z][z];
}
else
{
d_i = (1-
y[z])/((y[0]/d_bin[z][0])+(y[1]/d_bin[z][1])+(y[2]/d_bin[z][2])+(y[3]/d_bin[z][3])+(y[4]/d_bin[z][4])+(y[5]/
d_bin[z][5])+(y[7]/5));
}
if ((THREAD_ID(t) == 2) || (THREAD_ID(t) == 9))
{
d_k1 = (D_pore/3)*sqrt(8*R*T/(pi*MW[z])); /* knudsen diffusivity in m^2/s */
d_ipor = (1/porosity)*G_DI/((1/d_i)+(1/d_k1)); /* effective diffusion coefficient for species a in m^2/s */
return d_ipor;
}
else
{
return d_i;
}
}

else if (i==7)
{
/* He diffusion coefficient */
d_i = 5.0;

return d_i;
}

}
```

Species Reaction Rate Source Term User-Defined Function

```
/***********************************************************************************
Custom Net Reaction Rates, equation 1 is propylene steam reforming to CO2 and equation 2 is WGS.
***********************************************************************************/

#include "udf.h"

DEFINE_NET_REACTION_RATE(UDF_prop_net,c,t,particle,pressure,temp,xi,rr,jac)
{
/***********************************************************************************
Custom Net Reaction Rates: equation 1 is propylene reforming to CO2 and equation 2 is WGS.
***********************************************************************************/

#if !RP_HOST
real R,T,P,SAV,P_h2o,P_c3h6,P_co,P_co2,P_h2;

R = 8.314; /* J/(mol-K) */
```

```
T = C_T(c,t); /* K */
P = (120000 + C_P(c,t))/(1000); /* kPa */
P_h2o = P*xi[0]; /* partial pressures in kPa */
P_c3h6 = P*xi[1];
P_h2 = P*xi[2];
P_co = P*xi[3];
P_co2 = P*xi[4];

/* Rate Constants */
real k2,K2,K_h2o,K_co,K_h2,DEN;

k2 = 4.39*(pow(10,4))*(exp(-8074.3/T)); /* kmol/(kPa*kg*h) */
K2 = exp(4400/(T-4.063)); /* unitless */
K_h2o = 1.77*(pow(10,3))*(exp(-10666.35/T)); /* 1/kPa */
K_h2 = 6.12*(pow(10,-11))*(exp(9971.13/T)); /* 1/kPa */
K_co = 8.23*(pow(10,-7))*(exp(8497.71/T)); /* 1/kPa */
DEN = 1+0+(K_co*P_co)+(K_h2*P_h2)+(K_h2o*P_h2o/P_h2); /* unitless */

/* Catalyst Properties */
real rho_alumina,porosity,eq_factor;

rho_alumina = 3900; /* kg/m^3 */
porosity = C_POR(c,t);

/* Catalyst Equivalency Factor to Account for less Catalyst in Circular Geometry than in Square
Geometry. There is around 13% less catalyst so the catalyst that is present needs to be around 13%
more effective */

eq_factor = 1.1376;

/* Rate Constant Calculations */
real rate1,rate2;

/* The rate expressions were converted from mol/g-s by multiplying the rate expressions by the density
of alumina and the space occupied by alumina. The rate expressions were then divided by porosity since
Fluent’s governing equations multiply the reaction rates by porosity. */

rate1 = eq_factor*(rho_alumina*(1-porosity)/porosity)*(2.81*(pow(10,-
2)))*(P_c3h6/(1+(0.09*P_c3h6)))*(exp(-8000/T)); /* kmol of propylene/(m^3-s) */
rate2 = eq_factor*(rho_alumina*(1-porosity)/(3600*porosity))*(k2/P_h2)*((P_co*P_h2o)-
(P_h2*P_co2/K2))/(pow(DEN,2)); /* kmol of carbon monoxide/(m^3-s) */

/* Return */
rr[0] = (-(6*rate1)-rate2); /* kgmol of steam reacted/m^3-s */
rr[1] = (-rate1); /* reaction rate for propylene */
rr[2] = ((9*rate1)+rate2); /* reaction rate for hydrogen */
rr[3] = -rate2; /* reaction rate for carbon monoxide */
rr[4] = (3*rate1)+rate2; /* reaction rate for carbon dioxide */
```

```
rr[5] = 0; /* reaction rate for oxygen */
rr[6] = 0; /* reaction rate for nitrogen */
rr[7] = 0; /* reaction rate for inert helium */

#endif
}
```

Hottel and Sarofim Absorption Coefficient User-Defined Function

```
/***************************************************
Custom Absorption Coefficients
***************************************************/

#include "udf.h"

DEFINE_GRAY_BAND_ABS_COEFF(user_gray_band_abs,c,t,ci)

{
        real abs_coeff = 0;
        real T = C_T(c,t); /* Temperature in Kelvins */
        real P = 120000+C_P(c,t); /* Presssure in Pascals */

        real P_h2o,P_tetra,P_h2,P_co,P_co2,P_n2,tee,Ts;

        P_h2o = ci[0];
        P_tetra = ci[1];
        P_h2 = ci[2];
        P_co = ci[3];
        P_co2 = ci[4];
        P_o2 = ci[5];
        P_n2 = ci[6];

        /* General Values */
/* T0 was set to 1000 K, PaLo was set to 1000 Pa*m, and P0 was set to 100000 Pa */

        tee = T/1000;
        Ts = T; /* assuming the surface temperature is the same as the gas temperature, therefore
absorption is equivalent to emissivity */

        /* Values for Carbon Dioxide (C_NM) */
        real CP_E,CPaL_fract,CPaLm,Ca;
        /*
        C_00 = -3.9893;
        C_01 = 1.2710;
        C_02 = -0.23678;
        C_10 = 2.7669;
        C_11 = -1.1090;
        C_12 = 0.19731;
```

```
C_20 = -2.1081;
C_21 = 1.0195;
C_22 = -0.19544;
C_30 = 0.39163;
C_31 = -0.21897;
C_32 = 0.044644;
*/

CP_E = (P+(0.28*P_co2))/(P0);

if (tee>0.7)
{
		CPaL_fract = 0.225*(tee^2);
}
else
{
		CPaL_fract = 0.054/(tee^2);
}
CPaLm = CPaL_fract*1000; /* Pa*m */
Ca = 1+(0.1/(tee^1.45));
/*
Cb = 0.23;
Cc = 1.47;
*/

/* Values for Steam (S_NM) */
real SP_E,SPaL_fract,SPaLm,Sa,Sb;
/*
S_00 = -2.2118;
S_01 = 0.85667;
S_02 = -0.10838;
S_10 = -1.1987;
S_11 = 0.93048;
S_12 = -0.17156;
S_20 = 0.035596;
S_21 = -0.14391;
S_22 = 0.045915;
*/
SP_E = (P+((2.56*P_h2o)/(tee^0.5)))/(100000);

SPaL_fract = 13.2*(tee^2);

SPaLm = SPaL_fract*1000; /* Pa*m */

if (tee>0.75)
{
Sa = 1.888-(2.053*log10(tee));
}
```

```
        else
        {
        Sa = 2.144;
        }

        Sb = 1.10/(tee^1.4);
        /* Sc = 0.5; */

        /* From Simulation */

        real L,tau,delta_epsi,C_epsi_fract,S_epsi_fract,C_epsi0,S_epsi0;

        L = 0.001; /* Width of Outer Tube in metres */

        /* Calculations */

        tau = P_h2o/(P_h2o + P_co2);
        delta_epsi = ((tau/(10.7+(101*tau)))-
(0.0089*(tau^10.4)))*((log10(((P_h2o+P_co2)*L)/1000))^2.76);

        /* C_epsi_fract = 1-((((Ca-1)*(1-CP_E))/(Ca+Cb-1+CP_E))*(exp(-
Cc*((log10(CPaLm/(P_co2*L)))^2)))); */
        C_epsi_fract = 1-((((Ca-1)*(1-CP_E))/(Ca+0.23-1+CP_E))*(exp(-
1.47*((log10(CPaLm/(P_co2*L)))^2))));
        /* S_epsi_fract = 1-((((Sa-1)*(1-SP_E))/(Sa+Sb-1+SP_E))*(exp(-
Sc*((log10(SPaLm/(P_h2o*L)))^2)))); */
        S_epsi_fract = 1-((((Sa-1)*(1-SP_E))/(Sa+Sb-1+SP_E))*(exp(-0.5*((log10(SPaLm/(P_h2o*L)))^2))));

        /* C_epsi0 =
exp((C_00*(t^0)*((log10(P_co2*L/PaLo))^0))+(C_10*(t^1)*((log10(P_co2*L/PaLo))^0))+(C_20*(t^2)*((lo
g10(P_co2*L/PaLo))^0))+(C_30*(t^3)*((log10(P_co2*L/PaLo))^0))+(C_01*(t^0)*((log10(P_co2*L/PaLo))^
1))+(C_11*(t^1)*((log10(P_co2*L/PaLo))^1))+(C_21*(t^2)*((log10(P_co2*L/PaLo))^1))+(C_31*(t^3)*((log
10(P_co2*L/PaLo))^1))+(C_02*(t^0)*((log10(P_co2*L/PaLo))^2))+(C_12*(t^1)*((log10(P_co2*L/PaLo))^2
))+(C_22*(t^2)*((log10(P_co2*L/PaLo))^2))+(C_32*(t^3)*((log10(P_co2*L/PaLo))^2))); */
        C_epsi0 = exp((-
3.9893*(t^0)*((log10(P_co2*L/1000))^0))+(1.271*(t^1)*((log10(P_co2*L/1000))^0))+(-
2.1081*(t^2)*((log10(P_co2*L/1000))^0))+(0.39163*(t^3)*((log10(P_co2*L/1000))^0))+(1.271*(t^0)*((lo
g10(P_co2*L/1000))^1))+(-
1.109*(t^1)*((log10(P_co2*L/1000))^1))+(1.0195*(t^2)*((log10(P_co2*L/1000))^1))+(-
0.21897*(t^3)*((log10(P_co2*L/1000))^1))+(-
0.23678*(t^0)*((log10(P_co2*L/1000))^2))+(0.19731*(t^1)*((log10(P_co2*L/1000))^2))+UDF0.19544*(t
^2)*((log10(P_co2*L/1000))^2))+(0.044644*(t^3)*((log10(P_co2*L/1000))^2)));
        /* S_epsi0 =
exp((S_00*(t^0)*((log10(P_h2o*L/1000))^0))+(S_10*(t^1)*((log10(P_h2o*L/1000))^0))+(S_20*(t^2)*((lo
g10(P_h2o*L/1000))^0))+(S_01*(t^0)*((log10(P_h2o*L/1000))^1))+(S_11*(t^1)*((log10(P_h2o*L/1000))
^1))+(S_21*(t^2)*((log10(P_h2o*L/1000))^1))+(S_02*(t^0)*((log10(P_h2o*L/1000))^2))+(S_12*(t^1)*((l
og10(P_h2o*L/1000))^2))+(S_22*(t^2)*((log10(P_h2o*L/1000))^2))); */
```

```
	S_epsi0 = exp((-2.2118*(t^0)*((log10(P_h2o*L/1000))^0))+(-
1.1987*(t^1)*((log10(P_h2o*L/1000))^0))+(0.035596*(t^2)*((log10(P_h2o*L/1000))^0))+(0.85667*(t^0)
*((log10(P_h2o*L/1000))^1))+(0.93048*(t^1)*((log10(P_h2o*L/1000))^1))+(-
0.14391*(t^2)*((log10(P_h2o*L/1000))^1))+(-0.10838*(t^0)*((log10(P_h2o*L/1000))^2))+(-
0.17156*(t^1)*((log10(P_h2o*L/1000))^2))+(0.045915*(t^2)*((log10(P_h2o*L/1000))^2)));

	C_epsi = C_epsi0*C_epsi_fract;
	S_epsi = S_epsi0*S_epsi_fract;

	C_alph = C_epsi*((T/Ts)^0.5);
	S_alph = S_epsi*((T/Ts)^0.5);

	abs_coeff = C_alph+S_alph-delta_epsi;

return abs_coeff;

}
```

Catalyst Layer Absorption Coefficient User-Defined Function

```
/*******************************************************************************
********
Custom absorption coefficients
*******************************************************************************
***********/

#include "udf.h"

DEFINE_WSGGM_ABS_COEFF(absorption_coefficients,c,t,xi,p_t,s,soot_conc,Tcell,nb,ab_wsggm,ab_soot
)
{
#if !RP_HOST

if ((THREAD_ID(t) == 2) || (THREAD_ID(t) == 9))
{
*ab_wsggm = 0.0;
}

#endif
```

Appendix E: ANSYS Fluent Simulation Results

Table E1 summarizes the ANSYS Fluent base case results.

Table E1: ANSYS Fluent Base Case Simulation Results

			Axial Reformer Position (mm)							**UniSim® Results**
			0	**1**	**2**	**5**	**10**	**20**	**30**	
Reforming Channel	**ΔP**	**Pa**	0	0.73	1.18	2.56	4.91	9.62	14.32	0
	Conversion	**%**	0	53.50	71.79	94.85	99.79	100.00	100.00	100
		%/μg$_{cat}$	0	0.54	0.36	0.19	0.10	0.05	0.03	-
	Outlet Mole %	**H_2O**	91.17	45.24	40.95	35.28	34.07	34.01	34.01	39.73
		C_3H_6	7.44	2.55	1.55	0.28	0.01	0.00	0.00	0.00
		H_2	1.39	38.22	43.18	48.67	49.68	49.72	49.72	43.98
		CO	0	0.03	0.05	0.08	0.08	0.09	0.08	5.69
		CO_2	0	9.67	12.44	15.56	16.15	16.18	16.18	10.62
	T	**K**	830	1,138	1,137	1,135	1,135	1,135	1,135	966
Flue Gas Channel	**ΔP**	**Pa**	0	14.9	32.2	82.9	167.9	337.2	506.3	0
	T	**K**	1,150	1,138	1,137	1,135	1,135	1,135	1,135	-

Figure E5 illustrates how the base case catalyst layer diffusion flux of hydrogen is initially evenly divided between mass diffusion and thermal diffusion contributions before becoming dominated by mass diffusion contributions approximately 1 mm into the reforming channel.

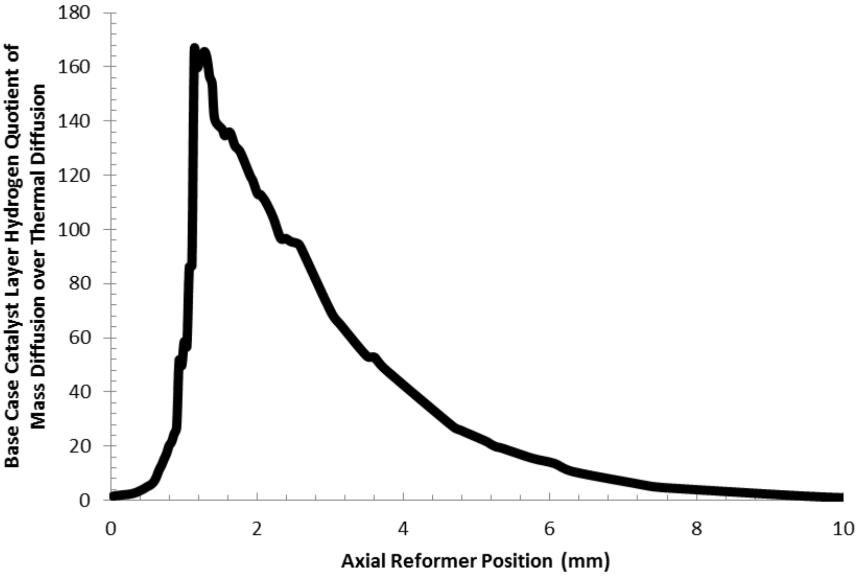

Figure E5: Comparison of base case catalyst layer hydrogen mass diffusion and thermal diffusion.

A complete stream table of the coupled ANSYS Fluent base case and 200 kW RFC UniSim® model is enclosed in Table E2 and Table E3.

Table E2: Fluent Base Case UniSim® Coupling and Optimized RFC 200 kW Stream Table 1

System Feed			
		Fluent Base Case	**UniSim®**
Mass Flow Rate (kg/h)	H_2O	259.21	259.21
	Diesel ($C_{16}H_{34}$)	49.83	49.83
	Air	1,361.28	1,344.05
Inlet Temperature (°C)		25	25
Pressure (kPa)		101.325	101.325
System Operating Pressure (kPa)		120	120
Feed Temperature after Heating (°C)	H_2O	800	800
	$C_{16}H_{34}$	300 (liquid)	300 (liquid)
	Air	818	900
Parasitic Losses (kW)		7.49	7.39
Reformer			
Outlet Temperature (°C)		862	693
Inlet Molar S/C Ratio		4.67	4.67
Outlet Mass %	H_2O	42.93	50.06
	Hydrocarbon Feed	0.00	0.00
	H_2	7.02	6.20
	CO	0.17	10.94
	CO_2	49.88	32.70
	CH_4	0.00	0.09
Outlet Mole %	H_2O	34.01	39.73
	Hydrocarbon Feed	0.00	0.00
	H_2	49.72	43.98
	CO	0.08	5.59
	CO_2	16.18	10.62
	CH_4	0.00	0.08

Table E3: Fluent Base Case UniSim® Coupling and Optimized RFC 200 kW Stream Table 2

Fuel Cell Stack			
		Fluent Base Case	**UniSim®**
Average Temperature (°C)		996	996
Fuel Utilization		0.8	0.8
Oxygen Utilization		0.4	0.4
Voltage per Cell (V/cell)		0.5235	0.5179
Current (A)		70.118	69.442
Cell Count		5,948	5,948
Total Power Generated (kW)		218.33	213.91
Net Power Output (kW)		210.84	206.52
Electrical Efficiency (%)		35.15	34.43
Outlet Mass %	H_2O	17.39	17.57
	H_2	0.32	0.24
	CO	1.76	1.95
	CO_2	6.43	6.32
	CH_4	0.00	0.00
	N_2	61.01	61.48
	O_2	11.98	11.33
	Ar	1.11	1.12
Tail Gas Burner			
Outlet Temperature (°C)		1,531	1,481
Available Excess Heat (kJ/h)	High Quality Heat (T > 100°C)	184.80	53.04
	Low Quality Heat (T > 25°C)	340.00	200.9
Combined Heat and Power Efficiencies (%)	High Quality Heat	86.06	49.04
	Low Quality Heat	128.81	89.77
Outlet Mass %	H_2O	20.27	19.67
	H_2	0.00	0.00
	CO	0.00	0.00
	CO_2	9.19	9.38
	N_2	60.89	61.38
	O_2	8.28	8.23
	Ar	1.11	1.12
	NO	0.25	0.21
	NO_2	0.00	0.00

Appendix F: User-Defined Functions for Varied Porosity Models

Intra-Particle Porosity User-Defined Function

```
/*************************************************************************
Varying porosity along length of reformer
*************************************************************************/

#include "udf.h"

DEFINE_PROFILE(porosity1,t,i)
{
#if !RP_HOST

real x[ND_ND];
real z;
cell_t c;
begin_c_loop(c,t)
{
C_CENTROID(x,c,t);
z = x[0];
F_PROFILE(c,t,i) = 0.6 - (50*z);
}
end_c_loop(c,t)

#endif
}
```

Varying Intra-Particle Porosity Diffusion User-Defined Function

```
/************************************************************************************
********
Custom diffusion coefficients for the porous region
*************************************************************************************
***********/

#include "udf.h"
#include "mem.h"
#include <stdio.h>
#include <stdlib.h>

DEFINE_DIFFUSIVITY(eff_diff_prop_nonbinary_better_intravar,c,t,i)
{
Material *m;
real divide;
#define pi 3.1415926535897 /* constant pi */
#define D_pore 0.00000037 /* intra-particle average pore size in meters */
#define R 8314 /* gas constant in J/(kmol-K) or (kg-m^2)/(kmol-K-s^2) */

real sigma[7] = {2.641,4.678,2.827,3.69,3.941,3.467,3.798}; /* characteristic length in angstroms */
real epsilon[7] = {809.1,298.9,59.7,91.7,195.2,106.7,71.4}; /* Energy parameter in Kelvin */
real T = C_T(c,t); /* temperature in kelvin */
real P = (120000 + C_P(c,t))/(100*1000); /* pressure in bars */
real diff;
real MW[8] = {18.01534,42.08127,2.01594,28.01055,44.00995,31.9988,28.0134,4.0026}; /* molecule
molecular weights in kg/kmol */
real sigma_bin[7][7];
real epsilon_bin[7][7];
real omega[7][7];
real MW_bin[7][7];
real d_bin[7][7];
real modT[7][7];
real d_ipor;
real d_k1;
real molmassfract[8];
real sum,porosity;
real y[8];
int z;
real d_i;

porosity = C_POR(c,t);

real x[ND_ND];
real w;
real por_intra; /* intra-particle porosity */
```

```
real G_DI; /* intra-particle diffusion correction factor */
real tau = 0.42/0.22; /* Naseri et al. tortuosity */

/* Mole Fraction Calculation */
sum = 0;
for (int a = 0; a < 7; a++)
{
molmassfract[a] = (C_YI(c,t,a))/MW[a]; /* kmol of species "a" per kg of mixture */
sum+=molmassfract[a]; /* kmol of mixture per kg of mixture */
}
for (int a = 0; a < 7; a++)
{
y[a] = molmassfract[a]/sum; /* mole fraction of species "a" */
}

for (int a = 0; a < 7; a++)
{
for (int b = 0; b < 7; b++)
{
sigma_bin[a][b] = (sigma[a] + sigma[b])/2; /* interaction value in angstroms */
epsilon_bin[a][b] = pow((epsilon[a]*epsilon[b]),0.5); /* energy parameter geometric average in kelvin */
modT[a][b] = T/epsilon_bin[a][b]; /* modified unitless temperature */
omega[a][b] =
(1.06036/(pow((modT[a][b]),0.1561)))+(0.193/(exp(0.47635*modT[a][b])))+(1.03587/(exp(1.52996*mod
T[a][b])))+(1.76474/(exp(3.89411*modT[a][b]))); /* unitless diffusion collision integral */
MW_bin[a][b] = 2/((1/MW[a])+(1/MW[b])); /* averaged molecular weight in kg/kmol */
d_bin[a][b] =
(0.00266*(pow(T,1.5))/(P*(pow(MW_bin[a][b],0.5))*(pow(sigma_bin[a][b],2))*omega[a][b]))/(100*100)
; /* binary diffusion coefficient in m^2/s */
}
}

if (i == 0)
{
/* H2O diffusion coefficient */
z = 0.0;
if (y[z] == 1)
{
d_i = d_bin[z][z];
}
else
{
d_i = (1-
y[z])/((y[1]/d_bin[z][1])+(y[2]/d_bin[z][2])+(y[3]/d_bin[z][3])+(y[4]/d_bin[z][4])+(y[5]/d_bin[z][5])+(y[6]/
d_bin[z][6])+(y[7]/5));
}
if ((THREAD_ID(t) == 2) || (THREAD_ID(t) == 9))
{
```

```
C_CENTROID(x,c,t);
w = x[0];
por_intra = (0.46+(50*w))/0.86;
G_DI = por_intra/tau;
d_k1 = (D_pore/3)*sqrt(8*R*T/(pi*MW[z])); /* knudsen diffusivity in m^2/s */
d_ipor = (1/porosity)*G_DI/((1/d_i)+(1/d_k1)); /* effective diffusion coefficient for species a in m^2/s */
return d_ipor;
}
else
{
return d_i;
}
}

else if (i==1)
{
/* C3H6 diffusion coefficient */
z = 1.0;
if (y[z] == 1)
{
d_i = d_bin[z][z];
}
else
{
d_i = (1-
y[z])/((y[2]/d_bin[z][2])+(y[3]/d_bin[z][3])+(y[4]/d_bin[z][4])+(y[5]/d_bin[z][5])+(y[6]/d_bin[z][6])+(y[0]/
d_bin[z][0])+(y[7]/5));
}
if ((THREAD_ID(t) == 2) || (THREAD_ID(t) == 9))
{
C_CENTROID(x,c,t);
w = x[0];
por_intra = (0.46+(50*w))/0.86;
G_DI = por_intra/tau;
d_k1 = (D_pore/3)*sqrt(8*R*T/(pi*MW[z])); /* knudsen diffusivity in m^2/s */
d_ipor = (1/porosity)*G_DI/((1/d_i)+(1/d_k1)); /* effective diffusion coefficient for species a in m^2/s */
return d_ipor;
}
else
{
return d_i;
}
}

else if (i==2)
{
/* H2 diffusion coefficient */
z = 2.0;
```

```
if (y[z] == 1)
{
d_i = d_bin[z][z];
}
else
{
d_i = (1-
y[z])/((y[3]/d_bin[z][3])+(y[4]/d_bin[z][4])+(y[5]/d_bin[z][5])+(y[6]/d_bin[z][6])+(y[0]/d_bin[z][0])+(y[1]/
d_bin[z][1])+(y[7]/5));
}
if ((THREAD_ID(t) == 2) || (THREAD_ID(t) == 9))
{
C_CENTROID(x,c,t);
w = x[0];
por_intra = (0.46+(50*w))/0.86;
G_DI = por_intra/tau;
d_k1 = (D_pore/3)*sqrt(8*R*T/(pi*MW[z])); /* knudsen diffusivity in m^2/s */
d_ipor = (1/porosity)*G_DI/((1/d_i)+(1/d_k1)); /* effective diffusion coefficient for species a in m^2/s */
return d_ipor;
}
else
{
return d_i;
}
}

else if (i==3)
{
/* CO diffusion coefficient */
z = 3.0;
if (y[z] == 1)
{
d_i = d_bin[z][z];
}
else
{
d_i = (1-
y[z])/((y[4]/d_bin[z][4])+(y[5]/d_bin[z][5])+(y[6]/d_bin[z][6])+(y[0]/d_bin[z][0])+(y[1]/d_bin[z][1])+(y[2]/
d_bin[z][2])+(y[7]/5));
}
if ((THREAD_ID(t) == 2) || (THREAD_ID(t) == 9))
{
C_CENTROID(x,c,t);
w = x[0];
por_intra = (0.46+(50*w))/0.86;
G_DI = por_intra/tau;
d_k1 = (D_pore/3)*sqrt(8*R*T/(pi*MW[z])); /* knudsen diffusivity in m^2/s */
d_ipor = (1/porosity)*G_DI/((1/d_i)+(1/d_k1)); /* effective diffusion coefficient for species a in m^2/s */
```

```
return d_ipor;
}
else
{
return d_i;
}
}

else if (i==4)
{
/* CO2 diffusion coefficient */
z = 4.0;
if (y[z] == 1)
{
d_i = d_bin[z][z];
}
else
{
d_i = (1-
y[z])/((y[5]/d_bin[z][5])+(y[6]/d_bin[z][6])+(y[0]/d_bin[z][0])+(y[1]/d_bin[z][1])+(y[2]/d_bin[z][2])+(y[3]/
d_bin[z][3])+(y[7]/5));
}
if ((THREAD_ID(t) == 2) || (THREAD_ID(t) == 9))
{
C_CENTROID(x,c,t);
w = x[0];
por_intra = (0.46+(50*w))/0.86;
G_DI = por_intra/tau;
d_k1 = (D_pore/3)*sqrt(8*R*T/(pi*MW[z])); /* knudsen diffusivity in m^2/s */
d_ipor = (1/porosity)*G_DI/((1/d_i)+(1/d_k1)); /* effective diffusion coefficient for species a in m^2/s */
return d_ipor;
}
else
{
return d_i;
}
}

else if (i==5)
{
/* O2 diffusion coefficient */
z = 5.0;
if (y[z] == 1)
{
d_i = d_bin[z][z];
}
else
{
```

```
d_i = (1-
y[z])/((y[6]/d_bin[z][6])+(y[0]/d_bin[z][0])+(y[1]/d_bin[z][1])+(y[2]/d_bin[z][2])+(y[3]/d_bin[z][3])+(y[4]/
d_bin[z][4])+(y[7]/5));
}
if ((THREAD_ID(t) == 2) || (THREAD_ID(t) == 9))
{
C_CENTROID(x,c,t);
w = x[0];
por_intra = (0.46+(50*w))/0.86;
G_DI = por_intra/tau;
d_k1 = (D_pore/3)*sqrt(8*R*T/(pi*MW[z])); /* knudsen diffusivity in m^2/s */
d_ipor = (1/porosity)*G_DI/((1/d_i)+(1/d_k1)); /* effective diffusion coefficient for species a in m^2/s */
return d_ipor;
}
else
{
return d_i;
}
}

else if (i==6)
{
/* N2 diffusion coefficient */
z = 6.0;
if (y[z] == 1)
{
d_i = d_bin[z][z];
}
else
{
d_i = (1-
y[z])/((y[0]/d_bin[z][0])+(y[1]/d_bin[z][1])+(y[2]/d_bin[z][2])+(y[3]/d_bin[z][3])+(y[4]/d_bin[z][4])+(y[5]/
d_bin[z][5])+(y[7]/5));
}
if ((THREAD_ID(t) == 2) || (THREAD_ID(t) == 9))
{
C_CENTROID(x,c,t);
w = x[0];
por_intra = (0.46+(50*w))/0.86;
G_DI = por_intra/tau;
d_k1 = (D_pore/3)*sqrt(8*R*T/(pi*MW[z])); /* knudsen diffusivity in m^2/s */
d_ipor = (1/porosity)*G_DI/((1/d_i)+(1/d_k1)); /* effective diffusion coefficient for species a in m^2/s */
return d_ipor;
}
else
{
return d_i;
}
```

```
}

else if (i==7)
{
/* He diffusion coefficient */
d_i = 5.0;

return d_i;
}

}
```